Marangoni driven free surface flows in liquid weld pools

Zaki Saptari SALDI

The research reported in this thesis was carried out at the Department of Multi Scale Physics, Faculty of Applied Sciences, Delft University of Technology, Prins Bernhardlaan 6, 2628 BW, Delft, The Netherlands.

Delft University of Technology

The research was carried out under the project number MC8.05240 in the framework of the research program of the Materials innovation institute (M2i).

MARANGONI DRIVEN FREE SURFACE FLOWS IN LIQUID WELD POOLS

PROEFSCHRIFT

ter verkrijging van de graad van doctor
aan de Technische Universiteit Delft,
op gezag van de Rector Magnificus Prof. ir. K.C.A.M. Luyben,
voorzitter van het College voor Promoties,
in het openbaar te verdedigen op

vrijdag, 7 december 2012, om 10:00 uur

door

Zaki Saptari SALDI

Master of Engineering
from Toyohashi University of Technology, Japan
geboren te Jakarta, Indonesië

Dit proefschrift is goedgekeurd door de promotor:

Prof. dr. ir. C.R. Kleijn

Copromotor:

Dr. S. Kenjereš, Dipl.-Ing.

Samenstelling promotiecommisie:

Rector Magnificus,	voorzitter
Prof. dr. ir. C.R. Kleijn,	Technische Universiteit Delft, promotor
Dr. S. Kenjereš, Dipl.-Ing.,	Technische Universiteit Delft, copromotor
Prof. dr. I.M. Richardson,	Technische Universiteit Delft
Prof. dr. ir. C. Vuik,	Technische Universiteit Delft
Prof. H. Dong, PhD,	University of Leicester
Prof. em. dr. J.A. Dantzig,	University of Illinois at Urbana-Champaign
Dr. R.P.J. Duursma,	Tata Steel

ISBN: 978-94-6190-980-0

Printed in The Netherlands.

To Rafa, Selly, Ibu, Bapak, Mama, and Papa

Contents

1 CHAPTER

Introduction

1.1 Background

Laser welding is one of the most widely used joining processes in the manufacture of engineering structures and products, *e.g.* in the area of automotive, aerospace, naval, electronic, and civil engineering. In order to meet increasingly demanding requirements in the modern era, there is a continuous need to develop improved welding techniques for novel alloys and engineering structures need to be robust and reliable. These traits can only be guaranteed through continuous improvement of weld quality, mainly by advancing the methodologies that allow for tailoring of the weld composition, structure, and properties (David and DebRoy (1992)).

Weld composition, structure, and properties are known to be dependent on the hydrodynamics of the weld pools, *i.e.* the liquid region of the fusion zone formed during heating, at typically millimeter length scale. Weld pool hydrodynamics, predominantly driven by Marangoni convection due to surface tension gradients, plays an important role in the energy transfer to the surrounding heat-affected zone (figure 1.1). The energy transfer affects the final weld shape, post-solidification microstructures, and residual stresses, which correlate to the weld quality, *e.g.* mechanical strength, fatigue life, resistance to corrosion, etc. Therefore, gaining insights into how weld pool hydrodynamics influences heat and mass transfer is essential in order to yield optimized and better controlled high-quality welds.

The aforementioned tailoring of weld composition and properties, as a matter of fact, was what motivated the project in which the research reported in this thesis was carried out. The project was primarily driven by the interest from the industrial partner (Tata Steel, formerly Corus Netherlands) in investigating the use of chemical elements in welding using a consumable wire. Elements added to the weld pool through the wire are *e.g.* zirconium and scandium as grain refiners, or calcium as surface active elements. These elements can help improve the weld properties. Nevertheless, their detailed transport mechanism and influence on

hydrodynamics are unknown. Numerical prediction of the weld pool hydrodynamics, as the main focus in this thesis, will provide a basis for studying element mixing in weld pools.

1.2 Physical phenomena and relevant dimensionless numbers in weld pools

Despite the small length scale of weld pools, there is a complex physics related to hydrodynamics involving intercoupled aspects (Lancaster (1984), Kumar et al. (2007), Debroy and David (1995)), including melting, flow, mass, and heat transfers, solidification, free surface deformations, and interfacial reaction. These intercoupled phenomena are illustrated in figure 1.1. The non-uniform heat influx (*e.g.* from a laser source) melts the solid workpiece into the liquid weld pool and creates a thermal gradient at the free surface. For liquid steels subjected to a conduction mode laser flux, *i.e.* in which the keyhole formation and vaporization are negligible, the thermal gradient is typically of the order of 10^2 - 10^3 K/mm. This is a few order of magnitudes lower than for high energy and high intensity laser welding (Batteh et al. (2000), Zhou and Tsai (2008), Zhou and Tsai (2009)), where keyhole and vaporization are significant. Additionally, the surface tension gradients also stem from the variation of the surface active elements at the weld pool surface (Mills et al. (1998)). The dependence of surface tension on temperature and element concentration thus results in a significant spatial variation of surface tension, manifested in Marangoni stresses at the free surface. These stresses must be balanced by shear stresses due to the liquid metal viscosity. Shear stresses from regions of low to high surface tension essentially drives the weld pool flow. This Marangoni driven flow can have a profound impact on the final weld shapes (Oreper and Szekely (1984), Heiple and Roper (1982), Heiple et al. (1983)).

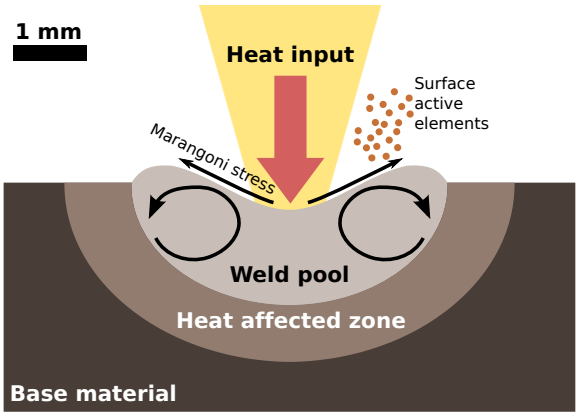

Figure 1.1. A 2-D sketch of the weld cross section, showing the weld pool and the heat affected zone.

The significance of the surface tension gradient due to thermal effects is given by

the thermal Marangoni number:

$$\mathrm{Mg} = \frac{(d\sigma/dT)\, L\Delta T}{\mu\alpha} \tag{1.1}$$

where $d\sigma/dT$ is the variation of surface tension with temperature, L a characteristic length scale, ΔT the temperature difference, μ the dynamic viscosity, and α the thermal diffusivity. The typical Marangoni numbers in laser weld pools are $\mathrm{Mg} \sim 10^2$ - 10^5.

In weld pools, temperature gradients also lead to density gradients, which give rise to buoyancy effects. However, when compared to Marangoni driven flow, buoyancy driven flow is much less important. This is characterized by a small ratio of the Rayleigh and Marangoni numbers, also known as the dynamic Bond number:

$$\mathrm{Bo} = \frac{\mathrm{Ra}}{\mathrm{Mg}} = \frac{\rho g\beta\Delta T L^3/(\mu\alpha)}{(d\sigma/dT)\, L\Delta T/(\mu\alpha)} = \frac{\rho g\beta L^2}{d\sigma/dT} \tag{1.2}$$

where ρ is the fluid density, g the gravitational acceleration constant, and β thermal expansion coefficient. This ratio is typically 10^{-4} - 10^{-3}, due to the small size of weld pools.

Hydrodynamics and transport phenomena in weld pools also depend on the material used. The properties of liquid metal, namely viscosity and thermal diffusivity, determine the Prandtl number, which represents the ratio of momentum to thermal diffusion. The Prandtl number is expressed as:

$$\mathrm{Pr} = \frac{\nu}{\alpha} \tag{1.3}$$

where ν is the kinematic viscosity. For liquid steel flow, Pr is in the order of 0.1.

The characteristic velocity U can be obtained by balancing the surface tension force and the viscous force:

$$\frac{\Delta\sigma}{L} = \frac{\mu U}{L} \tag{1.4}$$

where $\Delta\sigma$ is the surface tension difference. Hence:

$$U = \frac{\Delta\sigma}{\mu} \simeq \frac{(d\sigma/dT)\,\Delta T}{\mu} \tag{1.5}$$

Heat and mass in weld pools can be transported by means of: (1) convection, due to liquid flows; and (2) conduction or diffusion, due to gradients of temperature or element concentration, respectively. The ratio of convective to conductive or diffusive transport is given by the Peclet number. When heat transfer is considered, the heat Peclet number is:

$$\mathrm{Pe}_{\mathrm{heat}} = \frac{UL}{\alpha} \simeq \frac{L\,(d\sigma/dT)\,\Delta T}{\alpha\mu} \tag{1.6}$$

, whereas for mass transfer, the mass Peclet number is:

$$\mathrm{Pe}_{\mathrm{mass}} = \frac{UL}{\mathcal{D}} \simeq \frac{L\,(d\sigma/dT)\,\Delta T}{\mathcal{D}\mu} \tag{1.7}$$

where $\mathcal{D}$ the species diffusivity. Many studies on weld pool flows showed that both Peclet numbers are in the order of 10 - 10^2, indicating that convective transport prevails over conduction or diffusion.

The weld pool free surface can experience deformations when surface tension forces can not balance the viscous forces due to thermocapillarity of the weld pool. The degree of surface deformation can be characterized by the Capillary number:

$$\mathrm{Ca} = \frac{\mu U}{\sigma_0} \simeq \frac{(d\sigma/dT)\,\Delta T}{\sigma_0} \tag{1.8}$$

where σ_0 is the reference surface tension. The typical Capillary number in weld pools is $\mathrm{Ca} \sim 10^{-1}$, which is sufficiently large to cause a surface deformation. In return, the free surface deformation also influences the internal weld pool flow, hence the heat and mass transfers. Experimental observations on free surface oscillations in conduction mode laser spot welding have been reported by Kou et al. (2011).

Whether a weld pool flow is laminar or turbulent is still an unresolved issue. However, the surface tension Reynolds number:

$$\mathrm{Re}_{\sigma} \simeq \frac{\rho L\,(d\sigma/dT)\,\Delta T}{\mu^2} \tag{1.9}$$

, which defines the ratio of surface tension force to viscous force, can be as large as 10^5, leading to a highly unstable and a violent free surface flow. This in fact has been observed experimentally for liquid steel weld pools (Zhao et al. (2010)), where the flow is also highly transient and asymmetric (three-dimensional). For surface tension dominated flows, Aboutalebi et al. (1995) also proposed that weld pool flow becomes turbulent if Re_{σ} is much larger than 100.

1.3 General overview of studies on weld pool flows

Studies of weld pool flows have been carried out over the span of three decades, mainly through experiments but also through numerical simulations. In this section, overview of experimental techniques and numerical models is given.

1.3.1 Experimental studies

Experimental measurements on weld pool flows have been widely reported in literature. In general, the authors often faced a number of obstacles, mainly due to the small dimensions, opacity, and high temperature of the weld pool. However, viable measurements of weld pool velocities have been made, although often limited to the free surface flow. Successful observations of weld surface flow essentially owed to the presence of oxide particles, which are transported by the free surface flow. The movement of these particles can be captured using high speed camera (Henrikson (2005), Delapp et al. (2005), Zhao et al. (2009), Zhao et al. (2010)), and techniques such as Particle Tracking Velocimetry (Henrikson (2005)) and Particle Image Velocimetry (Zhao et al. (2009)) can provide a quantitative description of the velocity direction and magnitudes. Such information was helpful in identifying the surface flow patterns.

On the other hand, one of the initial efforts in measuring internal flow was done by Limmaneevichitr (2000) with the aid of a physical model in experiments on liquid sodium nitrate. This material has a transparent melt, a relatively low melting temperature, and a strong variation of surface tension with respect to temperature. Moreover, the Marangoni number is close to that of typical welding materials, such as steel and aluminum. Such characteristics made sodium nitrate suitable in reproducing steel or aluminum weld pool flows. By containing the liquid sodium nitrate in a hemispherical glass tube, the cross sectional flow of tracers in the melt (aluminum particles) could be visualized using a laser light-sheet technique. In addition, effects of a surface active elements addition in creating an inward flow were demonstrated. This finding agreed with what was suggested by Heiple and Roper (1982) and Heiple et al. (1983): a minor presence of surface active elements can substantially change the temperature dependence of surface tension, leading to a change in flow pattern.

A more recent and advanced internal flow visualization technique was started by Mizutani et al. (2003), Naito et al. (2006), and Katayama et al. (2001) through the use of X-ray transmission technique. This technique, in fact, eliminated the problem associated with the liquid metal opacity. Using this method, Naito et al. (2006) were able to observe the development of the internal flows in weld pool keyhole during hybrid TIG-Nd:YAG welding. Furthermore, porosity due to bubble formation was also identified.

1.3.2 Numerical studies

In conjunction with experiments, numerical simulations by means of Computational Fluid Dynamics (CFD) have been of importance in studying the fluid flow and heat transfer in weld pool. CFD offers a great benefit over experimental measurement that is complicated by the small dimensions, opacity, and high temperature fields. It allows for a detailed analysis of the time-dependent flow and heat transfer, both at free surface and inside the weld pool. In this section, available models are reviewed with consideration of several aspects, such as free surface deformation, turbulence, and solidification stage.

Flat and free surface simulations

In predicting weld pool flows, many numerical models in literature relied on a flat surface assumption on 2-D (Chan et al. (1984)), 2-D axisymmetric (Chan et al. (1987), Choo et al. (1992), Pitscheneder et al. (1996)) and 3-D (Chan et al. (1983), Mishra and Debroy (2005), Ribic et al. (2008)) coordinate systems, thus being unable to simulate the free surface deformations. On the other hand, simulation of weld pools with deforming free surface had contributions from, among others, the following: Paul and DebRoy (1988) showed that free surface simulations resulted in a solidified surface topography that agreed to a fair extent with experimental observation. Thompson and Szekely (1989) used a coordinate transformation approach to predict the free surface deformation and demonstrated that for a negative surface tension temperature gradient, free surface deformation increased the maximum velocity at the surface by less than 10% from that obtained using non-deformable surface. Tsai and Kou (1989) revealed that for a positive surface tension temperature gradient, free surface deformation caused a decay of downward velocities at the center of the weld pool, which is more rapid than the decay for a flat surface case. Therefore, the resulting weld pool with deforming free surface is about 14% less deep than the weld pool with flat surface. Ha and Kim (2005) presented a result showing a small increase of depth and width of laser weld pool with deformable free surface compared to that with flat surface. They attributed this increase to the enhanced convective heat transfer due to the free surface oscillations.

Laminar and turbulent flows

As addressed briefly in section 1.2, it is still not completely clear whether weld pool flow is turbulent or laminar. In terms of numerical modeling, many models in the past have used laminar assumption, while simulations taking into account turbulence models were also reported.

Many flat surface laminar models were reported to use fitting factors for the thermal conductivity and the viscosity to enhance the momentum and the energy transfers (*e.g.* Choo et al. (1992), Choo and Szekely (1994), Mundra and DebRoy (1993), Pitscheneder et al. (1996)), which in reality are likely due to the flow instabilities and/or possibly turbulence. This was done in order to obtain good agreement with the experimental results in terms of the weld pool shapes. The enhancement factors, obtained using inverse modeling, are used uniformly in the weld pool, thus ruling out the non-homogeneous transport enhancement due to local instabilities and velocity gradients. Such an approach completely masks the role of flow instabilities caused by the surface deformations and fails to explain the physics behind the hydrodynamics-driven transport enhancement. This can lead to an inaccurate prediction of the time-dependent mixing of the elements in the weld pool, which is important for the determination of the microstructure quality.

3-D simulations using turbulence models were reported to provide better weld pool shape agreement with experiment, although all of these models also em-

ployed flat surface assumption. Choo and Szekely (1994) used Reynolds-Averaged Navier-Stokes (RANS) turbulence models in their simulation and suggested that weld pool flows are likely to be turbulent or at least transitional, rather than laminar. This was proposed based on their finding that numerical simulations with turbulent models provide a better agreement of weld pool shape with experimental results. However, strangely enough, in their simulations an enhancement factor of 100 was employed, rendering the role of the turbulence model useless. Hong et al. (2002) employed k - ϵ turbulence model in the simulation of GTA welding of 304 stainless steel. Furthermore, Hong et al. (2003) used a vorticity-based turbulence model in their simulation. Both of these simulations provide a good agreement of weld pool depth, whereas the depth obtained using a laminar model was found to overpredict experimental results. This was achieved by completely eliminating the use of enhancement factors. Jaidi and Dutta (2004) numerically studied weld pool flow in Gas Metal Arc Welding (GMAW) using a k - ϵ turbulence model and flat surface assumption (with models to account for energy input from the metal droplets). They demonstrated that the thermal diffusion is enhanced and results in a deeper weld pool. Relevant to this, the maximum velocity and temperature on the surface are decreased due to the eddy diffusivities. They also showed that the maximum ratio of turbulent-to-laminar viscosity was found close to the weld pool surface and abruptly decreases towards the weld pool boundary. This is likely to correlate with a strong Marangoni convection at the surface, which corresponds with a high turbulent kinetic energy.

Turbulent flow predictions may also be carried out in greater detail by means of Direct Numerical Simulation (DNS) and Large Eddy Simulation (LES). As opposed to the use of turbulence modeling which solves the transport of the mean flow quantities, these two simulation techniques resolve a wider range of flow scales in the turbulence spectrum: in DNS, all scales are resolved, whereas in LES the large scales are resolved and the smaller scales are modeled. In the area of weld pool hydrodynamics, literature reporting simulations using any of these two methods is nearly nonexistent, most probably due to a formidable requirement of computational resources. The only literature reporting the use of LES is by Chatterjee and Chakraborty (2005), who studied a general laser surface melting process. It was shown that LES approach could predict pool depth that agrees better with experiment, compared to the laminar and k - ϵ model. Nevertheless, the simulation was performed on quite coarse mesh resolution (around 200,000 computational cells), far below the typical mesh resolution for LES.

Solidification stage

Models in literature most often did not account for the solidification stage after the heat source is switched off. This implies that any comparison of computed weld shapes with experimental results lacks from the fact that experimental results were obtained for solidified welds, whereas numerical results showed welds at the end of the heating stage. A few works incorporating the solidification stage were reported by *e.g.* Paul and DebRoy (1988) and Traidia et al. (2010). Furthermore, coupling between macroscale flow and heat simulation with solidifi-

cation at microstructure scale has also been started in recent years, as shown in *e.g.* Pavlyk and Dilthey (2004).

1.4 Objectives

The main objectives of the research reported in this thesis are:

1. To develop a numerical model implemented in a Computational Fluid Dynamics (CFD) code that allows for the prediction of the flow field and heat transfer in steel weld pools subjected to a laser heat source during conduction mode laser spot welding.
2. To answer the question: which level of sophistication (*e.g.* 2-dimensional or 3-dimensional, with a flat or deformable liquid surface, with or without inclusion of the solidification phase) is needed to accurately model the physics of weld formation?
3. To use the developed code to study the physics of the weld pool flow. In particular, we seek to answer the following questions: (a) How does the Marangoni driven flow in the weld pool influence the shape of the final fusion zone?; (b) How does the Marangoni driven flow in the weld pool depend on the amount of heat supplied to the weld, and on the concentration of surface active elements in the weld pool?; and (c) What is the role of free surface deformation and flow instabilities on the heat transfer and on the shape of the final fusion zone?

1.5 Scope of the thesis

The research reported in this thesis deals with the CFD studies of weld pool hydrodynamics and heat transfer. The material of the workpiece is stainless steel, subjected to a stationary laser (laser spot welding). The combination of the laser power and the laser beam radius is kept within the range of conduction mode, which means that keyhole formation and vaporization do not take place.

From the numerical simulations perspective, two models are used in this thesis. One model uses the flat surface assumption, whereas the other includes free surface deformations.

In a parallel project, an experimental work devoted to studying the weld pool flows was carried out by Chuangxin Zhao (Zhao (2011)). His experimental data is used to validate the simulation results in this thesis.

1.6 Outline

The organization of this thesis is as follows. Chapter 2 discusses the numerical models used in the CFD code. They encompass the conservation equations and

the numerical treatment of the model by the Finite Volume Method. A section devoted to the open source CFD code used in this thesis, *i.e.* OpenFOAM, is also given. Chapter 3 contains the numerical test cases used to validate the developed OpenFOAM solvers. Several known benchmark test cases are reported, in which the relevant physical aspects in weld pool hydrodynamics are assessed. Chapter 4 serves to validate the weld pool model with a flat surface assumption. The validation was done against a reported case in a literature. In this chapter, a critical review on the enhancement of momentum and heat transfer as has been treated by flat surface models in the literature is addressed. Chapter 5 is complementary to chapter 4, in that it covers the free surface simulations of the case in chapter 4. The role of free surface in hydrodynamics and energy transfer is discussed. Chapter 6 is focused on the numerical prediction of the observed flows in the parallel experimental project by Zhao (2011), under the influence of oxygen in the environment. Comparisons between flat and free surface models for those experiments is also discussed. Chapter 7 ends the thesis with the concluding remarks as well as some recommendations for future studies.

1.7 Acknowledgement

The PhD research reported in this thesis was carried out under the project number MC8.05240 in the framework of the research program of the Materials innovation institute (M2i). The project was also supported by the industrial partner, *i.e.* Tata Steel (formerly Corus Netherlands). The author was affiliated with the Department of Multi Scale Physics, Delft University of Technology, and closely collaborated with the group of Joining and Material Behaviour, Department of Material Science and Engineering, Delft University of Technology. The PhD researcher working in the latter, Chuangxin Zhao, carried out the experimental studies, from which the data for validation of the CFD simulations in this thesis was obtained. The support of the aforementioned parties is gratefully acknowledged.

2 CHAPTER

Numerical Methods

2.1 Introduction

This chapter presents the numerical methods employed in this thesis. Firstly, the physical problem is described and an explanation of the two models considered in this thesis, namely solid-liquid (flat surface) and solid-liquid-gas (free surface) model, is given. In this thesis, the terms solid-liquid model and flat surface model are used interchangeably, as are the terms solid-liquid-gas model and free surface model. Furthermore, the governing continuum equations pertaining to the problem of liquid metal hydrodynamics for both models are presented. Following that, the finite volume discretization of the governing equations is explained. Then the procedure of how the numerical methods sequentially work in the code is outlined. Finally the open-source CFD code OpenFOAM, into which the numerical model equations are implemented, is presented.

2.2 Physical models

The problem of liquid metal hydrodynamics in this thesis involves three phases, *i.e.* solid, liquid, and gas. In this section, we first distinguish two approaches to model the physical problem of interest, based on how many phases are taken into account, as shown in figure 2.1.

The first approach is the solid-liquid model, in which we ignore the gas phase in our simulation. Using such an approach, the liquid-gas interface is assumed to be non-deformable and is aligned with the computational domain boundary, at which the pertaining boundary conditions are employed. A bulk volume of studies in the literature show that this model has been widely employed in the weld pool flow modeling community (Pitscheneder et al. (1996), Winkler et al. (2000), Wang et al. (2001), Zhang et al. (2003), He et al. (2003), Jaidi and Dutta (2004), Mishra and Debroy (2005), Ribic et al. (2008), Do-Quang et al. (2008), Wei et al. (2009)). When using this model, it is assumed that the Capillary number (Eq. 1.8) is so small that surface tension can keep the surface from deforming.

Using the second approach, *i.e.* the solid-liquid-gas model, the gas phase is included in the simulation. With this approach, the liquid-gas interface is free to deform, and instead of being aligned at the computational domain boundaries, it is implicitly captured as a numerical solution to the conservation equation in the internal part of the domain.

Both approaches deal with the melting front (solid-liquid interface) by coupling the energy equation (to solve the temperature field) with the liquid fraction field (which specifies whether and to which extend a computational cell is in the solid or the liquid phase). Similar to the liquid-gas interface in the solid-liquid-gas model, the solid-liquid interface in both models is also implicitly captured by the solution to the conservation equation, in this case the energy equation.

We will be using methods for capturing the free surface (liquid-gas interface) and the melting front (solid-liquid interface), that allow for solving the conservation equations on a fixed mesh system, meaning that these interfaces do not have to be tracked explicitly by deforming the mesh.

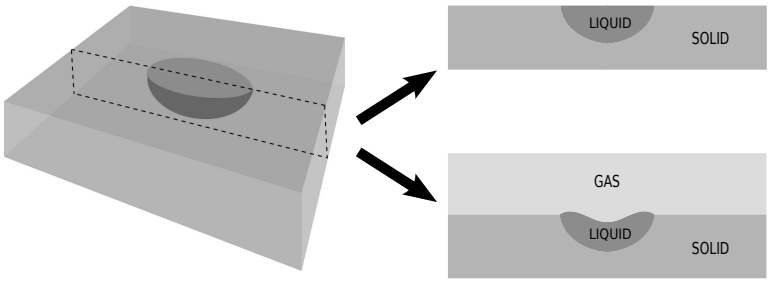

Figure 2.1. Three-dimensional problem sketch of weld pool (left) and the modeling approaches: solid-liquid model (right, top) and solid-liquid-gas model (right, bottom). For easiness, the two models are illustrated in the 2-D cross section.

2.3 Solid-liquid model

2.3.1 Governing equations

The employed solid-liquid model is based on the following continuum equations of the conservation of mass, momentum, and energy:

$$\frac{\partial \rho}{\partial t} + \nabla \cdot (\rho \mathbf{U}) = 0 \tag{2.1}$$

$$\frac{\partial \rho \mathbf{U}}{\partial t} + \nabla \cdot (\rho \mathbf{U}\mathbf{U}) = -\nabla p + \nabla \cdot (\mu \nabla \mathbf{U}) + \mathbf{S}_{\mathbf{U}} \tag{2.2}$$

$$\frac{\partial \left(\rho C_p T\right)}{\partial t} + \nabla \cdot (\rho \mathbf{U} C_p T) = \nabla \cdot (k \nabla T) + S_T \tag{2.3}$$

Here, ρ is the fluid density, $\mathbf{U}$ the velocity vector, t time, p pressure, μ dynamic viscosity, C_p specific heat constant, T temperature, and k thermal conductivity. Additionally, $\mathbf{S_U}$ and S_T are momentum and energy source terms, respectively. These source terms will be discussed further in subsections 2.3.2 and 2.3.3.

2.3.2 Momentum source & sink

The contribution to the term $\mathbf{S_U}$ is two-fold. First, the temperature difference creates a density difference, which results in the buoyancy force in the direction of the gravity vector. Second, the velocity field has to vanish in the solid, thus there has to be a momentum sink which decelerates the flow in the solid. Accordingly, $\mathbf{S_U}$ reads

$$\mathbf{S_U} = \mathbf{S_b} + \mathbf{S_d} = \rho g \hat{\mathbf{e}}_y \beta \left(T - T_{ref}\right) + A\mathbf{U} \tag{2.4}$$

where

$$A = -\frac{C\left(1 - f_l\right)}{{f_l}^3 + e_0} \tag{2.5}$$

The first term (the thermal buoyancy) makes use of the Boussinesq approximation, where g is the gravitational acceleration constant, $\hat{\mathbf{e}}_y$ a unit vector pointing in the positive y-direction, and β the thermal expansion coefficient. The latter (the momentum sink) depends on the liquid fraction f_l, which is zero in the solid and unity in the liquid. The multiplier C is a constant, which is chosen to be large enough (= 10^6), whereas e_0 is a small constant (= 10^{-3}), to avoid the division by zero when the liquid fraction f_l is zero in the solid. In the solid, $\mathbf{S_d}$ acts as a dominant sink in the momentum equation, thus enforcing the zero velocity field. On the other hand, in the liquid zone, the above term vanishes and a velocity field is obtained using the other terms in the momentum equation (Brent et al. (1988)).

2.3.3 Energy source term

The energy source S_T accounts for the evolution of the latent heat during phase change. The latent heat is absorbed during solid-to-liquid (melting) phase change, whereas it is released during solidification. This term reads (Brent et al. (1988)):

$$S_T = -\left[\frac{\partial \rho \Delta H}{\partial t} + \nabla \cdot \left(\rho \mathbf{U} \Delta H\right)\right] \tag{2.6}$$

The latent heat ΔH is released or absorbed when the material undergoes a phase change. It changes from zero in the solid to the maximum value that equals the phase change latent heat L in the liquid, as shown in figure 2.2. This change can take place abruptly at one temperature, *i.e.* melting temperature T_m, or during a temperature interval, *i.e.* from solidus temperature T_s to liquidus temperature

T_l. The first is referred to as isothermal phase change, which is the case for pure material, while the latter is non-isothermal phase change, which is the case for alloyed material. For an isothermal phase change (figure 2.2 left), the convection of latent heat (the second term in Eq. 2.6) vanishes. For non-isothermal phase change (figure 2.2 right), the amount of latent heat is in general a function of the temperature in the interval (solid line). In this thesis, we assume that the latent heat follows a linear profile in the melting interval (dash line).

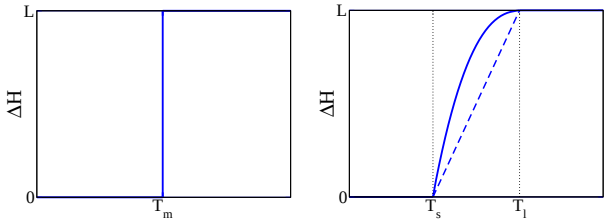

Figure 2.2. Evolution of latent heat ΔH for isothermal phase change (left) and non-isothermal phase change (right). For non-isothermal phase change, in the melting range ΔH is a non-linear (solid) or linear (dash) function of temperature.

Implementation of S_T makes use of the source term linearization technique (Patankar (1980), Voller et al. (1990), Voller and Swaminathan (1991)), where the non-linearities are accounted for through iterations after transforming this term into the following linear form:

$$S_T = S_P T + S_C \tag{2.7}$$

Eq. 2.6 can be rewritten as:

$$S_T = -\frac{\partial \rho f_l L}{\partial t} = -\rho L \frac{\partial f_l}{\partial T}\frac{\partial T}{\partial t} \tag{2.8}$$

where f_l is the liquid fraction and L the phase change latent heat. In Eq. 2.8, the convective term (second term in Eq. 2.6) is omitted for simplicity. For a linear profile of latent heat in the melting interval, the liquid fraction f_l reads:

$$f_l = \begin{cases} 0 & \text{if } T \leq T_s \\ \dfrac{T - T_s}{T_l - T_s} & \text{if } T_s < T < T_l \\ 1 & \text{if } T \geq T_l \end{cases} \tag{2.9}$$

Relating Eq. 2.8 and 2.7 (Voller and Swaminathan (1991)), the coefficients S_P and S_C in Eq. 2.7 are defined as:

$$S_P = -\frac{\rho L}{\Delta t}\frac{\partial \mathcal{F}}{\partial T} \tag{2.10}$$

and

$$S_C = -S_P \mathcal{F}^{-1} + \frac{\rho L}{\Delta t}\left(f_l^{\text{old}} - f_l\right) \tag{2.11}$$

Based on these equations, we can see that an iteration between temperature T and liquid fraction f_l takes place, where the superscript 'old' refers to the previous iteration level. $\mathcal{F}$ is the liquid fraction profile, function of temperature. The inverse function $\mathcal{F}^{-1}$ returns the temperature value for a given liquid fraction at the old iteration level. For a linear profile of f_l between T_s and T_l, $\partial\mathcal{F}/\partial T$ and $\mathcal{F}^{-1}$ are defined as:

$$\frac{\partial \mathcal{F}}{\partial T} = \frac{1}{(T_l - T_s)} \tag{2.12}$$

and

$$\mathcal{F}^{-1} = \mathcal{F}^{-1}(f_l) = f_l^{\text{old}}(T_l - T_s) + T_s \tag{2.13}$$

, respectively.

2.3.4 Boundary conditions

The boundary conditions used in the solid-liquid model are outlined here based on the dependent variables under consideration, *i.e.* velocity and temperature.

Velocity

At the liquid surface exposed to the atmosphere, the surface tension of the liquid-gas interface has to be taken into account. In a non-isothermal condition, the temperature difference along this boundary results in the gradient of surface tension. The tangential force driven by the surface tension gradient is balanced by the viscous force of the flow due to shear, *i.e.*

$$\mu \frac{\partial u}{\partial n} = \frac{d\sigma}{dT}\frac{\partial T}{\partial \tau} \tag{2.14}$$

where n and τ denote the normal and the tangential vectors to the boundary plane, respectively. The temperature gradient of surface tension $d\sigma/dT$ is a function of temperature and surface active element concentration.

Temperature

For the temperature (energy) equation, the following boundary condition is imposed at the liquid surface:

$$k\frac{\partial T}{\partial n} = q''_{in} - q''_{loss} \tag{2.15}$$

where q''_{in} accounts for influx from external heat, *e.g.* the laser beam, whereas q''_{loss} accounts for the heat lost to the environment, *e.g.* due to convection, radiation, or evaporation. At adiabatic walls, the boundary condition 2.15 reduces to a zero gradient type.

2.4 Solid-liquid-gas model

2.4.1 Governing equations

As already pointed out in section 2.2, as opposed to the solid-liquid model, in the solid-liquid-gas model the liquid-gas interphase is free to deform and not explicitly defined at mesh boundaries. Rather, it is smeared over several computational cells as a consequence of capturing this interface by using the Volume of Fluid method as will be discussed later. Consequently, the surface force acting on the liquid-gas interface, which translates as a boundary condition in the solid-liquid model (Eq. 2.14), has to be incorporated as a volume force in the interface cells. The same condition applies for the heat fluxes across the interface.

The governing equations for the solid-liquid-gas model are the following:

$$\frac{\partial \gamma}{\partial t} + \nabla \cdot (\gamma \mathbf{U}) = 0 \tag{2.16}$$

$$\frac{\partial \rho}{\partial t} + \nabla \cdot (\rho \mathbf{U}) = 0 \tag{2.17}$$

$$\frac{\partial \rho \mathbf{U}}{\partial t} + \nabla \cdot (\rho \mathbf{U}\mathbf{U}) = -\nabla p + \nabla \cdot (\mu \nabla \mathbf{U}) + \mathbf{S_U} + \mathbf{F_S} \tag{2.18}$$

$$\frac{\partial \left(\rho C_p T\right)}{\partial t} + \nabla \cdot (\rho \mathbf{U} C_p T) = \nabla \cdot (k \nabla T) + S_T + Q_T \tag{2.19}$$

Equation 2.16 is the Volume of Fluid model, in which the transport of the volume fraction γ is solved. This will be explained in subsection 2.4.2. The momentum and energy source terms which also appear in the solid-liquid model have been discussed in subsections 2.3.2 and 2.3.3, respectively. The smeared surface force $\mathbf{F_S}$ and the surface heat Q_T are discussed in subsection 2.4.3 and 2.4.4, respectively.

2.4.2 Volume of Fluid

General free surface modeling methods

In the simulations of multiphase flows, one of the main challenges lies in the prediction of the position and shape of an interface that separates the different phases. In general, approaches to predict the interface fall in three categories: (1) interface tracking; (2) interface fitting; and (3) interface capturing, as shown in figure 2.3. In the first approach, points located along the interface are tracked in time as they move (*e.g.* Tryggvason et al. (2001)). In the second (*e.g.* Egelja et al. (1998)), the grid boundaries are fitted to the interface. Both of these approaches usually fail when interface geometry becomes complicated. As opposed to these approaches, the interface capturing method employs the transport equation of a scalar indicating the phases of interest and implicitly captures the interface as the solution to the transport equation. Thus, it introduces no restriction on the interface evolution.

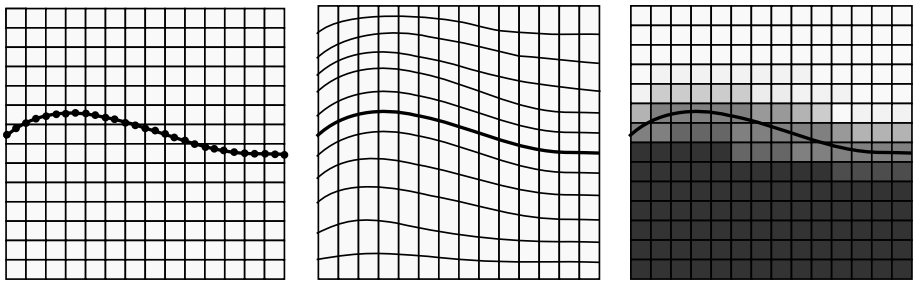

Figure 2.3. General classes of free surface modeling: interface tracking (left), interface fitting or moving mesh method (middle), and interface capturing (right).

The interface capturing method is exemplified by Level Set (LS) (Osher and Fedkiw (2002)) and Volume of Fluid (VOF) (Hirt and Nichols (1981)) methods. With LS, the interface is specified as the zero contour of a signed distance function. This function represents the distance between the cell centers and the interface. On the other hand, VOF solves the transport of volume fraction, which ranges from 0 to 1. The interface is represented by the transition region in the [0, 1] interval. In general, VOF leads to the smearing of interface, whereas LS can predict interface sharpness more accurately. Consequently, for flow involving surface tension, VOF may inaccurately predict the surface curvature and surface tension. However, VOF is superior to LS in that it guarantees a much better mass conservation. In this thesis, VOF is employed, with a special care given to minimize the associated interface smearing. This will be explained in the following sections.

Reformulation of the VOF model

In VOF, the transport of a scalar called volume fraction γ (Eq. 2.16) is solved (Hirt and Nichols (1981)). For a weld pool, the volume fraction ranges from 0 in the gas

phase to 1 in the (liquid or solid) base metal. The interface can be simply defined as a line of a constant volume fraction γ, commonly an isoline of γ=0.5. Nevertheless, when solving the VOF equation, one usually ends up obtaining a diffusive γ field, or a thick interface. This is a direct consequence of the numerical diffusion due to the discretization scheme for the convective term $\nabla \cdot (\gamma \mathbf{U})$. The remedy to this numerical diffusion seems to be straightforward, *i.e.* use of higher-order schemes. However, higher-order schemes do also pose a problem: the γ field goes unbounded, *i.e.* it suffers from undershoots and overshoots around the allowed minimum (γ = 0) and maximum (γ = 1) limits, respectively. Such unboundedness is intolerable, as it reflects an unphysical solution. Thus, one can devise a numerical scheme that blends the boundedness of low order schemes with the minimum diffusiveness of high order schemes, in order to obtain a sharp and bounded interface. Such blending is based on the approach of Normalized Variable Diagram (NVD) (Leonard (1991)). Several schemes, such as High Resolution Interface Capturing (HRIC) (Muzaferija et al. (1998)) and Compressive Interface Capturing Scheme for Arbitrary Meshes (CICSAM) (Ubbink and Issa (1999)), were developed on the basis of NVD. These NVD-based schemes will be discussed in subchapter 2.5.2.

The VOF model implemented in OpenFOAM does not use any of the above schemes or a blended scheme to get a non-diffusive, bounded γ field. Rather, an artificial compressive velocity in the vicinity of the interface is specified in order to compress the interface smearing by steepening the local gradient of γ (Berberović et al. (2009), Rusche (2002)). This is explained below.

The VOF model (Eq. 2.16) can be rewritten for a two-fluid Eulerian system (Cerne et al. (2001)):

$$\frac{\partial \gamma}{\partial t} + \nabla \cdot (\gamma \mathbf{U}_l) = 0 \tag{2.20}$$

$$\frac{\partial \gamma}{\partial t} + \nabla \cdot ((1-\gamma)\, \mathbf{U}_g) = 0 \tag{2.21}$$

where subscripts l and g refer to liquid and gas, respectively. Using the assumption that the influence of the liquid and gas velocities to the interface evolution is proportional to the corresponding volume fraction and that the effective fluid velocity is expressed as the following weighted average:

$$\mathbf{U} = \gamma \mathbf{U}_l + (1-\gamma)\, \mathbf{U}_g \tag{2.22}$$

then Eq. 2.20 can be rewritten as the evolution equation of volume fraction γ:

$$\frac{\partial \gamma}{\partial t} + \nabla \cdot (\gamma \mathbf{U}) + \nabla \cdot ((1-\gamma)\, \gamma \mathbf{U}_r) = 0 \tag{2.23}$$

where $\mathbf{U}_r = \mathbf{U}_l - \mathbf{U}_g$ is the relative velocity between the two phases, and here referred to as the "compression velocity".

Instead of the conventional VOF model (Eq. 2.16), Eq. 2.23 is in fact the equation used in OpenFOAM. It contains the additional convective term that depends on the compression velocity $\mathbf{U}_r$, which is only active in the interface cells, owing to the term $(1-\gamma)\,\gamma$. This artificial velocity helps compress the interface by minimizing the numerical diffusion of the volume fraction γ while maintaining its boundedness. Numerical treatment of this method is discussed in subsection 2.5.5. In addition, the volume fraction boundedness is maintained by utilizing a bounded scheme (*e.g.* Gamma scheme (Jasak et al. (1999))) combined with a solution procedure referred to as Multidimensional Universal Limiter for Explicit Solutions (MULES) (OpenCFD (2008)). This is outlined in subsection 2.5.6.

2.4.3 Surface forces

The surface forces are the driving force for the weld pool flow. These forces act at the weld pool surface as a consequence of the gradient of surface tension, which results from temperature and/or element concentration gradients. As opposed to the solid-liquid model, the surface forces in the solid-liquid-gas model (Eq. 2.18) are not implemented as boundary condition. Rather, they are imposed as smeared volume forces in the interface cells. The interface cells are here defined as the cells having a volume fraction between 0 and 1.

According to Brackbill et al. (1992), a surface force per unit area $\mathbf{f_s}$ can be transformed into a volumetric surface force $\mathbf{F_s}$ by means of a Delta function *i.e.*

$$\mathbf{F_s} = \mathbf{f_s}\delta = \mathbf{f_s}|\nabla\gamma| \tag{2.24}$$

which is non-zero in interface cells ($0 < \gamma < 1$) only.

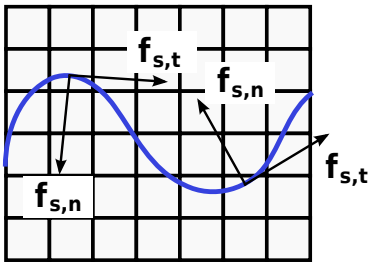

Figure 2.4. Illustration of normal and tangential components of surface force per unit area $\mathbf{f_s}$.

The surface force per unit area itself can be decomposed into the normal and the tangential components, as shown in figure 2.4. The normal component depends on the local value of surface tension as well as curvature, whereas the tangential

component is determined by the surface tension gradient. The expression is given as follows

$$\mathbf{f_s} = \mathbf{f_{s,n}} + \mathbf{f_{s,t}} = \sigma\kappa\mathbf{n} + \nabla_t\sigma \tag{2.25}$$

where κ is the curvature, $\mathbf{n}$ the surface normal vector, and ∇_t a tangential gradient operator. κ and $\mathbf{n}$ are defined as:

$$\kappa = -(\nabla \cdot \mathbf{n}) \tag{2.26}$$

and

$$\mathbf{n} = \frac{\nabla\gamma}{|\nabla\gamma|} \tag{2.27}$$

The tangential component $\nabla_t\sigma$ can be expressed as:

$$\nabla_t\sigma = \frac{d\sigma}{dT}\nabla_t T = \frac{d\sigma}{dT}\left[\nabla T - \mathbf{n}\left(\mathbf{n}\cdot\nabla T\right)\right] \tag{2.28}$$

Thus, combining Eq. 2.28, 2.25, and 2.24 yields

$$\mathbf{F_s} = \left[\sigma\kappa\mathbf{n} + \frac{d\sigma}{dT}\left(\nabla T - \mathbf{n}\left(\mathbf{n}\cdot\nabla T\right)\right)\right]|\nabla\gamma| \tag{2.29}$$

When implementing this expression for the volumetric surface forces into our numerical model, we first encountered a problem associated with a high flow acceleration in the less dense fluid phase. The typical density ratio in our simulations is 7000 (of steel) to 1 (of air). The smeared volume forces in the interface cells generated a high shear rate in the air phase, causing a very large velocity in this phase. This is also known as the spurious or parasitic currents, often encountered in VOF modeling of two-phase flows with a very large property gradient between both phases. This large velocity somehow forces the use of a very small time step in order for the simulation to be stable, which in turn slows down the computation. In order to avoid too high velocity in the air phase, we introduced a multiplier term into Eq. 2.29, which is now rewritten as follows

$$\mathbf{F_s} = \left[\sigma\kappa\mathbf{n} + \frac{d\sigma}{dT}\left(\nabla T - \mathbf{n}\left(\mathbf{n}\cdot\nabla T\right)\right)\right]|\nabla\gamma|\frac{2\rho}{(\rho_1+\rho_2)} \tag{2.30}$$

The term $2\rho/(\rho_1 + \rho_2)$ plays a role in redistributing the smeared forces toward the heavier phase (steel). Thus the resulting smeared forces tend to refrain from filling the air region in the vicinity of the interface and the aforementioned high acceleration flow in the air phase can be avoided. Such approach is also used by Brackbill et al. (1992).

2.4.4 Surface heat source

The heat source Q_T in Eq. 2.19 is due to the heating by the external laser beam. It is generally defined as

$$Q_T = q''_{in}\delta \tag{2.31}$$

where $\delta = |\nabla\gamma|$ implies that the surface heat influx q''_{in} is smeared over the interface cells.

However, using an analogous reason as for the smeared surface forces in subchapter 2.4.3, we also multiplied Eq. 2.31 with a factor to redistribute the heat input towards the steel phase, *i.e.*:

$$Q_T = q''_{in}\delta\frac{\rho C_p}{\rho_1 C_{p1} + \rho_2 C_{p2}} \tag{2.32}$$

The factor $\rho C_p/(\rho_1 C_{p1} + \rho_2 C_{p2})$ redistributes the heat input towards the region of higher ρC_p, *i.e.* steel.

2.4.5 Boundary conditions

To describe the boundary conditions more conveniently, the 2-D sketch of the solid-liquid-gas model (figure 2.1) is reused in figure 2.5. The boundaries in this model are the solid boundaries (bottom and solid sides) and the gas boundaries (top and gas sides).

Velocity

At the solid boundaries, the no-slip condition is imposed. At the gas boundaries, the pressure is specified. For a gas boundary with outflowing gas, a zero-gradient velocity condition is applied and the pressure equals a prescribed total reference value, whereas for a gas boundary with inflowing gas, a fixed value condition is used for the tangential velocity component and the pressure is adjusted using the dynamic pressure obtained from the velocity and density.

Temperature

The temperature boundary condition can be of the gradient type (Neumann boundary condition) as in Eq. 2.15, or of the fixed value type (Dirichlet boundary condition), depending on how the physical boundaries are interpreted. In this case, we use the Neumann type, where an adiabatic condition is imposed on the bottom, side gas, and side solid boundaries. At the top boundary, a radiative heat loss boundary condition is imposed.

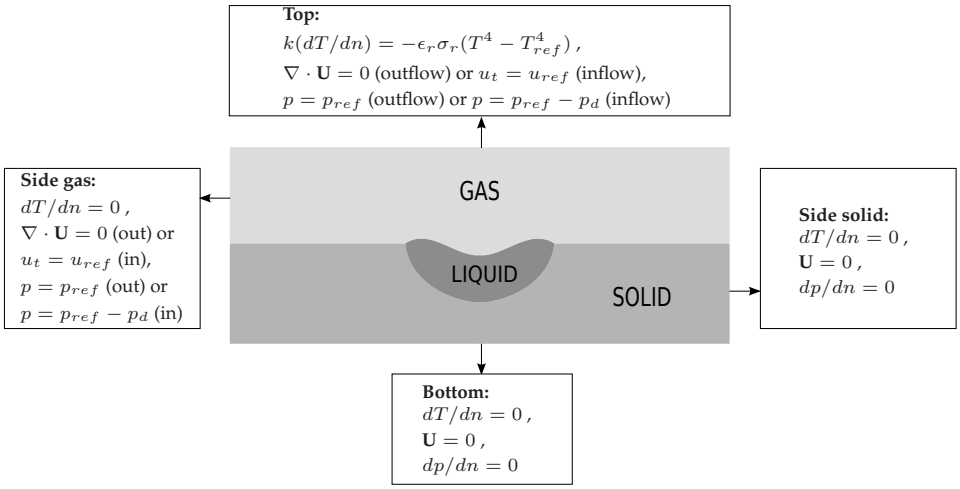

Figure 2.5. Boundary conditions for the solid-liquid-gas (free surface) model.

2.5 Finite Volume Method

The conservation equations Eq. 2.16, 2.17, 2.18, and 2.19 are solved numerically in this thesis by means of the Finite Volume Method (FVM). The principle behind this method is to integrate the conservation equations over a finite number of computational cells and to solve the equations in the integral form. The conservation equations can be rewritten in a general form (Ferziger and Perić (1996)), as follow:

$$\frac{\partial\left(\rho C_\phi \phi\right)}{\partial t} + \nabla \cdot \left(\rho C_\phi \phi \mathbf{U}\right) = \nabla \cdot \left(\Gamma_\phi \nabla \phi\right) + S_\phi \tag{2.33}$$

where ϕ is the generic variable, Γ_ϕ the diffusivity associated with the generic variable, and S_ϕ the source term. These quantities, for the conservation equations Eq. 2.16 - 2.19, are given in table 2.1.

General	ϕ	C_ϕ	Γ_ϕ	S_ϕ
VOF	γ	1	0	0
Mass	1	1	0	0
Momentum	U_i	1	μ	$S_{Ui} + F_{Si}$
Energy	T	C_p	k	$S_T + Q_T$

Table 2.1. Quantities of the terms in the general conservation equation

In order to write the generic conservation equation in the integral form, we transform the volume integral into the surface integrals summed up over all sides of the computational cells, according to the Gauss-Ostrogradsky's theorem:

$$\int_V \nabla \cdot \mathbf{f} dV = \int_S \mathbf{f} d\mathbf{S} \tag{2.34}$$

In this thesis, a 3-D Cartesian orthogonal structured grid is used. The associated control volume is shown in figure 2.6. Using such control volume, the volume integral term can then be converted into the following surface integrals:

$$\int_V \nabla \cdot \mathbf{f} dV = \int_{S_e} f_e dS - \int_{S_w} f_w dS + \int_{S_t} f_t dS - \int_{S_b} f_b dS + \int_{S_n} f_n dS - \int_{S_s} f_s dS \tag{2.35}$$

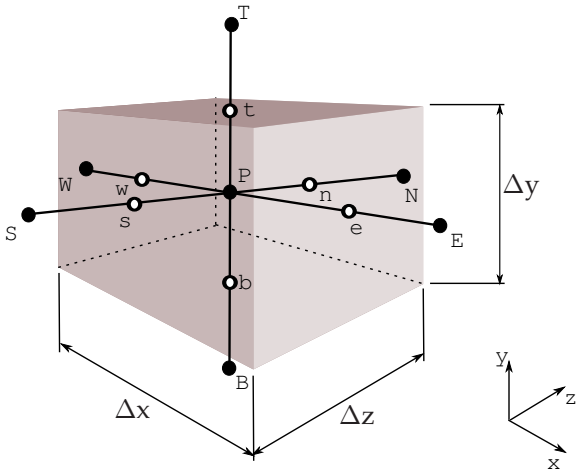

Figure 2.6. A typical control volume for a 3-D Cartesian orthogonal structured grid (Ferziger and Perić (1996)).

The generic equation (Eq. 2.33) can be rewritten in the integral form as follows:

$$\underbrace{\frac{d}{dt}\int_V \rho C_\phi \phi dV}_{\text{Unsteady}} + \underbrace{\int_S \rho C_\phi \phi \mathbf{U} \cdot d\mathbf{S}}_{\text{Convection}} = \underbrace{\int_S \Gamma_\phi \nabla \phi \cdot d\mathbf{S}}_{\text{Diffusion}} + \underbrace{\int_V S_\phi dV}_{\text{Source}} \tag{2.36}$$

2.5.1 Spatial discretization of the convection and diffusion fluxes

In the integral form of the general conservation equation Eq. 2.36, the convection term and the diffusion term can be rewritten as $\int_S \rho C_\phi \phi \mathbf{U} \cdot \mathbf{n} dS$ and $\int_S \Gamma_\phi \nabla \phi \cdot \mathbf{n} dS$, respectively. Here, $d\mathbf{S} = \mathbf{n} dS$, where $\mathbf{n}$ the surface normal vector pointing outward. The integrands of the convection and diffusion terms, denoted by $f^c = \rho C_\phi \phi \mathbf{U} \cdot \mathbf{n}$ and $f^d = \Gamma_\phi \nabla \phi \cdot \mathbf{n}$, respectively, are evaluated at the control volume surfaces, not at the control volume centers. This requires that the cell face values

and their gradients be known. In the CFD code used in this thesis, however, all dependent variables are stored at the cell centers. Accordingly, some interpolation is needed to express the cell face values in terms of the cell center values. Some most commonly used discretization schemes with different interpolation techniques are discussed below, namely Upwind Differencing Scheme (UDS), Central Differencing Scheme (CDS), and Quadratic Upwind (QUICK). Furthermore, a high resolution difference scheme based on Normalized Variable Diagram (NVD) used in OpenFOAM, called Gamma scheme, will be described in subchapter 2.5.2.

Upwind Differencing Scheme (UDS)

Suppose we want to approximate the cell face value at surface e in the control volume sketched in figure 2.6. Approximating ϕ_e by the nodal value upstream of face e is referred to as Upwind Differencing Scheme (UDS). This approximation reads:

$$\phi_e = \begin{cases} \phi_P & \text{if} \quad (\mathbf{U} \cdot \mathbf{n})_e > 0 \\ \phi_E & \text{if} \quad (\mathbf{U} \cdot \mathbf{n})_e < 0 \end{cases} \tag{2.37}$$

The solution to this approximation is always bounded, *i.e.* oscillatory solutions are always avoided. Nevertheless, the solution is only first-order accurate as shown by the leading truncation error term when applying Taylor series expansion for ϕ_e. Additionally, the solution is extremely diffusive, especially when the flow is oblique to the grid. The only way to minimize the numerical diffusion of UDS is by using a very fine mesh in the computation.

Central Differencing Scheme (CDS)

CDS approximates the cell face value ϕ_e by simply linearly interpolate between the two neighboring cell centers that share the face e.

$$\phi_e = \phi_E \lambda_e + \phi_P \left(1 - \lambda_e\right) \tag{2.38}$$

with the interpolation factor λ_e defined as:

$$\lambda_e = \frac{x_e - x_P}{x_E - x_P} \tag{2.39}$$

where x denotes the coordinate of the point considered.

If one applies Taylor series expansion for ϕ_e, it can be shown that CDS is second-order accurate, hence non-diffusive. However, the solutions obtained using CDS are unbounded, *i.e.* they oscillate, especially if the simulated problem is dominated by convection. (Patankar (1980)).

Quadratic Upwind Differencing Scheme (QUICK)

In CDS, it is assumed that linear variation applies between ϕ_P and ϕ_E. Leonard (1979) introduced the QUICK (Quadratic Upwind Interpolation for Convective Kinematics) scheme by improving the variability of ϕ between ϕ_P and ϕ_E from linear (straight line) to quadratic (parabola). This is achieved by making use of an extra upwind node: W or EE (one nodal point further to E in the positive x direction in figure 2.6), depending on the flow direction, when approximating ϕ_e. With QUICK, the following approximation holds:

$$\phi_e = \phi_U + g_1 (\phi_D - \phi_U) + g_2 (\phi_U - \phi_{UU}) \tag{2.40}$$

where now UU, U, and D represent the second upstream, the upstream, and the downstream node, respectively, *i.e.* W, P, and E if $(\mathbf{U} \cdot \mathbf{n})_e > 0$; or EE, E, and P if $(\mathbf{U} \cdot \mathbf{n})_e < 0$. The resulting coefficients g_1 and g_2 are associated with the distances between the connecting nodes:

$$g_1 = \frac{(x_e - x_U)(x_e - x_{UU})}{(x_D - x_U)(x_D - x_{UU})} \quad ; \quad g_2 = \frac{(x_e - x_U)(x_D - x_e)}{(x_U - x_{UU})(x_D - x_{UU})} \tag{2.41}$$

Similar to CDS, QUICK also suffers from unbounded solutions that can lead to stability problems in the computation.

2.5.2 Normalized Variable Diagram (NVD)-based schemes

Leonard (1991) introduced the concept of Normalized Variable Diagram, that laid a foundation of the bounded high-order schemes for the convective term of a transport equation. The idea behind NVD is to enforce solutions that comply with a constrain known as the Convective Boundedness Criterion (CBC) (Leonard (1991), Muzaferija et al. (1998), Ubbink and Issa (1999)). To illustrate this, the control volume sketch (figure 2.6) can be reintroduced as a 1-D sketch, say in the x direction, in figure 2.7. Suppose we focus on cell P and E, and the face they share, *i.e.* face e. The CBC states that the dependent variable of interest should remain smooth and be monotonically increasing or decreasing, *i.e.*: $\phi_P \leq \phi_e \leq \phi_E$ or $\phi_P \geq \phi_e \geq \phi_E$. By introducing a normalized variable $\tilde{\phi}$:

$$\tilde{\phi} = \frac{\phi - \phi_W}{\phi_E - \phi_W} \tag{2.42}$$

the CBC then reads: $\tilde{\phi}_P \leq \tilde{\phi}_e \leq 1$. Here, for simplicity we only consider the case of a monotonically increasing solution.

The NVD can be drawn as a plot of $\tilde{\phi}_P$ vs $\tilde{\phi}_e$, as in figure 2.8, in which the area that satisfies the CBC is hatched and bounded by solid lines. In the NVD, some common schemes are also mapped and it is obvious that the only scheme that satisfies

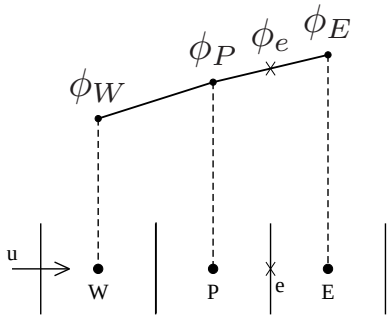

Figure 2.7. Illustration of Convective Boundedness Criterion in 1-D.

the CBC constraint is the 1st-order upwind scheme (UDS). The bounded high resolution schemes, such as CICSAM (Ubbink and Issa (1999)), HRIC (Muzaferija et al. (1998)), Minmod scheme (Harten (1983)), and Gamma scheme (Jasak et al. (1999), which is implemented in OpenFOAM), were developed such that their NVD plots lie in the allowed area that satisfies the CBC.

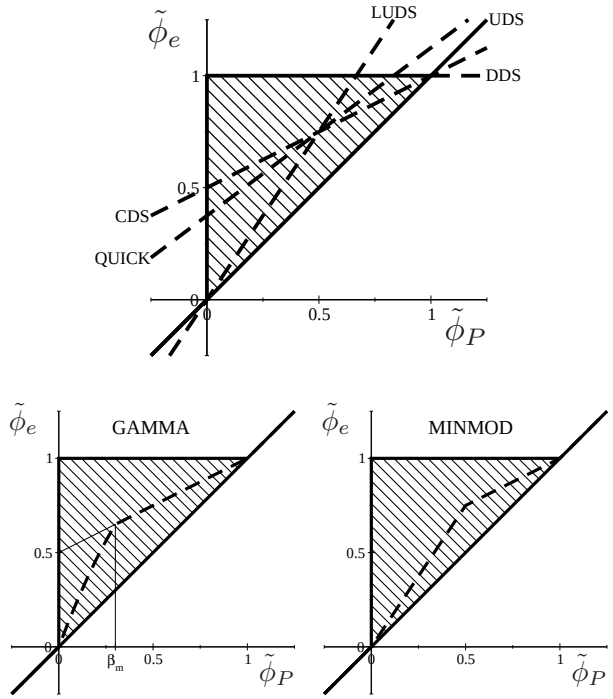

Figure 2.8. The Normalized Variable Diagram, with mapping of differencing schemes: UDS (1st-order upwind), DDS (1st-order downwind), CDS (central difference), QUICK, and LUDS (2nd-order upwind) (top); Gamma (bottom, left); and Minmod (bottom, right). The Convective Boundedness Criterion (CBC) is satisfied in the hatched area and solid lines.

Gamma scheme

The Gamma scheme (Jasak et al. (1999)) is proposed to facilitate the applicability of a bounded high resolution scheme on unstructured and/or non-uniform meshes. The normalized variable (Eq. 2.42) at the cell center P can be formulated in terms of the value at the downwind cell E and the gradient at P as follow:

$$\tilde{\phi}_P = 1 - \frac{\phi_E - \phi_P}{2(\nabla\phi)_P \cdot \mathbf{d}} \tag{2.43}$$

where $\mathbf{d}$ is a vector parallel with $\overline{PE}$ in figure 2.7. This formulation shows that the normalized variable can be calculated without including the value at the upwind cell W, as opposed to Eq. 2.42.

Based on Eq. 2.43, the following Gamma scheme is formulated:

$$\tilde{\phi}_e = \begin{cases} \tilde{\phi}_P & \text{if} \quad \tilde{\phi}_P \leq 0 \quad \text{or} \quad \tilde{\phi}_P \geq 1 \\ 0.5(1+\tilde{\phi}_P) & \text{if} \quad \beta_m \leq \tilde{\phi}_P \leq 1 \\ -0.5\gamma_e\tilde{\phi}_P + (1+0.5/\beta_m)\tilde{\phi}_P & \text{if} \quad 0 < \tilde{\phi}_P \leq \beta_m \end{cases} \tag{2.44}$$

where the blending factor is $\gamma_e = \tilde{\phi}_P/\beta_m$ and β_m is within the range: $0.1 \leq \beta_m \leq 0.5$. The Normalized Variable Diagram of this scheme is depicted in figure 2.8.

Minmod scheme

This scheme was first introduced by Harten (1983). Based on this scheme, $\tilde{\phi}_e$ is expressed as:

$$\tilde{\phi}_e = \begin{cases} \tilde{\phi}_P & \text{if} \quad \tilde{\phi}_P \leq 0 \quad \text{or} \quad \tilde{\phi}_P \geq 1 \\ \frac{1-\tilde{\xi}_e}{1-\tilde{\xi}_P}\tilde{\phi}_P + \frac{\tilde{\xi}_e - \tilde{\xi}_P}{1-\tilde{\xi}_P} & \text{if} \quad \tilde{\xi}_P \leq \tilde{\phi}_P < 1 \\ \frac{\tilde{\xi}_e}{\tilde{\xi}_P}\tilde{\phi}_P & \text{if} \quad 0 < \tilde{\phi}_P < \tilde{\xi}_P \end{cases} \tag{2.45}$$

where $\tilde{\xi}_e$ and $\tilde{\xi}_P$ are expressed as

$$\tilde{\xi}_e = \frac{x_e - x_W}{x_E - x_W} \quad ; \quad \tilde{\xi}_P = \frac{x_P - x_W}{x_E - x_W} \tag{2.46}$$

The Normalized Variable Diagram of this scheme is also shown in figure 2.8 (Alves et al. (2003)).

2.5.3 Discretization of the volume sources

The integral form of volume sources is discretized by the product of the mean value and the volume of the control volume. The mean value is approximated as the value at the cell center. Thus:

$$\int_{\Delta V} S_\phi dV = \overline{S}_\phi \Delta V \approx S_{\phi,P} \Delta V \tag{2.47}$$

2.5.4 Time integration schemes

The unsteady term in Eq. 2.36 can be discretized in either an explicit or an implicit manner. Because stability is of importance, in this thesis the unconditionally stable implicit scheme is used. The unsteady term can then be discretized using the following 1st-order implicit Euler method:

$$\frac{d}{dt}\int_{\Delta V} \rho C_\phi \phi dV = \frac{\Delta V}{\Delta t}\left[(\rho C_\phi \phi_P)^n - (\rho C_\phi \phi_P)^{n-1}\right] \tag{2.48}$$

where n and $n-1$ indicate the present and previous time step.

Alternatively, in order to improve the accuracy of the time discretization, a 2nd-order implicit Euler scheme can be used, *i.e.*:

$$\frac{d}{dt}\int_{\Delta V} \rho C_\phi \phi dV = \left[3\left(\rho C_\phi \phi_P\right)^n - 4\left(\rho C_\phi \phi_P\right)^{n-1} + 4\left(\rho C_\phi \phi_P\right)^{n-2}\right] \times \frac{\Delta V}{2\Delta t} \tag{2.49}$$

2.5.5 Numerical treatment of the VOF compression term

The discretization of the compression term in the reformulated VOF model (Eq. 2.23) requires the face value of the compression velocity. This velocity is calculated based on the maximum velocity magnitude in the interface region as well as its direction:

$$(\mathbf{U}_{r,f} \cdot \mathbf{S}_f) = n_f \text{min}\left[C_\gamma \frac{|\mathbf{U}_f \cdot \mathbf{S}_f|}{|\mathbf{S}_f|}, \text{max}\left(\frac{|\mathbf{U}_f \cdot \mathbf{S}_f|}{|\mathbf{S}_f|}\right)\right] \tag{2.50}$$

where $(\mathbf{U}_f \cdot \mathbf{S}_f)$ is the face volumetric flux, obtained from the pressure-velocity coupling. The face unit normal flux n_f is calculated based on the face-value volume fraction gradient:

$$n_f = \frac{(\nabla\gamma)_f}{|(\nabla\gamma)_f + \delta_n|} \cdot \mathbf{S}_f \tag{2.51}$$

A stabilization factor δ_n is used to account for the grid non-uniformity and expressed as:

$$\delta_n = \frac{\epsilon}{\left[\left(\sum_N V_i\right)/N\right]^{1/3}} \tag{2.52}$$

where N is the number of computational cells and ϵ a small number, here chosen as 10^{-8}.

This numerical treatment of the compression term in the VOF model ensures the following: Firstly, the relative (compression) velocity will be of the same order as the liquid phase velocity, if the gas phase velocity in the vicinity of the interface is small. Secondly, if the orders of magnitude of the velocities of both phases are equal, the interface compression strength is determined by the constant C_γ. If it is set to zero, no compression takes place. It can be increased to two (as used in this thesis) for a possible maximum compression.

2.5.6 Multidimensional Universal Limiter for Explicit Solutions (MULES)

MULES (OpenCFD (2008)) is a solution procedure that ensures boundedness of the volume fraction, based on the calculation of the flux correction as a difference between the higher-order limited flux obtained using *e.g.* the Gamma scheme (Jasak et al. (1999)) and the 1st order upwind flux. This corrected flux is subsequently limited in such a way that the new solution of volume fraction will be limited by the extrema in the neighboring cells (Berberović (2010)).

2.6 Solution procedure

In this section, it is described how the discretized equations are solved numerically. Emphasis is placed on how the solution procedure works in sequence, the pressure-velocity coupling, as well as the linear solvers.

2.6.1 Computation sequence

The two models used in this thesis, namely the solid-liquid and the solid-liquid-gas models, have their flowcharts, as outlined in figure 2.9 and 2.10, respectively. In general, the computation is always preceded by the pre-processing stage, in which the computational mesh is generated and its quality is assessed. The mesh generation results in all the geometrical information required for the spatial discretization by the Finite Volume Method in the main computation stage. Assessment of the mesh quality is an important part of the pre-processing stage, since only a mesh of a sufficient quality can lead to a good accuracy of the solution. The general rule-of-thumb is that a sufficiently fine resolution has to be applied to the

areas where pronounced gradients of the dependent variables occur, cell aspect ratio should be less than 5, and grid expansion factor should be less than 1.1.

In the main computation stage, the two models mainly differ in that the solid-liquid model does not require solving a Volume of Fluid equation, whereas the solid-liquid-gas model does. Additionally, the smeared surface forces and surface heat source have to be calculated in the solid-liquid-gas model. In the solid-liquid model, the surface force and the surface heat are simply imposed as boundary conditions. Moreover, the pressure-velocity coupling in the solid-liquid model is handled by the SIMPLE algorithm, while PISO is used for the solid-liquid-gas model. These two algorithms will be explained in subsection 2.6.2.

At the end of the computation, the time-dependent results are post-processed, normally by means of field visualization and plots of temporal history and spatial distribution of the dependent variables.

2.6.2 Pressure-velocity coupling

In the momentum conservation equation (Eq. 2.2 for the solid-liquid model, Eq. 2.18 for solid-liquid-gas model), we have a term representing the pressure gradient on the right hand side of the equations. Solving the momentum equations requires that the pressure distribution be known beforehand. However, the pressure differs from the other variables (velocities, temperature) in the sense that it does not have its own equation. To deal with this, pressure is normally derived from mass conservation (continuity) and momentum equations. Thus, the term pressure-velocity coupling is introduced.

Two main methods widely used in dealing with the pressure-velocity coupling are SIMPLE (Semi Implicit Method for Pressure-Linked Equations) (Patankar and Spalding (1972), Patankar (1980)) and PISO (Pressure Implicit with Splitting of Operators) (Issa (1986)). Both methods are used in OpenFOAM and shall be discussed in the following.

SIMPLE

The SIMPLE algorithm works iteratively as follow:

1. Set the boundary conditions.
2. Solve the discretized momentum equation to compute the guessed velocity field. This velocity field does net yet satisfy the continuity.
3. Compute the mass fluxes at the cells faces.
4. Solve the pressure equation and apply under-relaxation.
5. Correct the mass fluxes at the cell faces.
6. Correct the velocities based on the new pressure field.

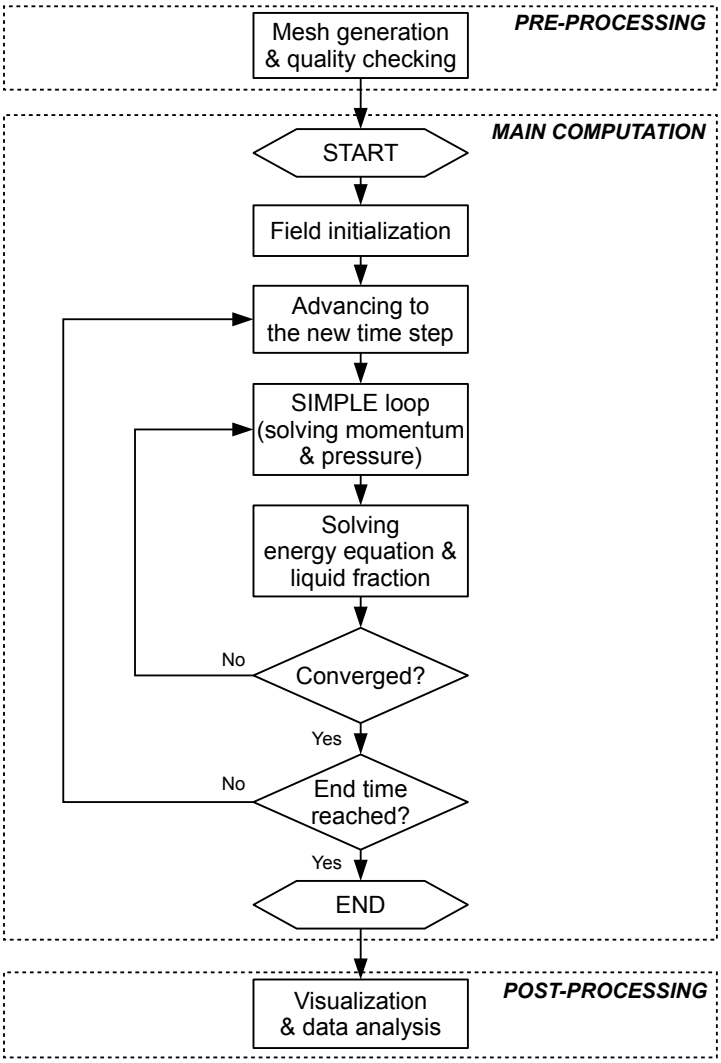

Figure 2.9. The flowchart of the solid-liquid model.

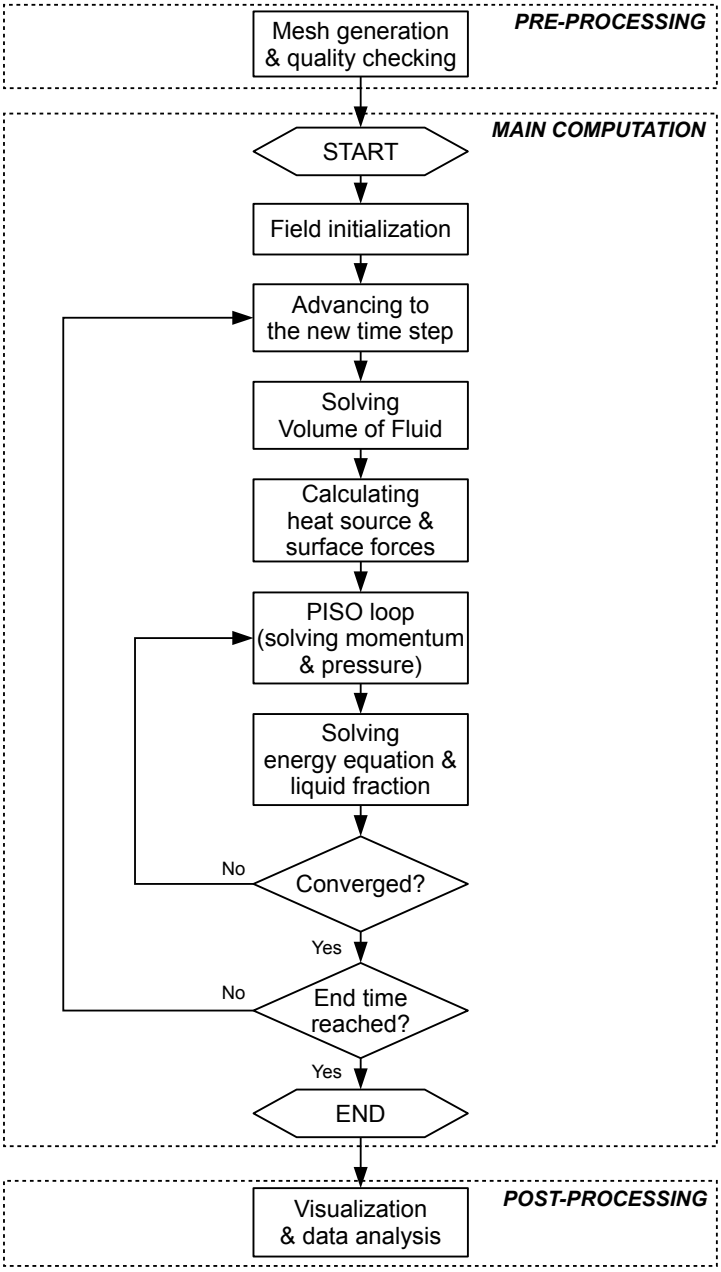

Figure 2.10. The flowchart of the solid-liquid-gas model.

7. Update the boundary conditions.
8. Repeat until convergence is reached.

PISO

PISO algorithm works almost similar as SIMPLE. It only differs from SIMPLE in that no under-relaxation is applied and that the momentum corrector step is performed more than once. This algorithm thus works as follow:

1. Set the boundary conditions.
2. Solve the discretized momentum equation to compute the guessed velocity field. This velocity field does net yet satisfy the continuity.
3. Compute the mass fluxes at the cells faces.
4. Solve the pressure equation.
5. Correct the mass fluxes at the cell faces.
6. Correct the velocities based on the new pressure field.
7. Update the boundary conditions.
8. Repeat from step 3 for a prescribed number of times.

2.6.3 Linear solvers

Through the Finite Volume discretization method described in this chapter, all the partial differential equations are transformed into their corresponding linear algebraic equations. Basically, each computational cell has one linear equation for one unknown generic variable ϕ (table 2.1). The linear equation systems have the general form of:

$$a_P \phi_P + \sum_{nb} a_{nb} \phi_{nb} = b \tag{2.53}$$

, which can be expressed in a matrix operation of:

$$\mathbf{A} \cdot \mathbf{\Phi} = \mathbf{b} \tag{2.54}$$

Here, $\mathbf{A}$ is a sparse matrix with the diagonal coefficients a_P and off-diagonal coefficients a_{nb}, $\mathbf{\Phi}$ the array of unknown generic variables ϕ, and $\mathbf{b}$ the array of source terms.

The matrix system in Eq. 2.54 is solved iteratively, *i.e.* a guess for the solution of ϕ is initially used and consecutively updated at the next iteration levels until a

convergence criteria is satisfied, *i.e.* the difference between solutions at two consecutive iterations fall below a prescribed tolerance. Many iteration techniques (linear solvers) have been developed to achieve the final solution with a high rate-to-convergence. In this thesis, the following linear solvers are employed (Saad (2003), OpenCFD (2008)):

1. Preconditioned Conjugate Gradient (PCG) with Geometric agglomerated Algebraic Multigrid (GAMG) preconditioner, for symmetric matrices.
2. Preconditioned Bi-Conjugate Gradient (PBiCG) with Diagonal-based Incomplete Lower-Upper (DILU) preconditioner, for asymmetric matrices.

2.7 OpenFOAM

OpenFOAM (Open Field Operation and Manipulation) is an open-source Computational Fluid Dynamics toolbox, licensed under the GNU General Public License (GPL). It is written in the C++ programming language and based on the object-oriented programming paradigm (Weller et al. (1998)). The concept of object-oriented programming allows for writing of the OpenFOAM solver as a hierarchy of so-called classes and functions, which are related to datasets and operations. These classes and functions can be deemed as *e.g.* variable fields, mesh, boundary conditions, numerical operators, etc. This offers a number of appealing advantages:

- By defining the numerical operators as classes, the governing transport equations can be written in a form that looks equivalent to the original mathematical formulation. As an example, in the top-level code of the free surface model, the momentum conservation equation (combining Eq. 2.18, 2.4, and 2.30), mathematically expressed as:

$$\begin{aligned}\frac{\partial \rho \mathbf{U}}{\partial t} + \nabla \cdot (\rho \mathbf{U}\mathbf{U}) \quad &= \quad -\nabla p + \nabla \cdot (\mu \nabla \mathbf{U}) + \rho g \hat{\mathbf{e}}_y \beta \left(T - T_{ref}\right) + A\mathbf{U} \\ &\quad + \left[\sigma \kappa \mathbf{n} + \frac{d\sigma}{dT}\left(\nabla T - \mathbf{n}\left(\mathbf{n} \cdot \nabla T\right)\right)\right] |\nabla \gamma| \frac{2\rho}{(\rho_1 + \rho_2)}\end{aligned} \tag{2.55}$$

, is implemented in OpenFOAM as:

```
fvVectorMatrix UEqn
(
    fvm::ddt(rho, U)
  + fvm::div(rhoPhi, U)
  - fvm::laplacian(muf, U)
  - (fvc::grad(U) & fvc::grad(muf))
  - dsigmadT*(fvc::grad(T) - nn*(nn & fvc::grad(T)))*mag(fvc::grad(gamma))*factor
  - fvm::Sp(A, U)
);

solve
```

```
(
  UEqn
  ==
  fvc::reconstruct
  (
      fvc::interpolate(rho*(scalar(1) - beta*(T-Tref)))*(g & mesh.Sf())
    + (
          fvc::interpolate(interface.sigmaK())*fvc::snGrad(gamma)
          *fvc::interpolate(factor)
        - fvc::snGrad(p)
      )*mesh.magSf()
  )
);
```

The energy equation (combining Eq. 2.19 and 2.7):

$$\frac{\partial\left(\rho C_p T\right)}{\partial t} + \nabla \cdot \left(\rho \mathbf{U} C_p T\right) = \nabla \cdot \left(k \nabla T\right) + S_P T + S_C + Q_T \tag{2.56}$$

is implemented as:

```
fvScalarMatrix TEqn
(
    fvm::ddt(rhoCp, T)
  + fvm::div(rhoPhiCp, T)
  - fvm::laplacian(fvc::interpolate(k), T)
  - fvm::Sp(Sp, T)
  ==
    Sc
);

solve( TEqn == QT );
```

The above example on the writing of momentum and energy equations in the top-level code shows that the main ingredients are the field objects (*e.g.* `U, rho, phi, muf, p, beta, g, sigmaK, gamma, T, QT`) and the numerical operators (`fvm::ddt`, `fvm::div`, `fvm::laplacian`, `fvc::grad`, `fvc::snGrad`, `fvc::interpolate`), regardless of the type of mesh (2-D or 3-D, structured or unstructured, orthogonal or non-orthogonal) and the mesh resolution being considered. This example also demonstrates the efficiency of the high-level programming used in OpenFOAM.

- The code can deal with arbitrary polyhedral meshes, structured or unstructured, orthogonal or non-orthogonal.
- The open-source nature of the code, not only in terms of its source code but also in terms of hierarchical structure of the classes, opens wide opportunities to expand its functionality and capability according to the user's or the programmer's interest.
- Inheritance of classes is possible. This gives much flexibility in extending the codes and the classes. For instance, the thermocapillary boundary condition in this thesis is inherited and extended from an existing free-slip boundary condition.

3 CHAPTER

Numerical Test Cases

3.1 Introduction

The distributed OpenFOAM package is released with a limited capability, but has a large potential and flexibility to be extended towards the simulation of complex fluid flow problems. We extended the basic OpenFOAM package to include various models for physical phenomena that are relevant in welding. This chapter deals with the numerical test cases, on which the extended OpenFOAM CFD code was validated. Each of the test cases is selected such that it is relevant for one of the physical phenomena dealt with in this thesis and not yet included in the released OpenFOAM package. The aspects considered in this chapter are:

- Melting phase change
- Single-phase Marangoni-driven flows
- Isothermal two-phase free surface flows
- Two-phase Marangoni driven flows
- Free surface Marangoni-driven flows with phase change

The governing equations associated with the above problems have been outlined in chapter 2.

3.2 Melting phase change

In this section, we consider a test case of melting of pure gallium in a 2-D rectangular cavity. This test case was originally reported by Brent et al. (1988). The general sketch of the problem is given in figure 3.1. The cavity is confined by two side walls, at fixed temperatures T_h and T_c, respectively with T_h above the melting temperature T_m, and T_c below T_m. The top and bottom walls are thermally

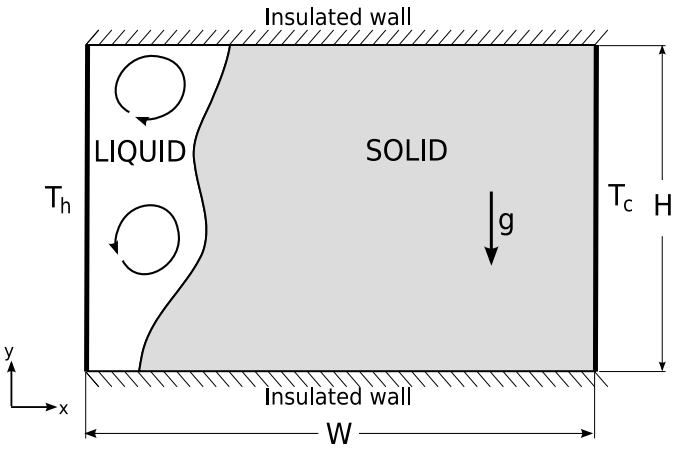

Figure 3.1. Sketch of gallium melting problem

insulated. Initially, the material inside the cavity is in solid state with temperature T_c. The physical properties and parameters are given in table A.1 in appendix A.

In the original paper on this problem, the simulation was performed on a coarse 42×32 mesh with an upwind difference scheme, which is only 1st-order accurate. This was simply because of the limitation of CPU power at the time the work was published. Hannoun et al. (2003), who tried to reproduce the simulation of Brent, argued that despite the good agreement with experimental results, Brent's result was not accurate because it was not a mesh-independent solution. We initially tried to simulate this case on a coarse mesh with 1st-order accurate upwind scheme as was done by Brent. In order to reach a mesh-independent solution, we also performed simulations on 4 different mesh resolutions as in Hannoun's paper: 280×200, 560×400, 840×600 and 1120×800, using 2nd-order central difference scheme.

The comparison of melting fronts obtained using our present OpenFOAM simulations, the simulations by Brent (mesh 42×32), and experiments by Gau and Viskanta (1986) is shown in figure 3.2 for time instants 2, 6, 15, and 19 minutes, respectively. All results are in a good agreement with each other. Close agreement is observed between OpenFOAM simulations and simulations by Brent, whereas the melting front obtained in the experiment propagates slower in the beginning and faster at later times.

The comparison of melting fronts and melt flow field for different mesh resolutions with 2nd-order central difference scheme is shown in figure 3.3. In contrast to the results obtained using the settings of Brent (coarse mesh, upwind scheme), the results on a finer mesh with higher order schemes show the formation of multiple convective rolls in the melt. This multiple rolls were also observed by Hannoun and some other authors (Dantzig (1989), Stella and Giangi (2000)). At the finest employed mesh resolution (1120×800), the melting front position agrees very well with experimental results of Gau and Viskanta (1986).

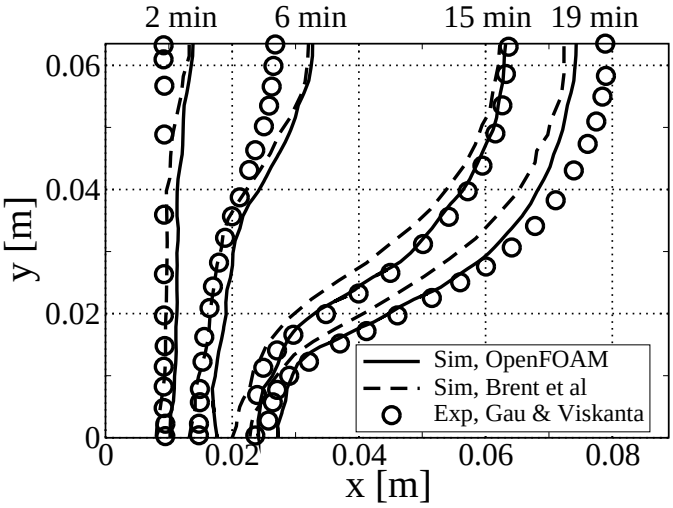

Figure 3.2. Comparison of melting front, mesh 42×32.

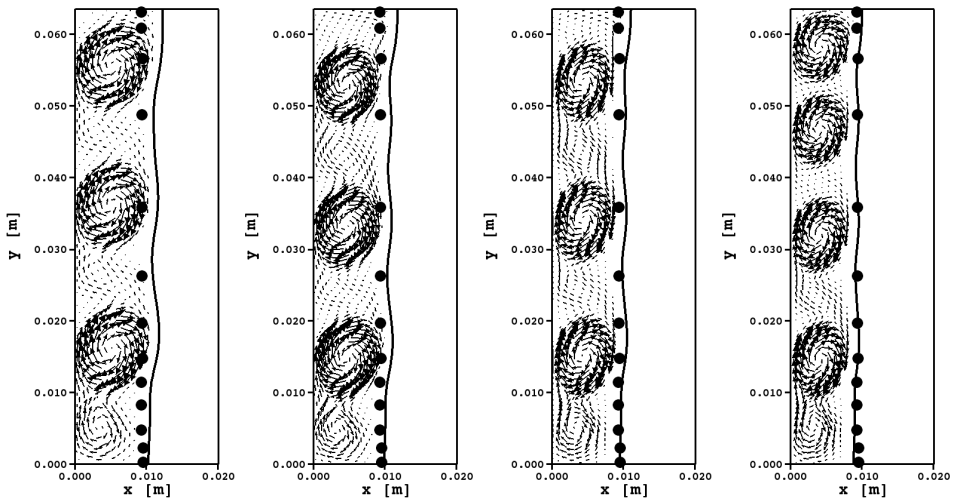

Figure 3.3. Simulated melt velocity field and melting front (solid line), and experimental melting front (circles, Gau and Viskanta (1986)) at t = 2 min, from left to right: mesh 280×200, 560×400, 840×600 and 1120×800, respectively.

3.3 Single-phase Marangoni driven flows

In this section, a benchmark problem of non-isothermal single-phase Marangoni driven flow serves to validate the implementation of the surface tension gradient (Marangoni) boundary condition for a flat surface, according to Eq. 2.14. The problem of interest is a liquid aluminum filled cavity confined by solid walls at its lateral sides and bottom, as shown in figure 3.4. The top surface is the free surface, which is exposed to the atmosphere. The cavity is heated from the left side, where the temperature of the left wall is fixed at T_h. The temperature of the right wall is fixed at T_c. The bottom wall is thermally insulated. At these three walls, the no-slip boundary condition holds. Due to the lateral heating, the horizontal temperature gradients at the top surface give rise to surface tension gradients, which balance the viscous force and consequently drive the flow in the cavity. Several assumptions are used in considering this problem. Firstly, the flow is laminar and steady. Moreover, the top free surface is assumed to be flat and non-deformable. Surface tension varies linearly with temperature, while density variation with temperature is considered by using the Boussinesq approximation. The other thermophysical properties are assumed to be constant and listed in table A.2. This testcase was reported by Bergman and Keller (1988).

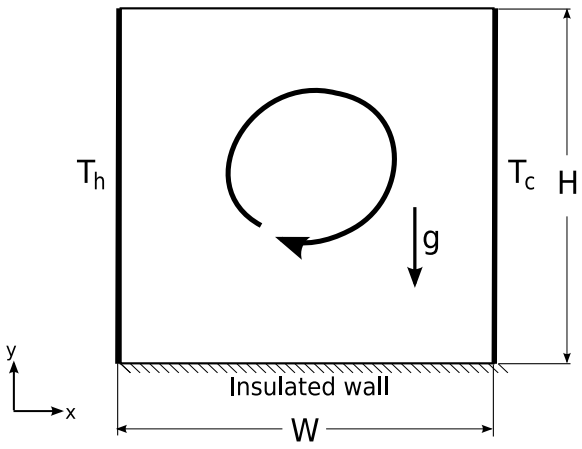

Figure 3.4. Sketch of Marangoni convection in a cavity problem

To demonstrate how surface tension gradients and buoyancy affect the flow direction in the cavity, three different simulation settings are used. The first setting concerns pure aluminum with constant surface tension, *i.e.* $\partial\sigma/\partial T = 0$. In the second case $\partial\sigma/\partial T = -3.5 \times 10^{-4}$, while in the third case $\partial\sigma/\partial T = +2.0 \times 10^{-4}$. The second case is associated with pure aluminum, whereas the third case is associated with aluminum-tin alloy, with a concentration of tin in the alloy of approximately 7 atomic percent. Except for $\partial\sigma/\partial T$, all other thermophysical properties are assumed to be equal to those of pure aluminum. In this test case, the relevant dimensionless numbers are the Marangoni (Eq. 1.1), Rayleigh (Eq. 1.2), Bond (Eq. 1.2), and Prandtl (Eq. 1.3) numbers.

The Prandtl and the Rayleigh numbers are Pr $= 0.0149$ and Ra $= 4.6 \times 10^4$, respectively. Additionally, the Marangoni and Bond numbers for case 1, 2, and 3 are 0 and ∞, 1.47×10^4 and 3.13, and 8.4×10^3 and 5.48, respectively.

Figure 3.5 shows the streamlines and isotherms in the cavity for the three different cases. For the neutral case (case 1), the thermocapillary force is absent, since there is no surface tension gradient. Thus the flow is driven solely by natural convection. For case 2, the negative value of $\partial\sigma/\partial T$ leads to a lower surface tension in the hot region (left part of the cavity) than that in the cold region (right part), thus driving the flow from left to right at the free surface, as can be seen from the closely-spaced streamlines and isotherms in the top-right corner of the cavity. On the other hand, the positive value of $\partial\sigma/\partial T$ in case 3 drives the flow at the free surface from right to left, which is in the opposite direction of the flow driven by natural convection. Consequently, two counter-rotating vortices exist for this case.

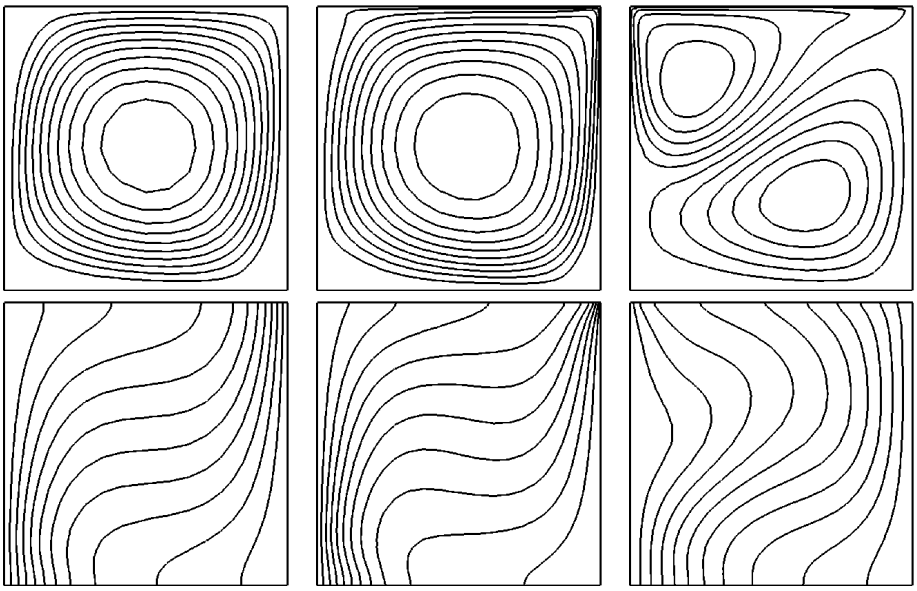

Figure 3.5. Streamlines (top) and isotherms with increment $\Delta T = 10K$ (bottom), for case 1 (left), case 2 (middle), and case 3 (right). Ranges of streamlines (ψ_{min}, ψ_{max}) are: (-8.95 $\times$ 10^{-8}, 1.37 $\times$ 10^{-9}) for case 1, (-1.26 $\times$ 10^{-7}, 2.88 $\times$ 10^{-9}) for case 2, and (-5.85 $\times$ 10^{-8}, 5.61 $\times$ 10^{-8}) for case 3.

In order to evaluate the role of the thermocapillary-driven flows in the heat transfer across the cavity, we calculated the local Nusselt number distributions at the hot and cold boundaries. The local Nusselt number is defined as

$$\mathrm{Nu} = \frac{hW}{k} \tag{3.1}$$

where W is the cavity width, k thermal conductivity, and

$$h = \frac{|k\partial T/\partial x|}{T_h - T_c} \tag{3.2}$$

The local Nusselt number distribution is shown in figure 3.6, in comparison with simulations by Bergman and Keller (1988). It is obvious that for case 2 (negative $\partial\sigma/\partial T$), the thermocapillary flow from left to right at the top part of the cavity enhances the local heat transfer rates at the cold wall. Additionally, the strong clockwise flow due to the thermocapillary effects increases Nu mainly along the bottom half of the hot wall due to the clockwise vortice. On the other hand, the coexistence of two counter-rotating vortices for case 3 (positive $\partial\sigma/\partial T$) results in a significant increase of heat transfer at the top part of the hot wall due to the anti-clockwise vortice, and a small increase at the bottom part of the hot wall due to the clockwise vortice. Here, the minimum increase takes place at around the mid-plane of the cavity because more heat is taken away in this region by the flow contributed by the two vortices.

The local Nusselt number distributions obtained by OpenFOAM simulation agree very well with results by Bergman and Keller (1988).

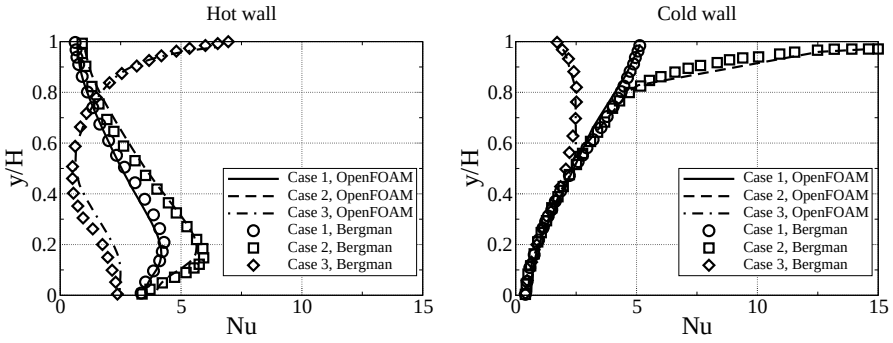

Figure 3.6. Local Nusselt number distributions at the hot and cold walls.

3.4 Isothermal two-phase free surface flows

The VOF method used in OpenFOAM to capture the interface between two fluids is tested on a benchmark problem of a water column collapsing in a gravitational field, as sketched in figure 3.7. This test case has been performed numerically by Waclawczyk and Koronowicz (2006), who applied the Compressive Interface Capturing Scheme for Arbitrary Meshes (CICSAM) and High Resolution Interface Capturing (HRIC) methods in their VOF approach. These two schemes are high-resolution advection schemes tailored to minimize the influence of artificial numerical dissipations as well as to maintain the boundedness of the VOF scalar. Prior to these authors, Colagrossi and Landrini (2003) applied Smoothed Particle

Hydrodynamics (SPH) methods on the same testcase and also provided experimental results.

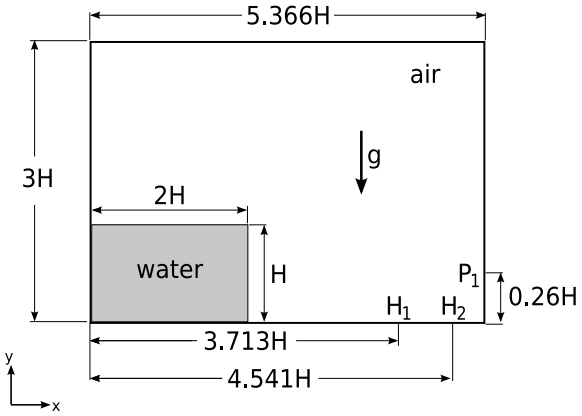

Figure 3.7. Problem sketch of collapse of a water column.

In figure 3.7, the initial water column height H=600 mm. The density and the dynamic viscosity for water are: $\rho_1 = 998$ kg/m^3, $\mu_1 = 10^{-3}$ kg/(m.s) and for air: $\rho_2 = 1.205$ kg/m^3, $\mu_2 = 1.81 \times 10^{-5}$ kg/(m.s). The simulation was performed on a 512 $\times$ 256 mesh resolution, with a maximum Courant number of 0.2. The time evolution of the collapse of the water column is shown in figure 3.8, in which the contour of the volume fraction is shown. The quantitative comparisons of water height level at point H1 and H2 as well as pressure values at point P1 (see figure 3.7) are given in figure 3.9 and 3.10, respectively. For these comparisons, the non-dimensional time $t^* = t\sqrt{g/H}$ is used.

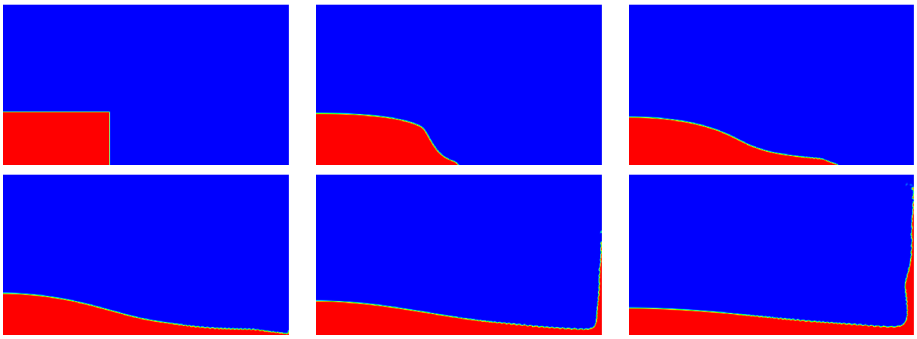

Figure 3.8. Time evolution of volume fraction γ, t = 0.0 - 1.0 s, with increment Δt = 0.2 s.

Comparison of water heights with experiment suggests that the onset of the water surface elevation at probes H1 ($t^* \sim 1.5$) and H2 ($t^* \sim 2$) are very well predicted. A good agreement is also found for the pressure increase at probe P1 at $t^* \sim 2.5$. In particular, the OpenFOAM simulation results agree well with results obtained using the HRIC scheme by Waclawczyk and Koronowicz (2006) with respect to the

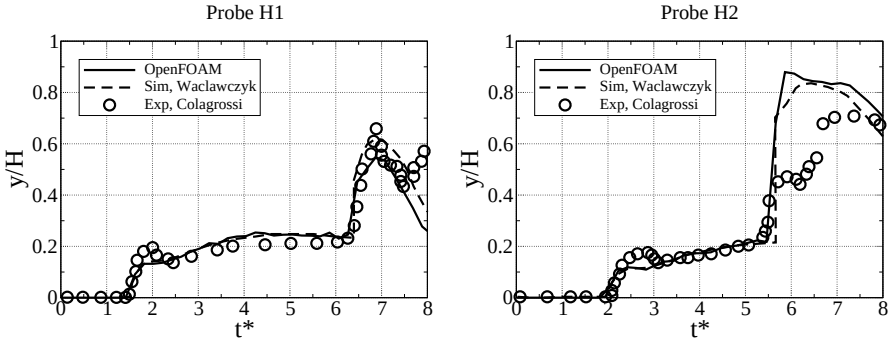

Figure 3.9. Time evolution of the water height at probes H1 and H2.

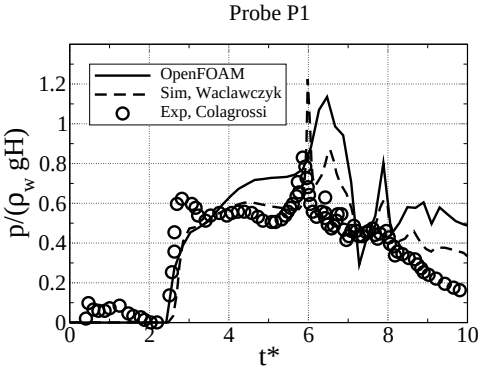

Figure 3.10. Time evolution of pressure at probe P1.

water heights, but both start to deviate slightly from the experimental data as the water hitting the right wall starts to overturn and break ($t^* \sim 5.5$ onwards). This deviation is also evident for the pressure data at probe P1. Nevertheless, the overall dynamics of the water collapse and breaking agrees quite well qualitatively with experiments.

3.5 Two-phase Marangoni driven flows

In this section, we validate the model on a thermocapillary driven flow problem in the presence of free surface deformation. The problem considered is a liquid in a two-dimensional cavity subjected to a lateral heating from the left wall, as sketched in figure 3.11. The liquid free surface is initially flat and located at a distance d from the bottom wall and the size of the cavity is $W \times H$. This problem is firstly reported in Sen and Davis (1982), who derived the analytical steady-state solution to the problem. Here, we perform the steady-state simulation of this problem with the following parameters and dimensionless numbers: Aspect ratio $A = d/W = 0.2$, Capillary number $\mathrm{Ca} = 0.008$, Marangoni number $\mathrm{Mg} = 0.2$, Reynolds number $\mathrm{Re} = 1$, and Prandtl number $\mathrm{Pr} = 0.2$. Here both the Rayleigh number Ra and Grashof number Gr are zero, because gravity is set to zero. A contact angle of 90 degrees is applied at the left and right walls. This problem was also simulated by a number of authors, *i.e.* Sasmal and Hochstein (1994), Hirt (1998), and Francois et al. (2006).

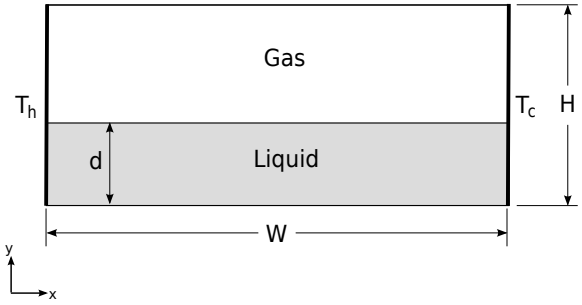

Figure 3.11. Sketch of non-isothermal two-phase Marangoni driven flows problem

The heating from the left wall causes a thermal gradient across the cavity, leading to a surface tension gradient at the free surface. The free surface flow results in a deformation of the interface. At steady state, the temperature and velocity fields obtained by OpenFOAM simulation are given in figure 3.12. To compare the solution more quantitatively, the free surface heights at the left and right walls reported in literature are outlined in table 3.1, in which it is shown that the OpenFOAM results agree well with those from literature. It is also notable that the results agree better with the analytical solution as mesh resolutions are increased.

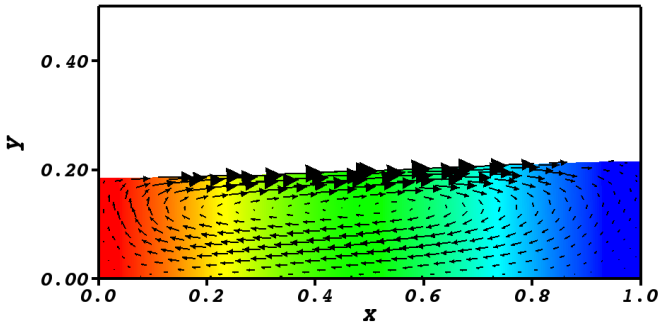

Figure 3.12. Temperature and velocity fields at steady state obtained from simulation of thermocapillary free surface problem.

Authors	**Dimensionless free surface heights**	
	Left wall	**Right wall**
Hirt (1998) (FlowScience, Inc.), simulation (mesh 21 × 10)	0.192	0.207
Sasmal and Hochstein (1994), simulation (mesh 34 × 31)	0.174	0.224
Francois et al. (2006), simulation (mesh 100 × 32)	0.187	0.209
Present, OpenFOAM (mesh 100 × 120)	0.187	0.208
Sen and Davis (1982), analytical	0.188	0.213

Table 3.1. Comparison of free surface heights (dimensionless) at left and right walls.

3.6 Free surface Marangoni-driven flows with phase change

When thermocapillary convection is combined with phase change and free surface deformation, a more complex system is obtained. Such a system is encountered in applications such as welding, casting, crystal growth, etc. In numerically modeling a system of this complexity, many researchers used the assumption of a flat, non-deformable liquid-gas interface (Liang and Lan (1997), Lan et al. (2000)). Some did take into account the interface deformation by means of a deformable mesh, but still neglected the gas phase dynamics (Rao and Shyy (1997)). Giangi et al. (2002) pointed out the importance of the gas phase above the liquid phase in affecting the heat transfer from the free surface, which influences the temperature gradients responsible for the flow.

Here, in order to demonstrate the capability of the developed OpenFOAM code in modelling such a system, we study the test case outlined in the paper by Tan et al. (2006). The test case model is the solid-liquid phase change of pure bismuth (Bi) in a 2-D container in a microgravity environment, as shown in figure 3.13. A gap of argon gas (Ar) with the height H_{Ar} is set above the bismuth melt with the depth d. The left wall temperature is held at constant hot temperature T_h, while the right wall temperature is set at constant cold temperature T_c. A decreasing linear temperature distribution from T_h to T_c is imposed at the top and bottom walls. The isoline of melting temperature T_m initially lies in between the left and right wall, *i.e.* at a distance x_m from the left wall. No-slip boundary conditions are imposed at all walls. The material properties of Bi and Ar, as well as the simulated parameters are outlined in table A.3.

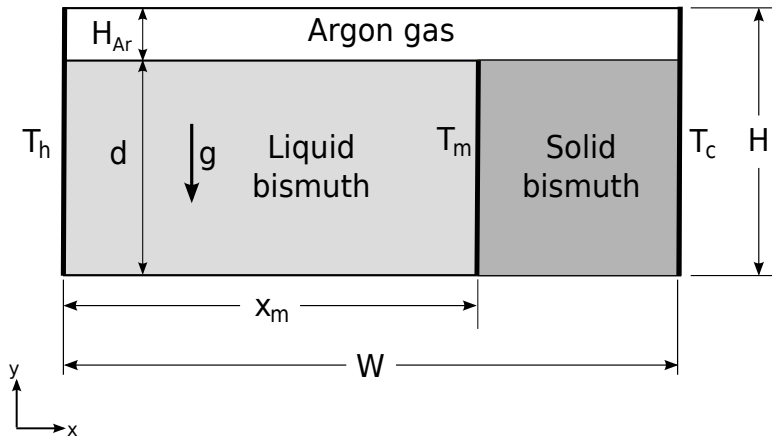

Figure 3.13. Problem sketch of free surface Marangoni-driven flows with phase change

The dimensionless numbers pertaining to this test case are Prandtl (Pr), Bond (Bo), Marangoni (Mg), Rayleigh (Ra), Capillary (Ca), and Stefan (Ste). The Bond number (Bo $= \rho g d^2/\sigma$) defines the ration of the hydrostatic restoring force of a deformed free surface to surface tension force. The Stefan number (Ste $= C_p \Delta T/L$,

where L is the latent heat of melting) represents the ratio of the sensible heat to the latent heat released or absorbed during phase change. The simulated test case is associated with Pr = 0.019 and Bo = 1.88 $\times$ 10^{-4}. Imposing a temperature difference $\Delta T = 12$ K between left and right walls gives Mg = 244, Ra = 0.031, Ca = 0.0022, and Ste = 0.033, respectively. The mesh resolution is 140 $\times$ 62, which is similar to what is used by Tan et al. (2006).

The steady state temperature and velocity fields are shown in figure 3.14. The horizontal temperature difference leads to a gradient of surface tension at the Bismuth-Argon interface, driving the surface flow away from the hot walls. The heat carried along the free surface melts the solid and helps push the liquid-solid interface. At the lower part of the melt the flow is driven away from this interface, causing a main clockwise recirculation zone. This main recirculation induces a weaker counterclockwise recirculation at the lower left corner of the melt. As for the gas phase, thermocapillary effects also form a recirculation zone, which does not go beyond the liquid-solid interface.

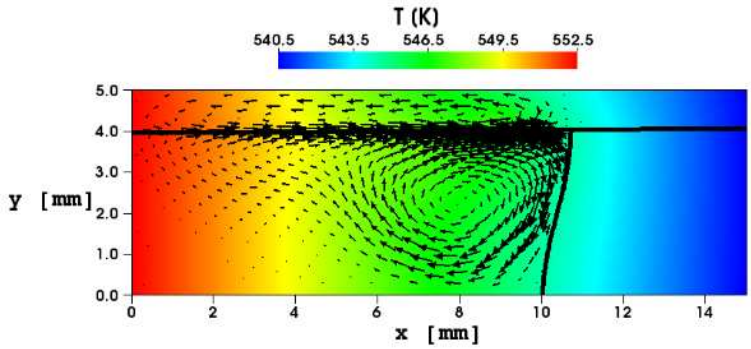

Figure 3.14. Temperature and velocity fields at steady state obtained from simulation of free surface Marangoni-driven flows with phase change.

Comparison of the liquid-solid interface between OpenFOAM results and results by Tan et al. (2006) is shown in figure 3.15. An excellent agreement is obtained in comparison with Tan's simulation.

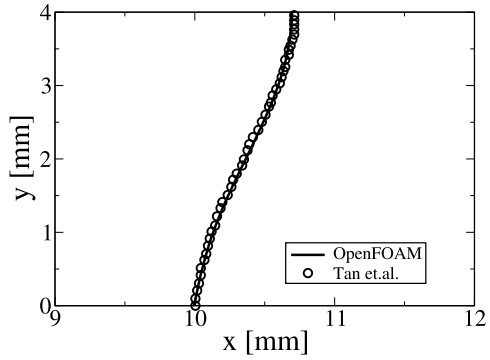

Figure 3.15. The shape of liquid-solid interface at steady state.

3.7 Concluding remarks

The validation of the developed OpenFOAM code has been described in this chapter. It can be concluded that the developed OpenFOAM code performs well and is sufficiently validated against a number of generic test cases, which are relevant to the simulation of weld pool hydrodynamics. Overall, good agreements are obtained when the OpenFOAM results are compared with other numerical simulation results and analytical solution. Slight discrepancies with experimental results do exist, but an explanation for these have been given. The good performance and validity of the code imply that it can be used to study the main subject of this thesis, *i.e.* weld pool hydrodynamics problem.

4 CHAPTER

Simulations of laser spot weld pool flows using flat surface assumption

4.1 Introduction

This chapter reports the simulations of laser spot weld pool hydrodynamics by employing a flat surface assumption. The study case is a problem reported by Pitscheneder et al. (1996). This work was focused on Böhler S705 steel with varying active element concentrations, in this case sulfur, and laser powers. The general conclusion was that the combination of sulphur concentration and laser power affects the surface tension gradient, thus the direction and strength of the Marangoni convective flow and eventually the weld pool shapes. Here, we repeat the same simulation for validation purpose, and we focus on two aspects not addressed in the work by Pitscheneder et al. (1996). First, we show the influence of using enhancement factors for thermal conductivity and viscosity as employed by Pitscheneder et al. (1996). Second, we demonstrate the necessity to incorporate the solidification stage into the simulation in order to have a more proper comparison with experimental results.

4.2 Problem description

The weld sample geometry was a disc of 15 mm radius and 15 mm thickness. Two sample steels are used, containing 20 and 150 ppm sulfur respectively. They were subjected to a non-moving CO_2 laser beam of 1.4 mm radius, with varying laser powers: 1900, 3850, and 5200 W. The absorptivity of the sample surface to the laser is 0.13. Irradiation times of 0.1, 0.25, 0.5, 0.75, 1, 3, 5, 10, and 15 s were used in the reference paper. The material properties are listed in table 4.1.

In their paper, Pitscheneder et al. (1996) used an enhancement factor of 7 for the molecular values of viscosity and liquid thermal conductivity *i.e.* the known values of the molecular viscosity and thermal conductivity were multiplied by a factor 7 in the simulations. They used such an approach to account for the enhanced

Properties	Values	Units
Density	8100	kg/m^3
Melting temperature	1620	K
Dynamic viscosity	0.006	$kg/(m \cdot s)$
Thermal conductivity of solid	22.9	$J/(m \cdot s \cdot K)$
Thermal conductivity of liquid	22.9	$J/(m \cdot s \cdot K)$
Enhancement factor for viscosity and liquid thermal conductivity	7.0	-
Specific heat of solid	627	$J/(kg \cdot K)$
Specific heat of liquid	723.14	$J/(kg \cdot K)$
Latent heat of melting	2.508×10^5	J/kg

Table 4.1. Material properties for the laser spot welding validation test case.

heat and mass transfer caused by the instabilities in the weld pool flow. This approach is clearly very rudimentary, and has no sound physical basis. Nevertheless, initially in this chapter we use the same approach of viscosity and thermal conductivity enhancements as used by Pitscheneder et al. (1996), solely for validation purpose.

4.3 Simulation settings

4.3.1 Mesh generation

For the simulation, a 2-D axisymmetric coordinate system is used. Pitscheneder et al. (1996) used a non-uniform mesh with 50 cells and a minimum cell size of 0.1 mm in the radial direction and 60 cells and a minimum cell size of 0.01 mm in the vertical direction. We generated a mesh of slightly different resolution (60×90), as shown in figure 4.1, giving minimum cell sizes in the radial and the vertical directions of 0.07 mm and 0.04 mm, respectively. Additionally, we generated two other meshes of higher resolution (85×125 and 110×160) in order to study the sensitivity of our numerical results to mesh resolutions. The minimum cell sizes in these refined meshes are 0.046 mm and 0.027 mm, and 0.035 mm and 0.02 mm, respectively.

In OpenFOAM, a 2-D axisymmetric mesh is defined as a wedge mesh in a 3-D Cartesian coordinate system, with only one cell occupying the third direction, as shown in figure 4.1. There is no need to transform the governing equations in 3-D Cartesian to axisymmetric coordinate system, as OpenFOAM automatically handles the proper numerical treatment, as long as a 2-D axisymmetric geometry is prescribed.

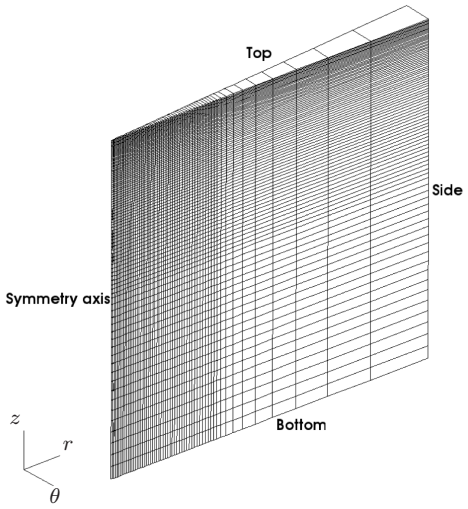

Figure 4.1. Basic ($n_r \times n_z = 60 \times 90$) 2-D axisymmetric mesh used for model validation.

4.3.2 Boundary conditions

At the top boundary, the boundary condition accounting for the balance between Marangoni stress and viscous stress (Eq. 2.14) is used. Additionally, the laser heat flux at the top surface is incorporated by Pitscheneder et al. (1996) as thermal boundary condition according to Eq. 2.15, except that the heat loss is neglected. They also assumed that the flux distribution has a top-hat profile. Accordingly, the thermal boundary condition (Eq. 2.15) can be written as:

$$k\frac{\partial T}{\partial n} = q''_{in}(r) = \begin{cases} \dfrac{\eta Q}{\pi r_q^2} & \text{for} \quad r \leq r_q \\ 0 & \text{for} \quad r > r_q \end{cases} \tag{4.1}$$

where r is the radial coordinate, Q the laser power, η the laser absorptivity, and r_q the laser beam radius.

At the symmetry boundary, the following boundary conditions are imposed:

$$\frac{dT}{dr} = 0 \quad ; \quad \frac{dv}{dr} = 0 \quad ; \quad u = 0 \tag{4.2}$$

where u and v are velocity components in radial and vertical directions, respectively.

No-slip boundary conditions are imposed at the solid boundaries (side and bottom). As for the thermal boundary conditions, they were not described in Pitscheneder et al. (1996). However, since the side and bottom boundaries seem to be far enough from the weld pool that they are unlikely to be affected by the weld pool heat, we used an adiabatic condition for these boundaries.

4.3.3 Temperature gradient of surface tension

Since the main focus is on the investigation of the effects of sulfur on the weld pool flow and shape, the dependence of surface tension on temperature and sulfur concentration needs to be known. A theoretical model by Sahoo et al. (1988) provides a basis for the calculation of the temperature gradient of surface tension ($d\sigma/dT$) as a function of temperature and sulfur activity, as shown in figure 4.2 for 20 and 150 ppm sulfur. The formulation of the model is given by:

$$\frac{d\sigma}{dT} = \frac{d\sigma}{dT}\Big|_0 - R\Gamma_S \ln(1 + Ka_i) - \frac{Ka_i}{(1 + Ka_i)} \frac{\Gamma_S(\Delta H^0 - \Delta \overline{H}_i^M)}{T} \tag{4.3}$$

$$K = k_1 \exp\left[\frac{-\Delta H^0}{RT}\right] \tag{4.4}$$

Here, $\frac{d\sigma}{dT}\Big|_0$ is the value of temperature gradient of surface tension for pure metal, Γ_S the surface excess at saturation, K the equilibrium constant for segregation, k_1 entropy factor, ΔH^0 the standard heat of adsorption, $\Delta \overline{H}_i^M$ the partial molar enthalpy of species mixing in the solution, and a_i the activity of the element in % weight. The values of these parameters for Fe-S system are listed on table 4.2. Thus, the two plots in figure 4.2 can be obtained by substituting the values of these parameters into Eq. 4.3 and 4.4, with sulfur activities a_i of 0.002 %-wt (20 ppm) and 0.015 %-wt (150 ppm), respectively.

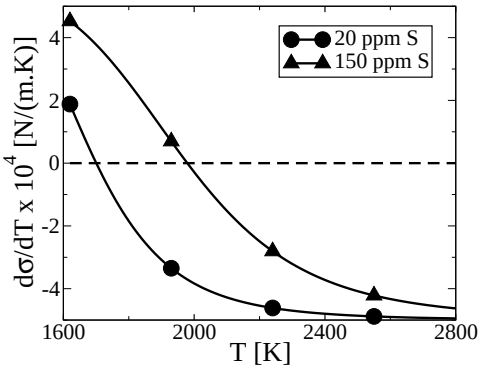

Figure 4.2. Temperature gradient of surface tension as a function of temperature for samples with 20 and 150 ppm sulfur.

Parameters	Values	Units
$\frac{d\sigma}{dT}\Big\vert_0$	-5.0 $\times$ 10^{-4}	N/(m $\cdot$ K)
Γ_S	1.3 $\times$ 10^{-8}	kmole/m^2
k_1	0.00318	-
ΔH^0	-1.66 $\times$ 10^8	J/(kmole)
$\Delta \overline{H}_i^M$	0	J/(kmole)

Table 4.2. Parameters for the calculation of temperature gradient of surface tension for Fe-S system.

4.3.4 Numerical schemes

The transport equations (Navier - Stokes and energy, *i.e.* Eq. 2.1 - 2.3) are spatially discretized using a higher-order NVD scheme with Minmod flux limiters. The transient terms are integrated using a first-order fully implicit scheme. The typical time step is 0.001 s, with a maximum Courant number allowed of 2. Convergence is reached when the residuals of pressure, temperature, and velocity are lower than 10^{-8}, and a minimum number of iteration per time step of 60 is used. Stricter convergence criteria did not lead to any changes in flow.

4.4 Validation against reference case

4.4.1 Mesh sensitivity analysis

In order to study the sensitivity of our numerical solutions to grid size, simulations on three different mesh resolutions were performed. The positions of the melt front at t = 5 s, for these three resolutions, with a laser power of 5200 W, are plotted in figure 4.3. The melt front positions are defined as the isolines of the melting temperature. In this figure, increasing the mesh resolution from 60 $\times$ 90 to 85 $\times$ 125 only very slightly alters the solution. Moreover, increasing the resolution further to 110 $\times$ 160 almost does not lead to any change in the melt front position. Accordingly, we concluded that a 85 $\times$ 125 mesh gives a mesh independent solution, and we use it for our further simulations.

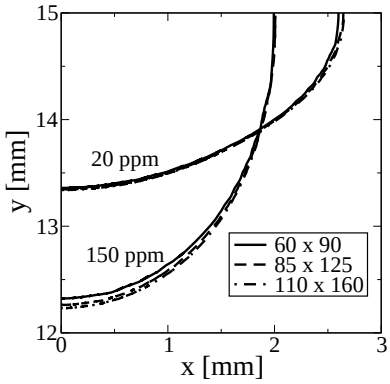

Figure 4.3. Position of the melt front at t = 5 s, laser power 5200 W, for three mesh resolutions: 60 $\times$ 90, 85 $\times$ 125, and 110 $\times$ 160.

4.4.2 Comparison with 3-D case

In addition to simulations on a 2-D axisymmetric coordinate system, we also examined the model on a full 3-D Cartesian coordinate system. The 3-D simulation is performed in order to check whether or not the results are equivalent to those of the 2-D axisymmetric case.

For our 3-D simulation, we used the same mesh resolution as that in the 2-D case by which we obtained a mesh independent solution, *i.e.* 85 $\times$ 125, in radial and vertical direction, respectively. The 3-D mesh is shown in figure 4.4.

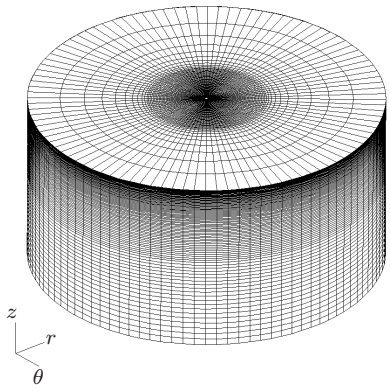

Figure 4.4. 3-D mesh used for model validation ($n_r = 85$, $n_z = 125$, $n_\theta = 100$).

The melt front and flow field at t = 5 s for the case of 20 ppm S, 5200 W obtained from the 3-D and 2-D simulations are shown in figure 4.5 (left). Additionally, we also compared the spatial distribution of temperature and velocity magnitude along a vertical line in the weld pool, approximately halfway between the symmetry axis and the weld pool edge (*i.e.* at r = 1 mm from the symmetry axis) at 5 s (figure 4.5 (right)). It is clear that 3-D and 2-D results show excellent agreements. This implies that the weld pool flow (using flat surface assumption) is axisymmetric, justifying the widely used 2-D axisymmetric coordinate system for flat surface weld pool simulations in literature.

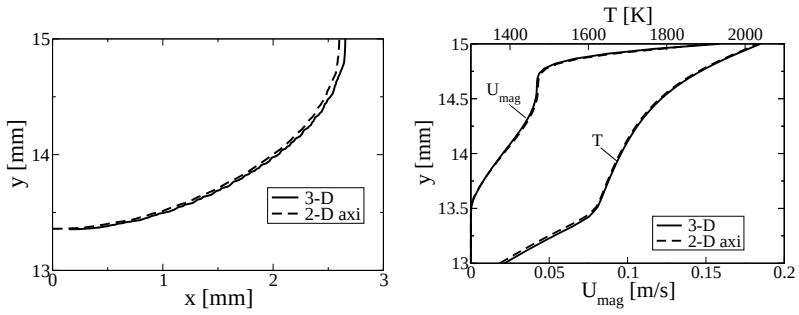

Figure 4.5. Comparison of melt front positions (left) and temperature and velocity magnitude distributions along a vertical line at r = 1 mm (right), between 3-D and 2-D axisymmetric simulations, for case 20 ppm S, 5200 W, t = 5 s.

4.4.3 Relation between temperature gradient of surface tension and Marangoni flow directions

Analysis of Marangoni driven flow requires an understanding of relation between surface tension gradient and flow directions. As the surface tension is a function of temperature and element concentration, assessment of this dependence is needed. This is illustrated in figure 4.6 for three types of possible dependency of the surface tension on temperature, and the corresponding weld pool flows. At a low element concentration, the temperature gradient of surface tension ($d\sigma/dT$) is generally negative over the entire weld pool temperature range (figure 4.6, top). This implies that the surface tension is lower in the high temperature region (weld pool center) than in the low temperature region (weld pool edge). As a consequence, flow along the liquid surface occurs from the weld pool center to the edge (outward flow). As element concentration is increased, a condition where $d\sigma/dT$ is positive in the low temperature range (weld pool edge), yet negative in the high temperature range (weld pool center), may arise. This is depicted in (figure 4.6, middle). In such case, flow in the center is outward, whereas at the edge it is inward. The two counter-rotating flows converge at some radius where surface tension reaches its maximum, or where $d\sigma/dT$ is zero. If the element concentration is increased further such that a positive $d\sigma/dT$ is satisfied everywhere in the

weld pool (figure 4.6, bottom), an inward flow occurs from the edge (low surface tension) to the center (high surface tension).

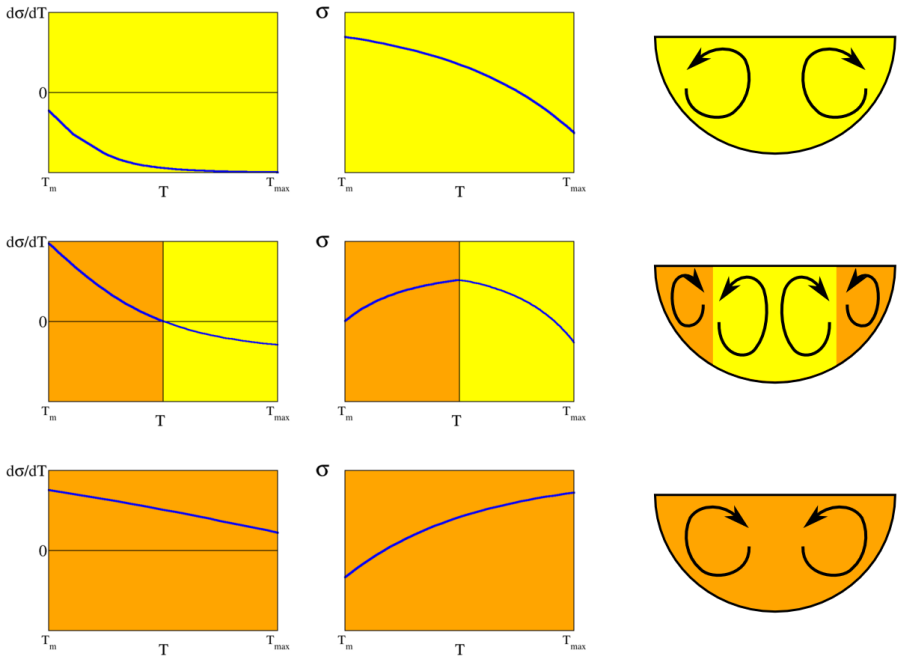

Figure 4.6. Illustration of the relation between the temperature gradient of surface tension between the melting temperature T_m and the maximum weld temperature T_{max}, and the Marangoni flow directions.

4.4.4 Effects of sulfur concentrations on weld pool shapes

The weld pool shapes and flows at t = 5 s are shown in figure 4.7 for different parameters. With a laser power of 1900 W, the weld pools containing 20 ppm and 150 ppm sulfur have identical shapes. However, when the laser power is increased to 3850 W and 5200 W, the shapes of the two weld pools with different sulfur contents are obviously different, where the welds with 150 ppm S have a larger penetration depth than those of 20 ppm S. With a laser power of 1900 W, the maximum temperature in the weld pool surface is low, resulting in a low surface tension gradient. Consequently, the Marangoni driven flows have low velocities and are associated with small Peclet numbers (~ 0.3 and ~ 1, for 20 and 150 ppm, respectively), which means that convection does not play a big part in the heat transfer inside the weld pool, regardless of the amount of sulfur content (hence flow directions). On the other hand, at higher laser power the surface tension gradients are larger, such that Marangoni convection becomes dominant, as shown by the increase in maximum velocities. This results in high Pe (> 10), indicating dominance of convection over conduction, and the direction of the Marangoni stress

becomes important in affecting the weld pool shapes. The direction of Marangoni stress depends on the sulfur concentration. At 20 ppm S, as shown in figure 4.2, the temperature gradient of surface tension $d\sigma/dT$ is mostly negative in the temperature range of the weld pool. This implies that surface tension in the hot zone (center of the weld pool) is lower than that in the weld pool edge, and the surface flow moves outward, resulting in wide but shallow weld pools. In contrast, at 150 ppm S, $d\sigma/dT$ is mostly positive in the temperature range of the weld pool and an opposite direction of the weld pool flow is obtained.

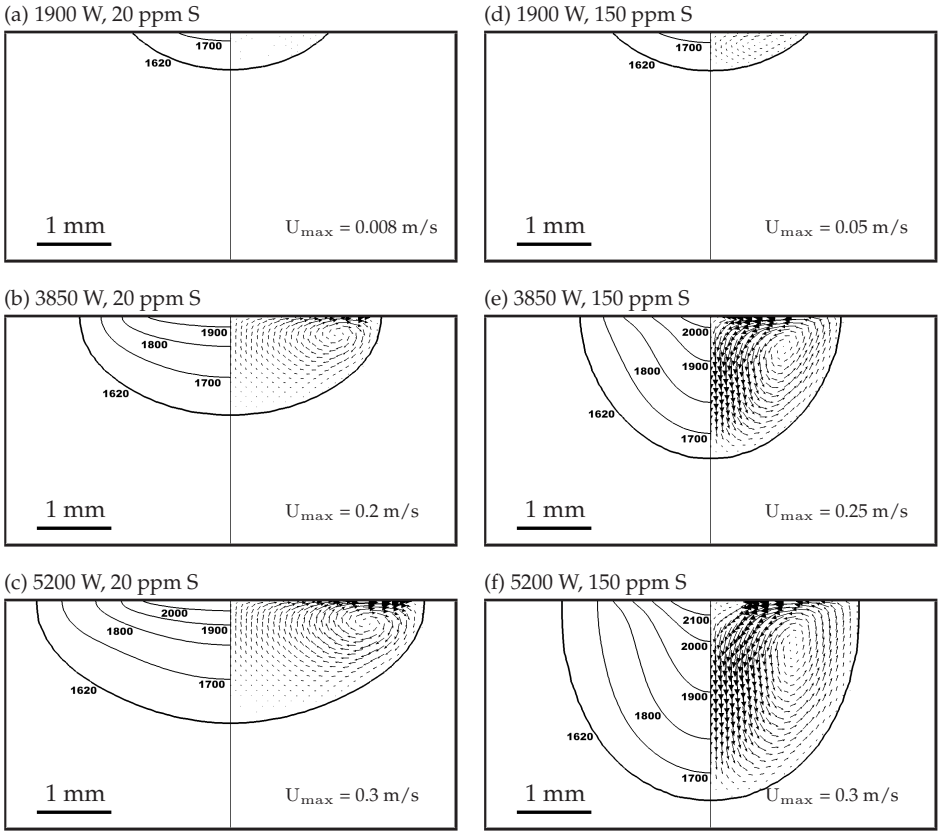

Figure 4.7. Simulated weld pool temperature (left) and velocity (right) fields at t = 5 s for 20 ppm sulfur (a - 1900 W; b - 3850 W; c - 5200 W) and 150 ppm sulfur (d - 1900 W; e - 3850 W; f - 5200 W).

Comparisons of the predicted weld pool shapes with experimental and simulation results by Pitscheneder et al. (1996) are shown in figure 4.8, for laser power 1900, 3850, and 5200 W at t = 5 s. Furthermore, more quantitative comparisons in terms of time history of weld pool depth and width are shown in figure 4.9, for 5200 W. It is evident from these comparisons that our simulation results agree well with the results of Pitscheneder et al. (1996). This brings about a confidence that

the developed OpenFOAM code is well validated for weld pool flow under flat surface assumption.

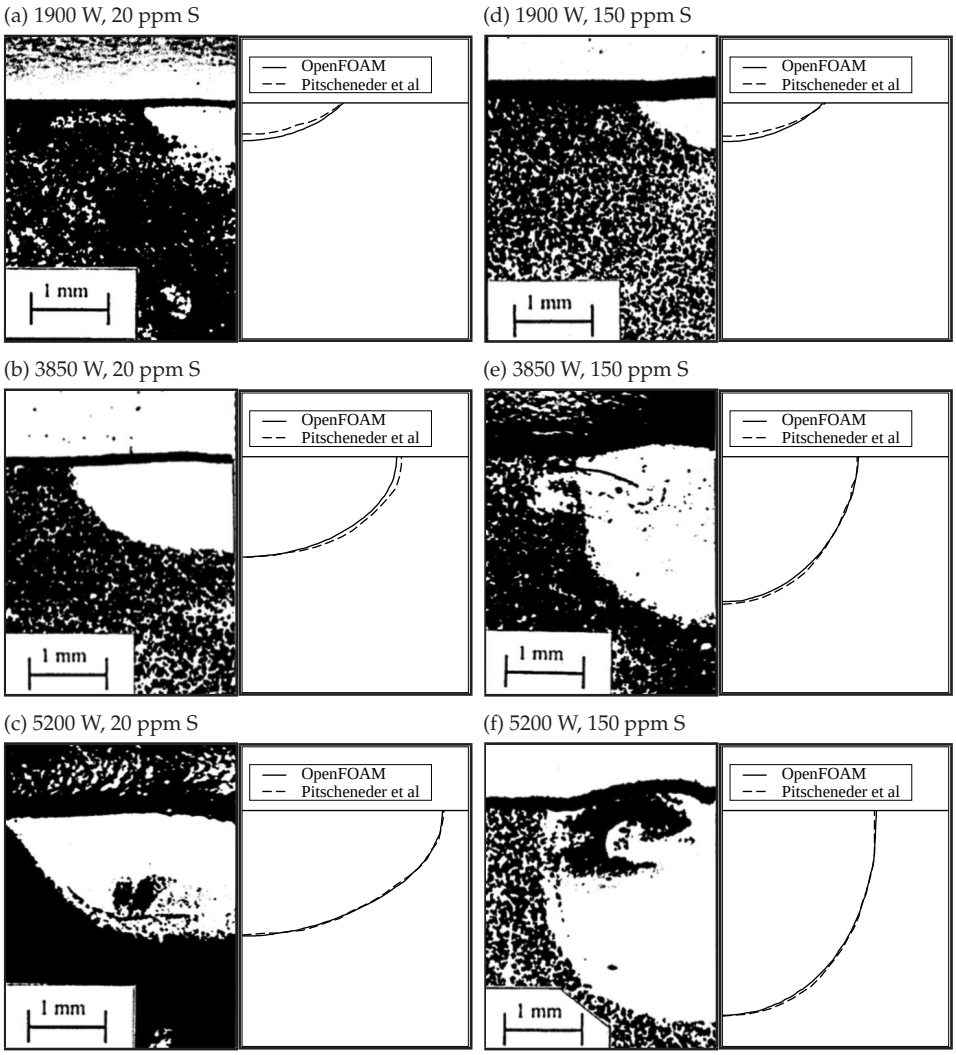

Figure 4.8. Weld pool shape comparisons between experiments (left) by Pitscheneder et al. (1996) and simulations (right), at t = 5 s for 20 ppm sulfur (a - 1900 W; b - 3850 W; c - 5200 W) and 150 ppm sulfur (d - 1900 W; e - 3850 W; f - 5200 W).

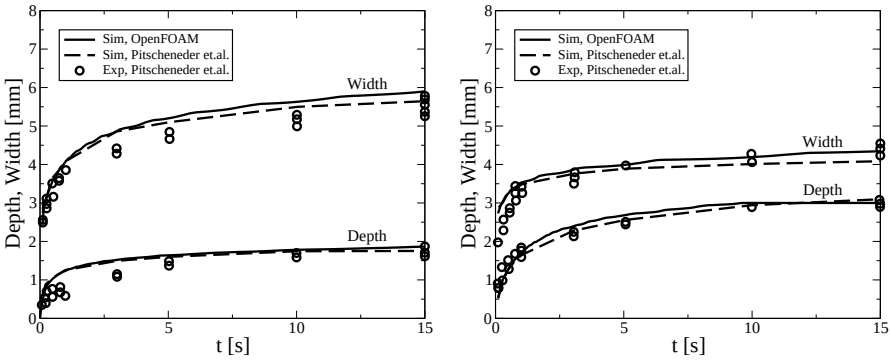

Figure 4.9. Time evolution of predicted and experimental weld pool depth and width for samples with 20 ppm S (left) and 150 ppm S (right). Laser power is 5200 W.

4.5 Influence of the enhancement factors

It has been shown that our simulation results agree well with results obtained by Pitscheneder et al. (1996) and with experimental data on post-solidification weld pool shapes. Nevertheless, it is important to keep in mind that in order to reach such a good agreement with experiments, Pitscheneder et al. (1996) increased the dynamic viscosity and the liquid thermal conductivity by a factor of 7.0 compared to their known molecular values, to so-called 'effective' values. Such an approach is a simple, yet very crude, way to account for the momentum and energy enhancement, which might be due to the transient and unstable nature of the flows as experimentally observed by *e.g.* Zhao et al. (2010). Although straightforward, this has no sound physical basis. Furthermore, there is no clear guideline on how much enhancement should be used for the viscosity and the thermal conductivity under certain operating conditions.

As a matter of fact, many published papers on weld pool simulations, regardless of types of heat source (laser or arc), showed results which were obtained using enhancement factors, f. Beside Pitscheneder et al. (1996), who used $f = 7$, the following papers explicitly mentioned the use of an enhancement factor f: Mundra and DebRoy (1993) used $f = 8$ in their simulation of laser weld pools of stainless steel incorporating element vaporization. Choo et al. (1992) employed $f = 30$ for their GTAW pools simulation. In a later paper the same authors, Choo and Szekely (1994), used $f = 100$ for the same GTAW pools simulation, and this led to weld pool shapes that agreed better with experiments compared to those from the previous paper.

An important thing one must note is that all the above papers exemplify the use of different f for different weld pool cases. The degree of complexity considered in each of the cases varies. This includes the heat source power, heating time, types of material, shape and size of workpiece, whether the heat source moves or is stationary, whether element vaporization is taken into account, *etc.*. This variation might relate to why such a large range of f is found in literature. However, the

idea of 'tuning' f originates from the same reason, *i.e.* to get a good agreement with experiments, in terms of post-solidification weld pool shapes.

Using inverse modeling De and DebRoy (2004) and De and DebRoy (2005) estimated f. They fitted simulation results to experimental data for a number of different welding conditions. They found that f varies from $\sim$ 3 - 10 for the thermal conductivity and from $\sim$ 10 - 40 for the viscosity, for the different cases studied.

In this thesis, simulations of the case reported by Pitscheneder et al. (1996) are further carried out without the enhancement factor f, *i.e.* both the dynamic viscosity and the liquid thermal conductivity are kept at their known molecular values (0.006 kg/(m.s) and 22.9 J/(m.s.K), respectively, table 4.1). Additionally, some other values of f (= 2, 4, 8, 16, 32, 64) are also used in order to study how this variation affects weld pool flows and shapes.

The cross sections showing time evolutions of temperature and flow fields for 4 cases of different combinations of laser power and sulfur concentration, *i.e.* 3850 W, 20 ppm; 3850 W, 150 ppm; 5200 W, 20 ppm; 5200 W, 150 ppm, with f = 1, 2, 4 and 16, are given in figures 4.10, 4.11, 4.12, and 4.13, respectively.

In figure 4.10, for 3850 W and 20 ppm of sulfur, we can see that for all values of f the weld pool gets wider and deeper in time. As f is increased, however, the maximum temperature and velocities decrease. The maximum temperature is lower for higher f because heat becomes more diffusive. Also, as a result, the temperature gradients for higher f decrease. This results in a lower maximum velocity. The decreasing maximum velocity with f is also caused by an increased viscosity. Furthermore, with increasing f the weld pool becomes less wide, yet deeper, because of lower surface velocities and higher thermal conductivities. The surface velocities are directed outwards for all values of f because of the negative $d\sigma/dT$.

For case 3850 W and 150 ppm S (figure 4.11), the weld pool also gets wider and deeper as time evolves. Moving from f = 1 to 16, we can also see that maximum velocities, maximum temperatures, and local surface temperature gradients decrease. Additionally, unlike the 3850 W - 20 ppm case, there are two counter-rotating flows for f = 1, 2, and 4: An outward flow in the center of the weld pool and an inward flow at the weld pool periphery. This is because the range of surface temperatures allows for negative and positive values of $d\sigma/dT$. At f = 16, due to a very high conductivity the maximum surface temperature is very low such that only positive $d\sigma/dT$ is present, and consequently the flow moves inward everywhere on the weld pool surface. As we move from f = 1 to 4, the zones occupied by the inward flows become larger. This results from the movement of the transitional surface temperature (around 2000 K, according to figure 4.2) towards the weld pool center as the heat becomes more diffusive. As time evolves, the inward flow becomes more dominant, causing deeper weld pools. At f = 16, on the other hand, the flow is always inward as time evolves. Moreover, compared to f = 4 the weld pool is more shallow, instead of becoming deeper. This is caused by a lower surface temperature gradient, hence, a lower velocity, such that heat is convectively transported inward more slowly than that with f = 4.

For the case with 5200 W and 20 ppm S (figure 4.12), the time evolution of temperature and flow fields show similar tendency as those of case 3850 W and 20 ppm S as f is increased, *i.e.* the weld pool becomes less wide and deeper, maximum temperature and maximum velocities decrease, and surface temperature gradients also decrease.

For case 5200 W and 150 ppm S (figure 4.13), increasing f results also in lower maximum velocities, maximum temperature, and surface temperature gradients. Similar to case 3850 W and 150 ppm, two counter rotating vortices coexist in the weld pools with f = 1, 2, and 4, with the outer inward vortices become larger in time, whereas only an inward flow exists for f = 16. However, unlike case 3850 W - 150 ppm where increasing f from 4 to 16 gives a more shallow weld pool, in the case with 5200 W - 150 ppm the weld pool does get a little deeper, despite the velocity drop. This is due to the use of higher laser power, which suggests that more energy is transported in the weld pool per unit time.

The time evolutions of the aspect ratio of the weld pools are given in figure 4.14, for varying enhancement factors. Unfortunately, the experimental aspect ratio was provided by Pitscheneder et al. (1996) only for a laser power of 5200 W. Comparisons of fusion zone shapes with experiments at t =5 s are given in figure 4.15. These two figures show that in fact f = 8 gives good agreement of weld pool shapes with experiments for case 150 ppm (both laser powers), which renders the use of f = 7 in Pitscheneder et al. (1996) reasonable. However, for 20 ppm cases, f = 4 gives a better agreement with experiments. This discrepancy of f could indicate that element concentration may also affect the momentum and heat transfer enhancements in weld pools.

For the 20 ppm cases, increasing f seems to lead to a monotonic decrease of weld pool width, accompanied by a virtually monotonic increase of weld pool depth, where the trend stops at f = 64, probably due to much lower maximum velocities as viscosity is strongly enhanced. On the other hand, for 150 ppm the weld pool with increasing f becomes deeper until f = 4 for 3850 W, and until f = 8 for 5200 W, and a further increase of f makes the weld pool more shallow. Such behavior can be explained as follows. For 150 ppm, at $f = 1$ the difference between maximum temperature at weld pool center and the critical temperature where $d\sigma/dT$ changes sign is the largest, thus the region occupied by outward flow in the weld pool center is also the largest. As f is increased, the maximum temperature decreases, and the outward flow region decreases in size and the inward flow at the edge starts to dominate, leading to deeper weld pools. At certain values of f (*i.e.* f = 4 and 8, for 3850 W and 5200 W, respectively), the inward flow becomes much more dominant than the outward flow, and a maximum depth is obtained. However, as viscosity is also increased, the maximum velocity decreases. Thus, despite causing fully inward flows, further increase of f does not make the weld pool any deeper. Instead, the weld pool becomes more shallow, since the convective heat transfer weakens instead of being enhanced.

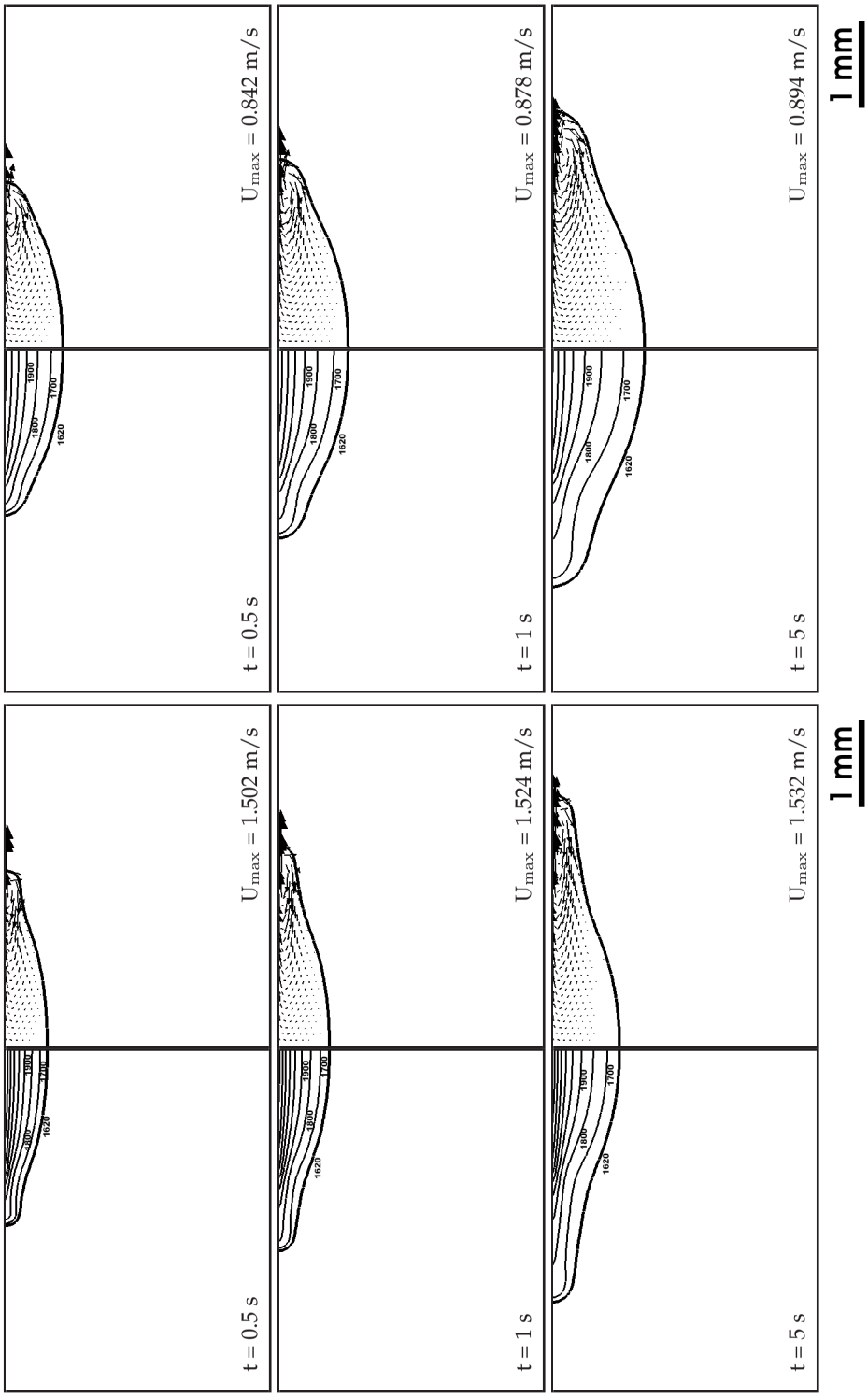

(a) 3850 W, 20 ppm, $f = 1$.

(b) 3850 W, 20 ppm, $f = 2$.

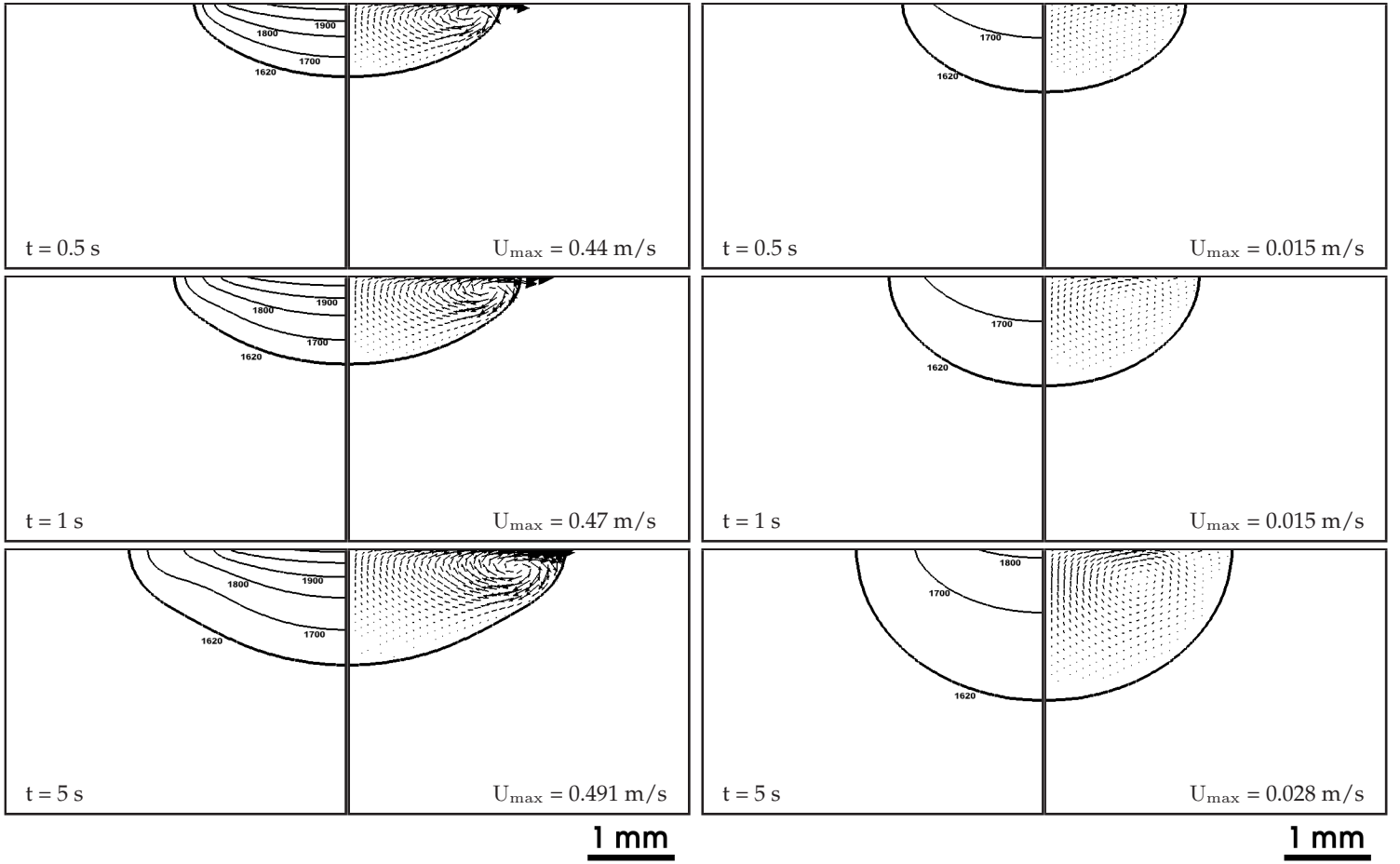

(c) 3850 W, 20 ppm, $f = 4$.

(d) 3850 W, 20 ppm, $f = 16$.

Figure 4.10. Time evolution of weld pool temperature (left) and velocity (right) fields for case 3850 W, 20 ppm S, $f = 1$, 2, 4, and 16. Note: velocity vector scales for different f are not the same.

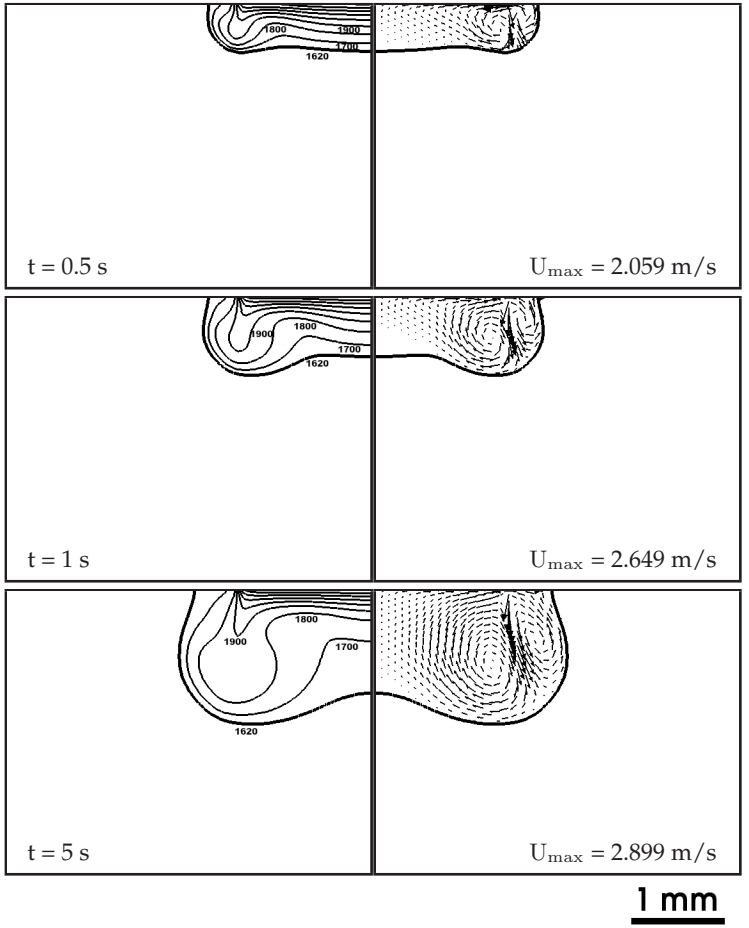

(a) 3850 W, 150 ppm, $f = 1$.

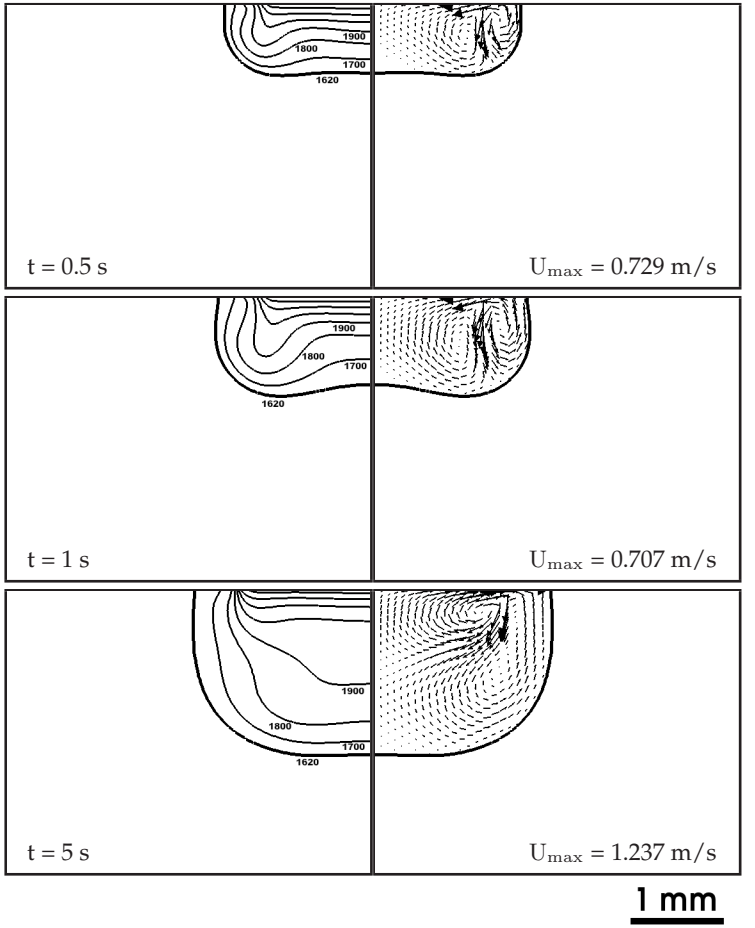

(b) 3850 W, 150 ppm, $f = 2$.

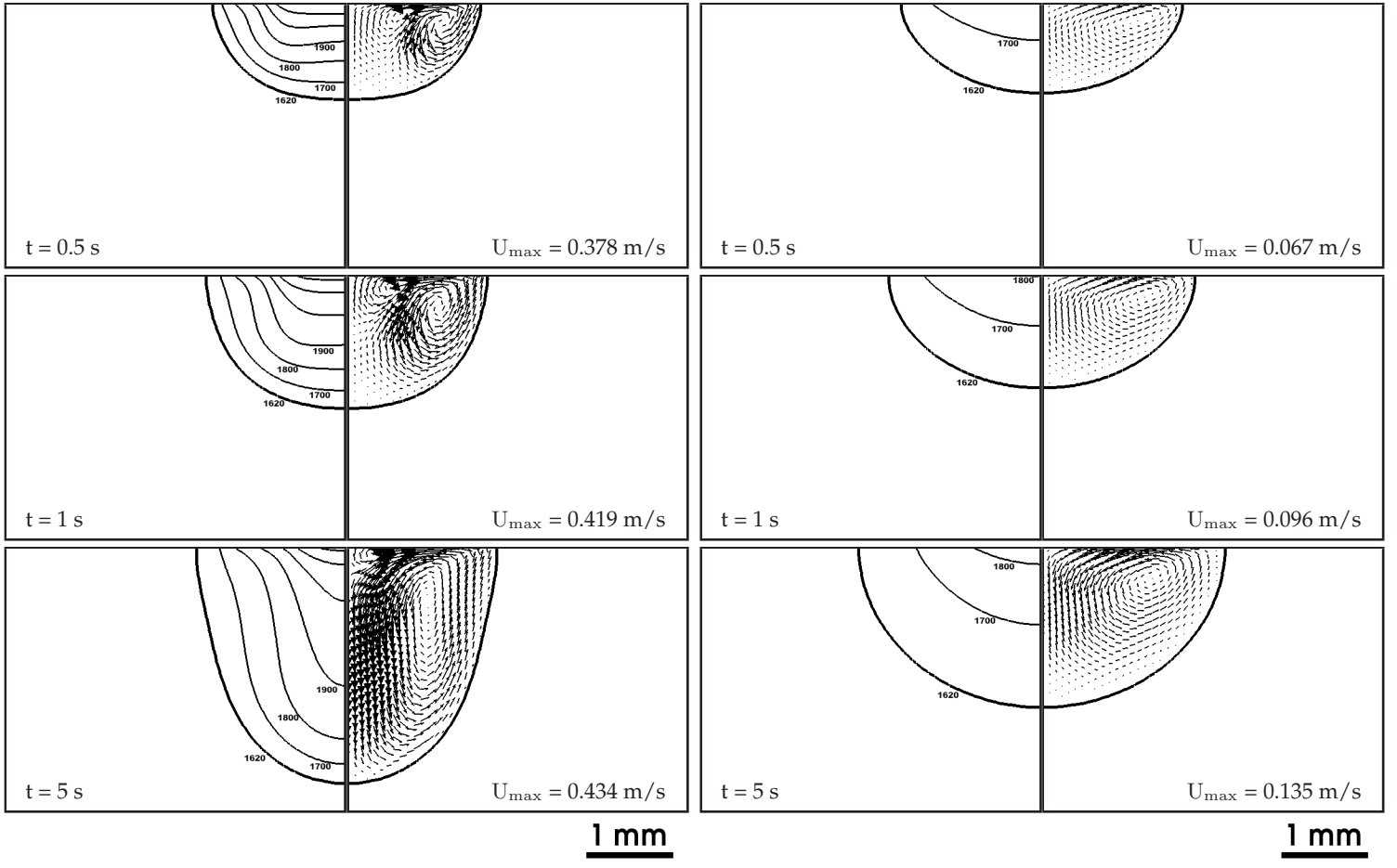

(c) 3850 W, 150 ppm, $f = 4$.

(d) 3850 W, 150 ppm, $f = 16$.

Figure 4.11. Time evolution of weld pool temperature (left) and velocity (right) fields for case 3850 W, 150 ppm S, $f = 1$, 2, 4, and 16. Note: velocity vector scales for different f are not the same.

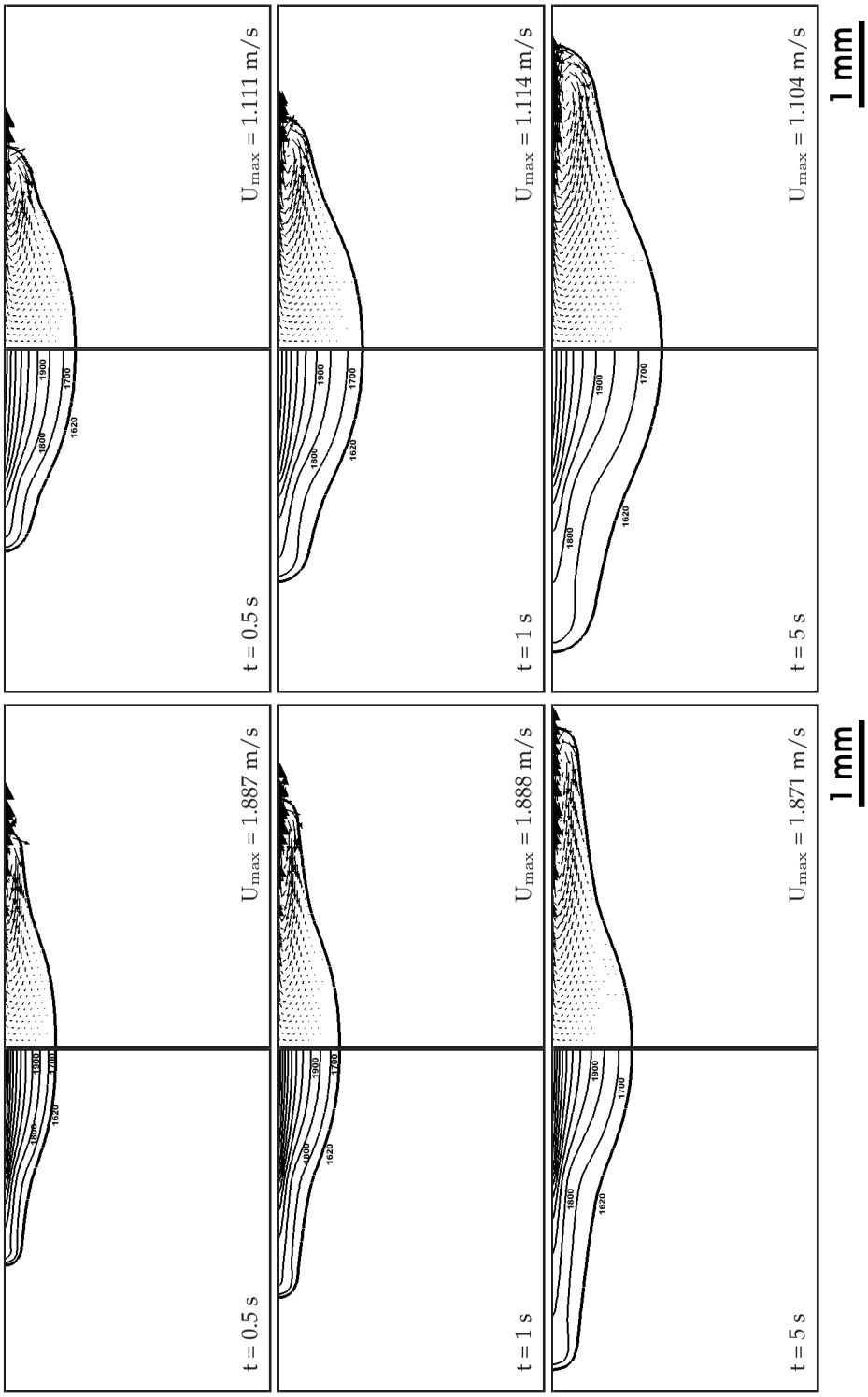

(a) 5200 W, 20 ppm, $f = 1$.

(b) 5200 W, 20 ppm, $f = 2$.

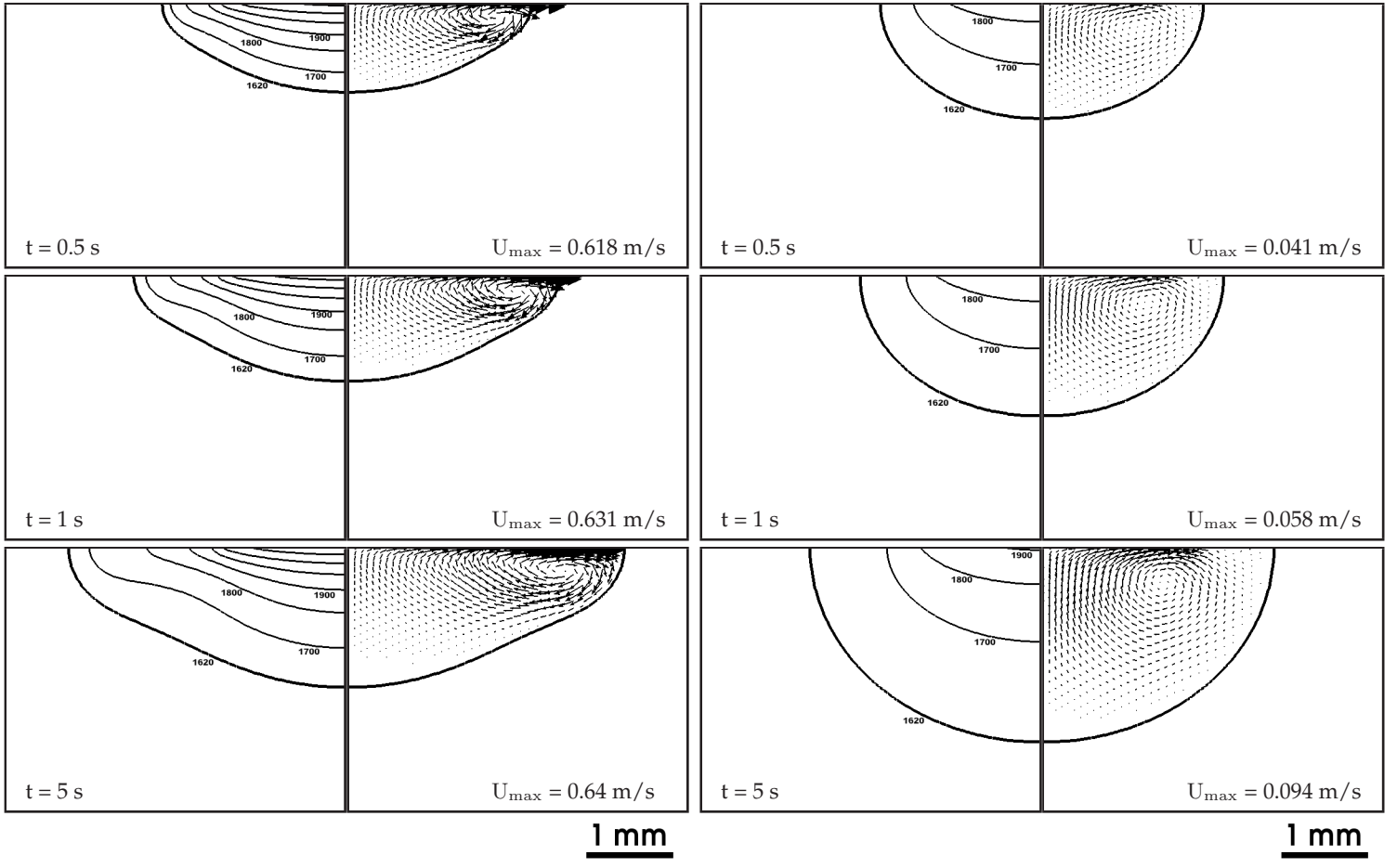

(c) 5200 W, 20 ppm, $f = 4$.

(d) 5200 W, 20 ppm, $f = 16$.

Figure 4.12. Time evolution of weld pool temperature (left) and velocity (right) fields for case 5200 W, 20 ppm S, $f = 1$, 2, 4, and 16. Note: velocity vector scales for different f are not the same.

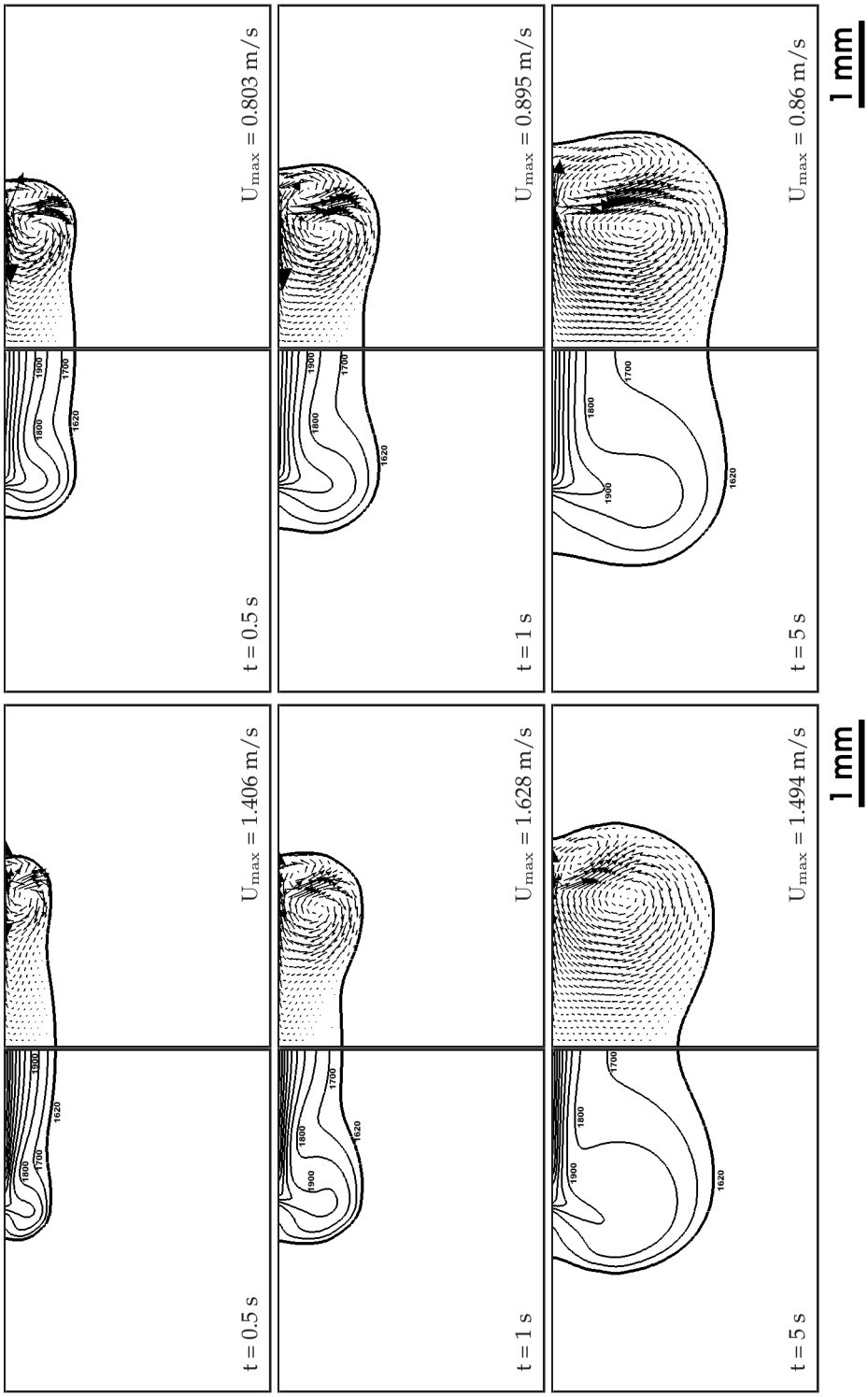

(a) 5200 W, 150 ppm, $f = 1$.

(b) 5200 W, 150 ppm, $f = 2$.

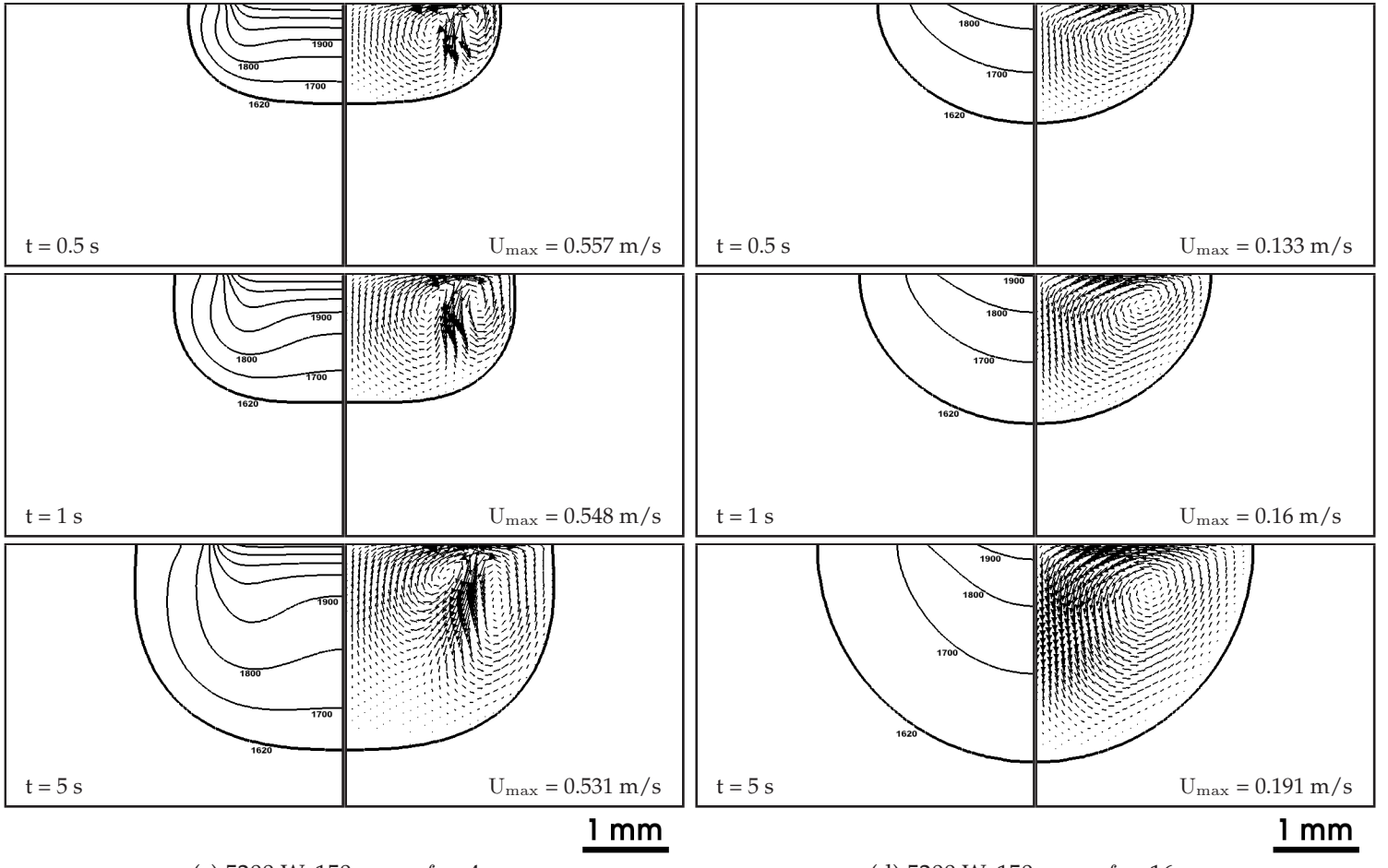

(c) 5200 W, 150 ppm, $f = 4$.

(d) 5200 W, 150 ppm, $f = 16$.

Figure 4.13. Time evolution of weld pool temperature (left) and velocity (right) fields for case 5200 W, 150 ppm S, $f = 1$, 2, 4, and 16. Note: velocity vector scales for different f are not the same.

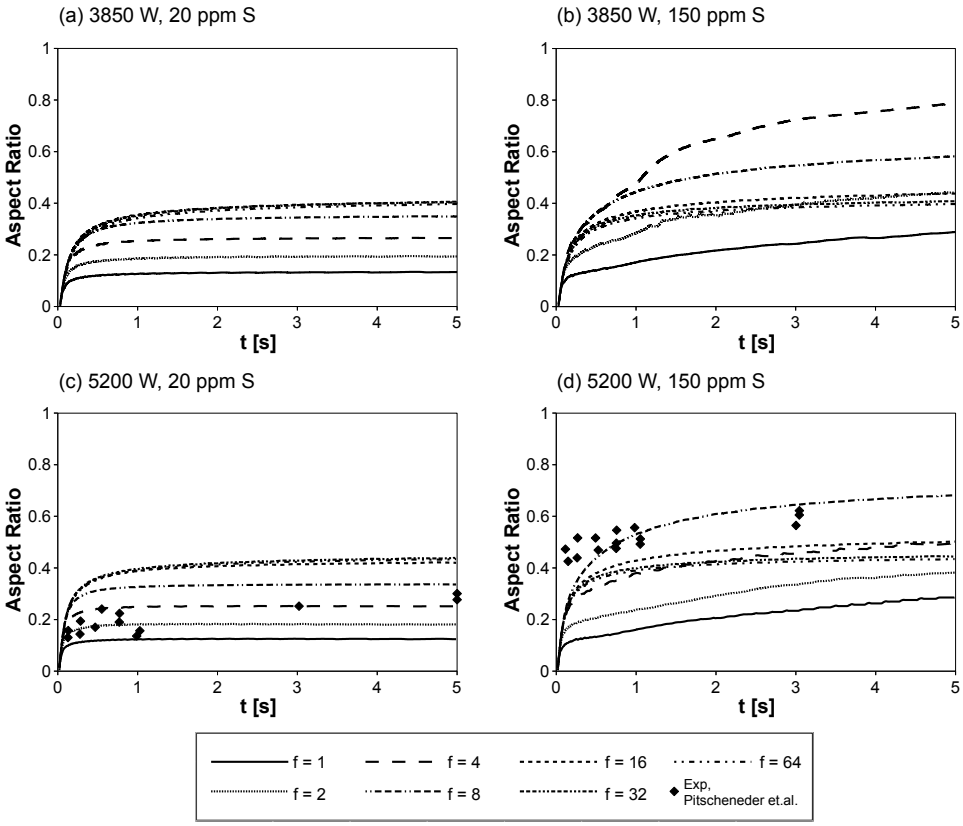

Figure 4.14. Comparisons of time evolution of weld pool aspect ratio for different enhancement factors, for (a) 3850 W, 20 ppm; (b) 5200 W, 20 ppm; (c) 3850 W, 150 ppm; (d) 5200 W, 150 ppm.

Figure 4.16 shows comparisons of temperature, temperature gradient, and radial velocity profiles along the weld pool surface, for varying enhancement factors, for 5200 W, 150 ppm S and t = 5 s. The critical temperature, T_C, at which the sign of $d\sigma/dT$ changes from positive (below T_C) to negative (above T_C), for 150 ppm S is 1965 K. For f = 1, 2, and 4, the temperature in the center of the weld pools (up to 65 -75% of the pool radius) is higher than T_C, and in the periphery it is lower than T_C. On the other hand, for f = 16, the temperature everywhere in the weld pool is lower than T_C. The temperature gradients are always negative for all cases, simply because of the monotonic decrease of temperature from the center to the edge. However, the magnitude of the temperature gradients vary, with the f = 1 case giving the largest peak at 75% of the pool radius and f = 16 with the smallest peak at 55% of pool radius. The flow direction is determined by the sign of the surface tension gradient, which is product of temperature gradient of surface tension and temperature gradient, *i.e.*:

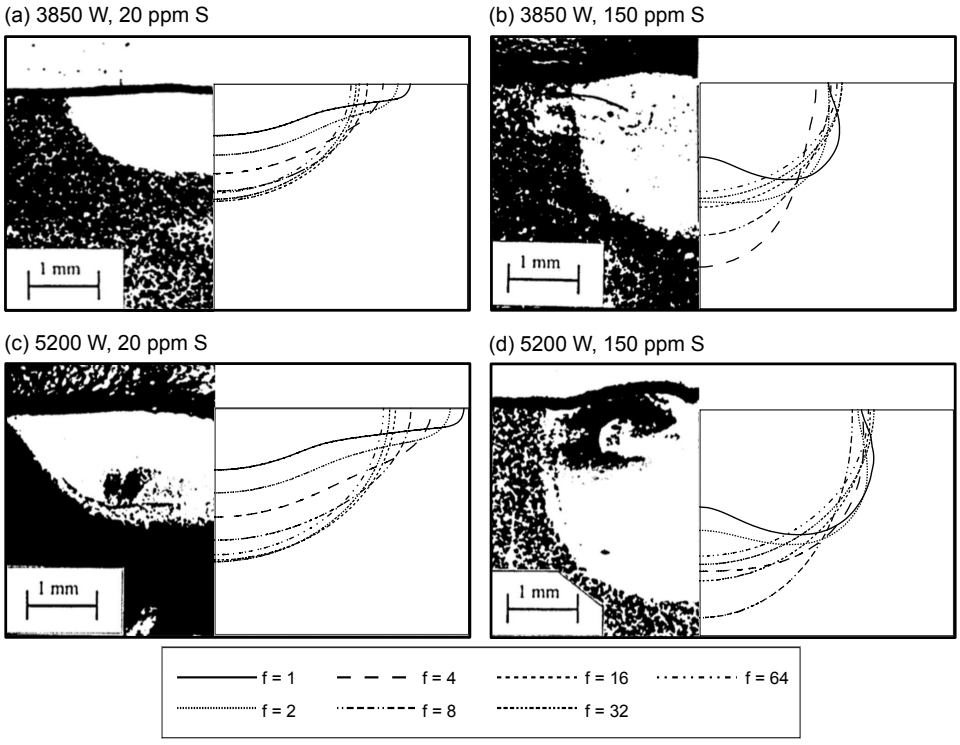

Figure 4.15. Comparisons of weld pool fusion zone shapes at t = 5 s between experiment (left) and simulations with varying enhancement factors f (right), for (a) 3850 W, 20 ppm; (b) 3850 W, 150 ppm; (c) 5200 W, 20 ppm; (d) 5200 W, 150 ppm.

$$\frac{d\sigma}{dx} = \frac{d\sigma}{dT}\frac{dT}{dx} \tag{4.5}$$

A positive value of $d\sigma/dx$ implies that surface tension in the center is lower than that at the edge, giving an outward flow along the weld pool surface, and *vice versa* for a negative $d\sigma/dx$. Accordingly, for f = 1, 2, and 4, the flow in the center moves outward (positive velocity) and in the periphery moves inward (negative velocity), whereas for f = 16 the flow moves inward everywhere in the weld pool.

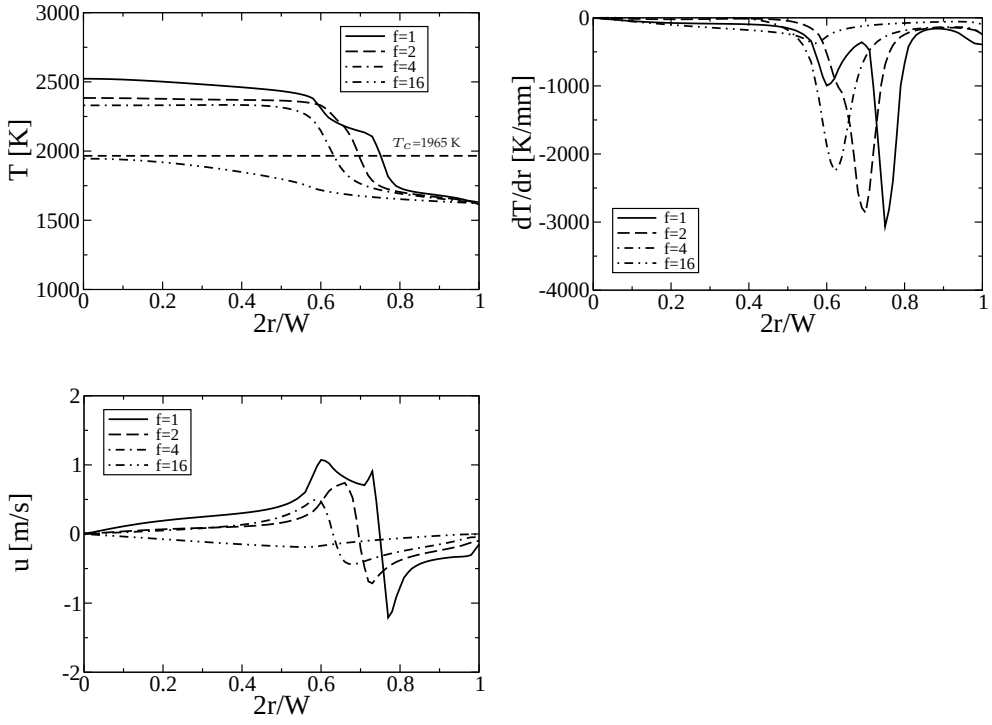

Figure 4.16. Comparisons of radial profiles along the weld pool surface of: (a) Temperature; (b) Temperature gradient; (c) Radial velocity, for f = 1, 2, 4, and 16. Laser power = 5200 W, sulfur concentration = 150 ppm and t = 5 s. Note: dimensionless radius ($2r/W$) from 0 (weld pool center) to 1 (weld pool edge) is used for the x-axis.

4.6 Effects of post-laser-switch-off on weld pool shapes

In the previous section, effects of enhancement factors on weld pool flows and weld pool shapes have been discussed. As was done in Pitscheneder's paper, experimental post-solidification weld pool shapes were compared to simulated weld pool shapes at the moment of laser switch-off. The latter was defined by the melting temperature isotherm at the moment of switch-off. The experimental post-solidification weld pool shape, however, is determined by all the material that has reached a temperature above the melting temperature, at any time instant. This is illustrated in figure 4.17.

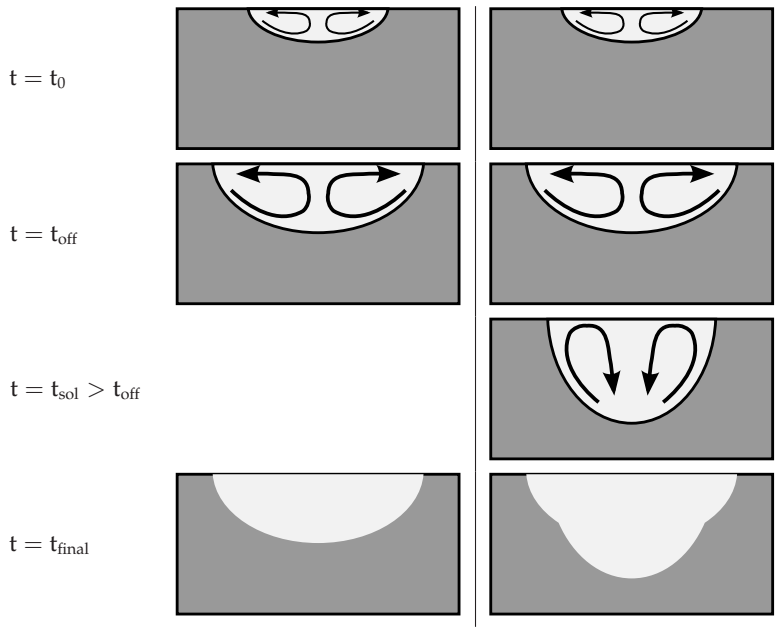

Figure 4.17. Illustration of difference in methods to identify fusion zone shapes: Commonly used method, without solidification (left); and method in this thesis, with solidification (right).

In the first method (left column), suppose the weld pool evolves during laser heating period from t_0 to t_{off}, *i.e.* its size increases as the melt front propagates. During this period, the melt front (solid line) coincides with the fusion boundary. The same also applies in the second method (right column). Subsequently, if the laser is deactivated at t_{off}, then for $t > t_{off}$ cooling takes place. This is considered in the second method, but not in the first one. During cooling, the melt front close to the surface propagates inward, as opposed to outward during heating. However, under certain conditions the flow direction might be altered too, such that the melt front deep in the pool moves even further downward, instead of upward. Finally, at t_{final} the weld is fully solidified and the final fusion zone is obtained. As shown in the bottom row of figure 4.17, the fusion zone from the second method

could be different than that from the first, which is simply equal to that obtained at t_{off}. Using the second method, we can have a more proper comparison with experimental weld shapes, since it also takes into account the solidification stage.

In our simulations, the laser is switched off at t = 5 s, and radiative and convective heat losses are imposed at the weld pool surface. The simulations are carried out for f = 1 and 2, with a radiative emissivity of 0.5 and a convective heat loss coefficient of 10 W/(m^{2}K).

Figures 4.18 - 4.21 show the weld pool cross section evolution from the time the laser is switched off (t = 5 s) to the time the weld pool is completely solidified, for 4 cases with combinations of laser power (3850 and 5200 W) and sulfur concentration (20 and 150 ppm). The area colored in grey is the non-melting solid zone, whereas the white area is the fusion zone. The black line is the melting temperature isotherm.

In all cases discussed, switching off the laser causes the melting isotherms close to the surface to move towards the center and eventually vanish during the cooling process. For the 20 ppm cases (figure 4.18 and 4.20), the flows stay in the outward direction and only decrease in intensity. Accordingly, the final solidified weld shapes are similar to the weld pool at t = 5 s. In contrast, for 150 ppm cases (figure 4.19 and 4.21), the flows change directions: the center vortice changes from outward to inward, whereas the peripheral vortice changes from inward to outward and is submerged beneath the surface. The flows initially increase their intensity downward at t = 5.01 and 5.02 s, before fading away as surface temperature gradients, hence, surface tension gradients decrease and the weld pool solidifies further. This increased downward velocities lead to deepening of the weld pool, resulting in a fusion zone that is deeper than that at t = 5 s.

The flow reversals that occur for 150 ppm also lead to a somewhat prolonged heat transfer towards the bottom of the weld pool, indicated by the downward movement of some isotherms. This causes longer solidification time for 150 ppm cases compared to 20 ppm cases, where the isotherms move upward throughout this cooling stage. In addition, solidification for 5200 W cases, as expected, is also longer than 3850 W.

That the flow direction during cooling remains the same for 20 ppm, but changes for 150 ppm can be explained by revisiting figure 4.2. For 20 ppm, $d\sigma/dT$ is mainly negative. Thus decreasing temperature in the weld pool will not change the outward flow direction. Slightly above the melting temperature, at around 1700 K, $d\sigma/dT$ indeed becomes positive, but by the time the weld pool is cooled down to around 1700 K, the temperature gradient is already so small that a change of flow direction hardly takes place. For 150 ppm, on the contrary, $d\sigma/dT$ changes sign from negative (outward flow) to positive (inward flow) at 1965 K, which is still considerably higher than melting temperature. This results in a flip of Marangoni stress direction.

Having done the solidification simulations, we can compare the post-solidification weld pool shapes to those obtained in the previous simulations where solidification is excluded, and also to experimental shapes. This comparison is given in

figure 4.22, in which simulation results with f = 1 and 2 are shown. The post-solidification shapes for 20 ppm cases with f = 1 and 2 are identical to those obtained when no solidification is taken into account. In other words, for 20 ppm the depth does not increase during the solidification phase, and an increased depth is only obtained due to higher thermal conductivity and viscosity by increasing f. On the other hand, for 150 ppm the post-solidification weld pools are significantly deeper than the weld pools at t = 5 s. For both sulfur concentrations with power 3850 W and f = 2, the final shapes are almost similar to the experimental shapes. For 150 ppm and 5200 W, however, the post-solidification weld pool predicted with f = 2 still underpredicts the depth of the experimental weld pools by 30-35%.

In general, with laser power 3850 W, the fusion zone shapes with f = 2 seem to be in a good agreement with experiment, regardless of sulfur concentrations, provided that solidification is taken into account. On the contrary, at higher laser power (5200 W), weld pool depth with f = 2 is very close to experimental result for concentration of 20 ppm, but not for 150 ppm. This noticeable discrepancy for 5200 W -150 ppm case could perhaps be explained by free surface effects. Experimental result (figure 4.22 (d)) shows a significant surface deformation, which is much stronger than for the other cases. Such a strong deformation might have involved severe flow instabilities, resulting in a deeper weld. These free surface effects will be discussed further in chapter 5.

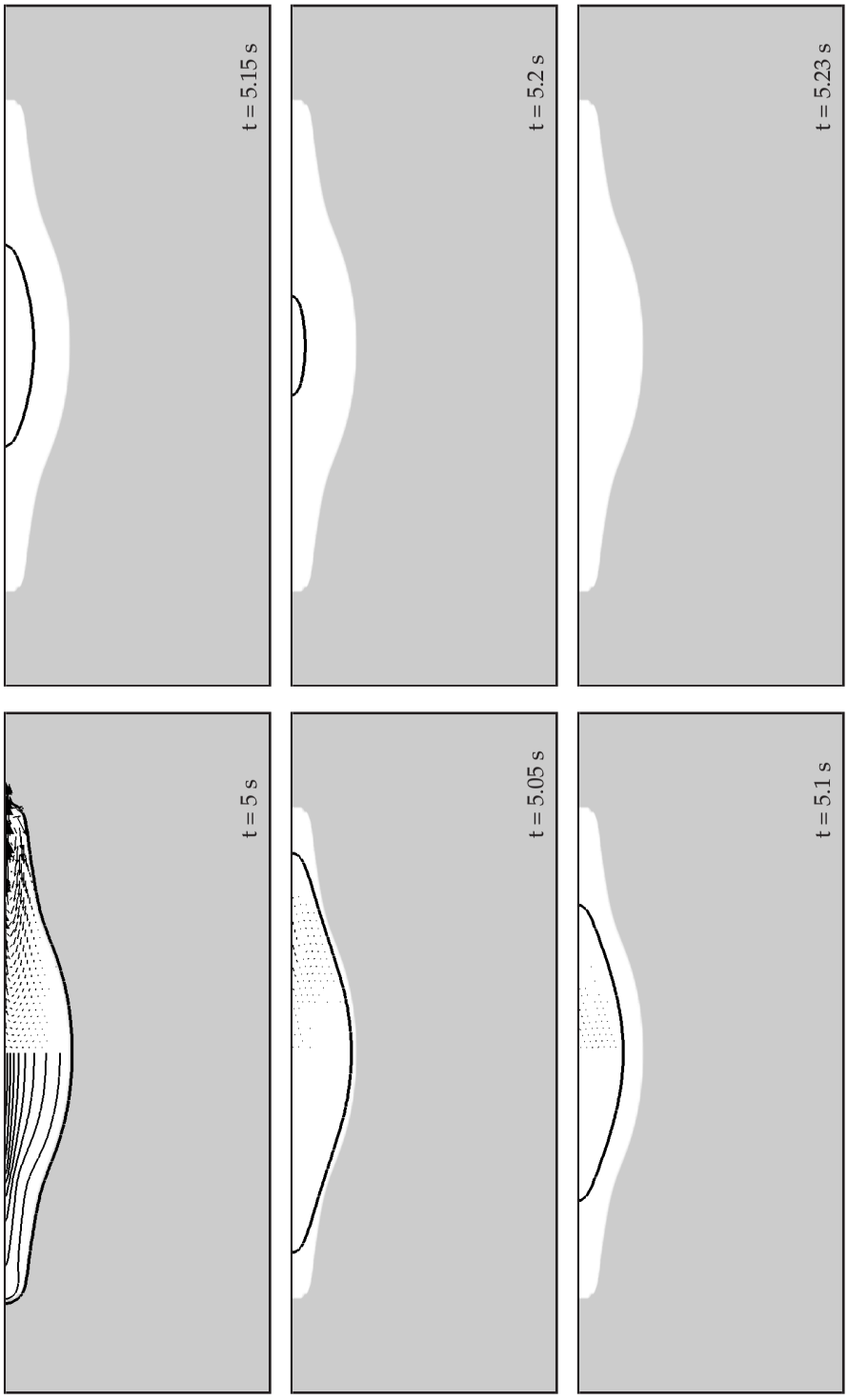

Figure 4.18. Temperature (left) and velocity (right) fields during cooling of the weld pool upon laser switch-off, for 3850 W, 20 ppm S.

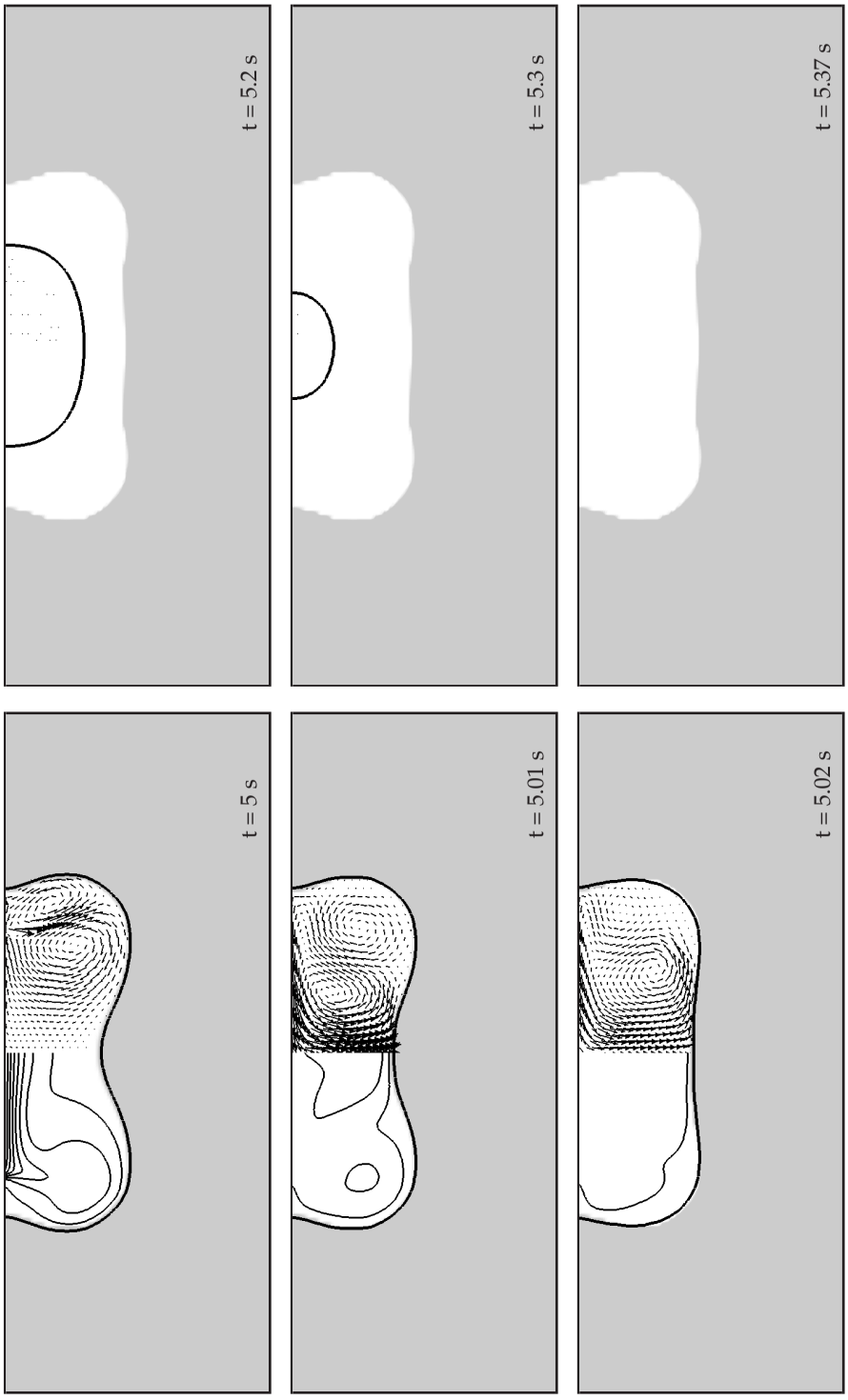

Figure 4.19. Temperature (left) and velocity (right) fields during cooling of the weld pool upon laser switch-off, for 3850 W, 150 ppm S.

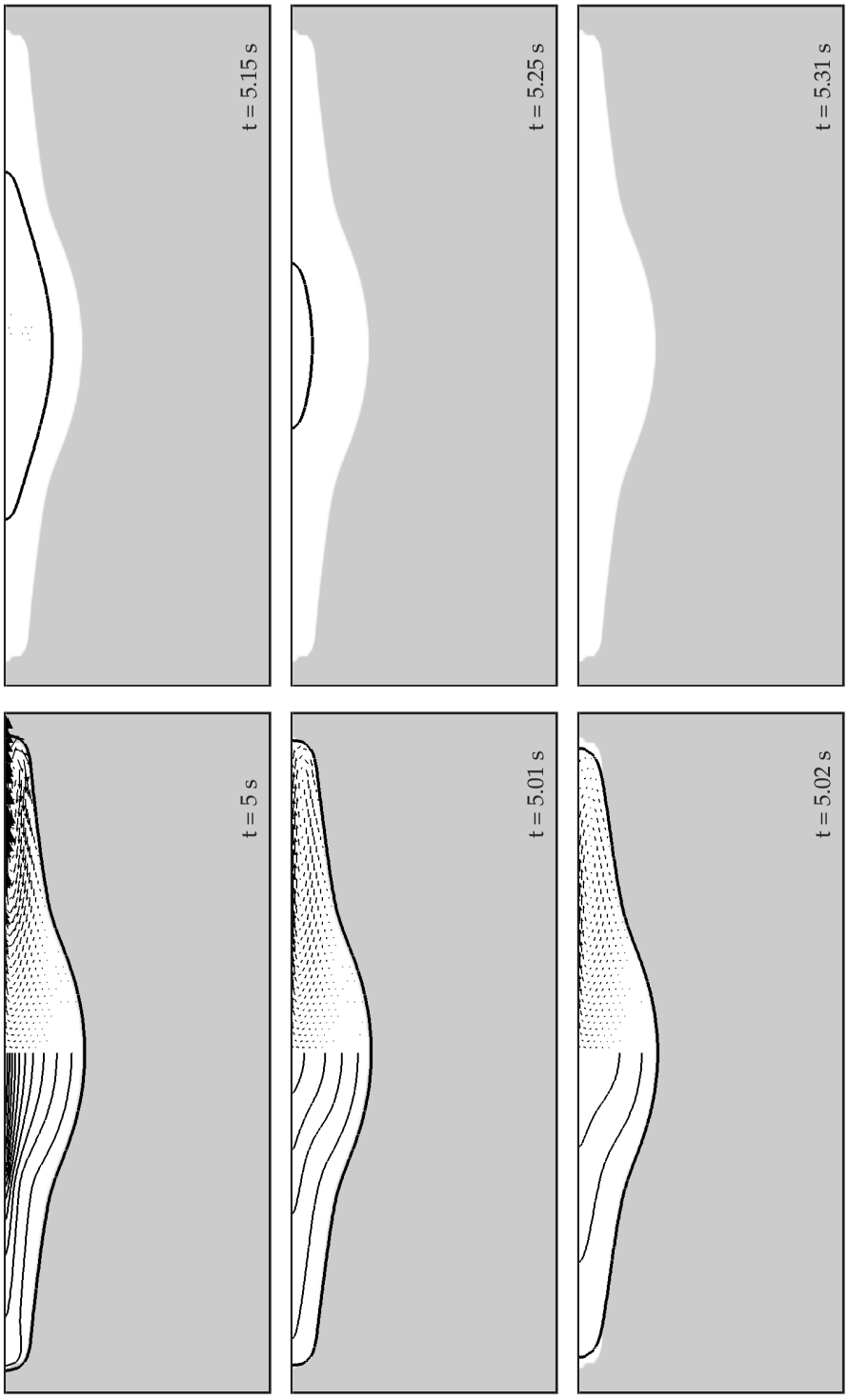

Figure 4.20. Temperature (left) and velocity (right) fields during cooling of the weld pool upon laser switch-off, for 5200 W, 20 ppm S.

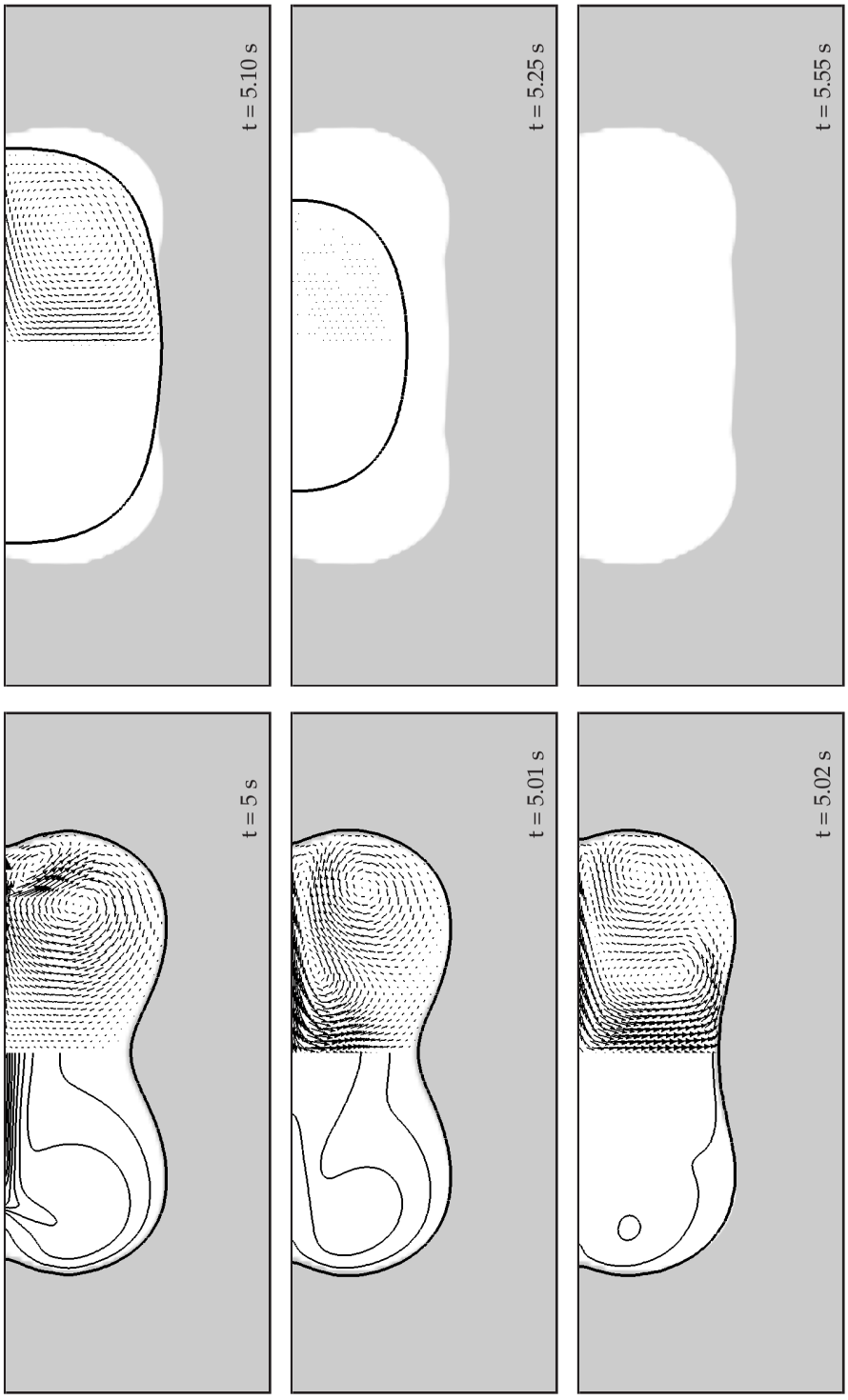

Figure 4.21. Temperature (left) and velocity (right) fields during cooling of the weld pool upon laser switch-off, for 5200 W, 150 ppm S.

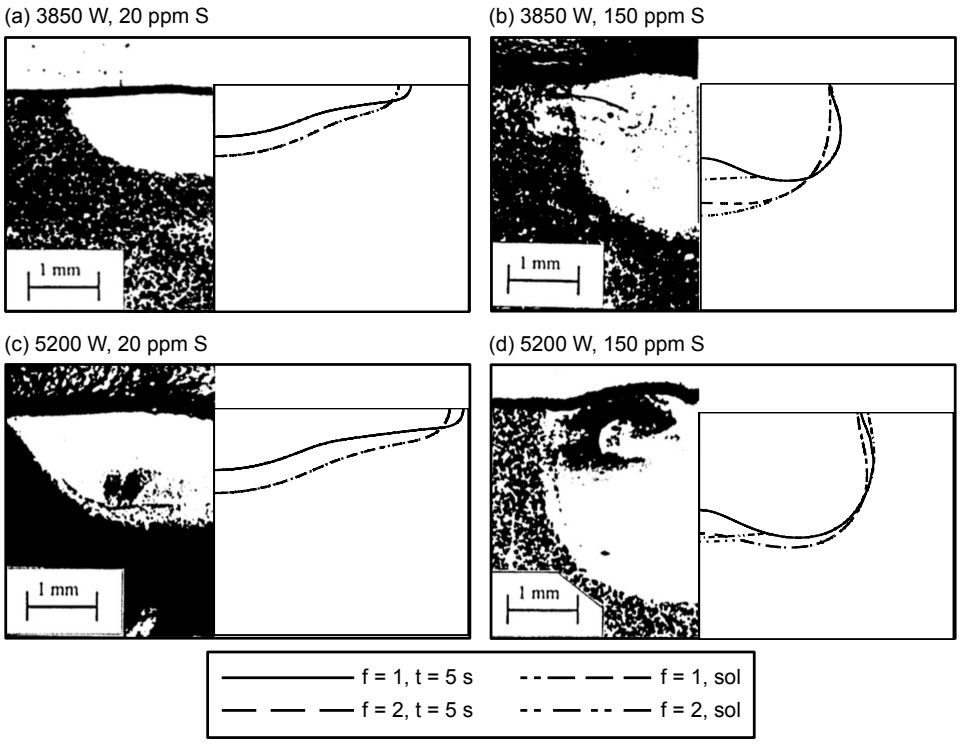

Figure 4.22. Comparisons of weld pool fusion zone shapes at t = 5 s between experiment (left) and simulations (right) with $f = 1$ and $f = 2$, without solidification and with solidification, for (a) 3850 W, 20 ppm; (b) 3850 W, 150 ppm; (c) 5200 W, 20 ppm; (d) 5200 W, 150 ppm.

4.7 Concluding remarks

In this chapter, we have studied the simulation of weld pool hydrodynamics in conduction mode laser spot welding, assuming the weld pool to have a flat, non-deformable upper liquid surface. Our special focus was on an evaluation of the so-called enhancement factor method, *i.e.* the artificial increase of the molecular viscosity and the thermal conductivity of the liquid metal in order to account for enhanced heat and mass transfer due to flow instabilities, which has been widely used in literature to obtain good agreement between experimental post-solidification weld pool shapes, and simulation results.

We based our study on well-documented experimental and simulation data reported by Pitscheneder et al. (1996). These authors present results for conduction mode laser spot welding of steel with various concentrations of sulphur, using varying laser powers. The sulphur concentration strongly influences the variation of surface tension with temperature, which is mainly negative for low sulphur concentrations and mainly positive for high concentrations.

In their simulations, Pitscheneder et al. (1996) artificially increase both the viscosity and the thermal conductivity of the liquid steel by an enhancement factor $f = 7$. Using this same enhancement factor $f = 7$, our OpenFOAM simulations of the fusion zone shape were found to be in good agreement with both the simulation results and experimental data reported by Pitscheneder et al. (1996). It was concluded however, that this enhancement factor has no sound physical basis and therefore its appropriate value cannot be set *a priori*.

A systematic study of the influence of the value of the enhancement factor f showed that the use of $f > 1$ may lead to different modifications in the fusion zone shape, depending on the welding conditions. This is due to two counteracting effects:

- On the one hand, increased thermal conductivity leads to reduced thermal gradients, and therefore reduced Marangoni forces and lower velocities in the weld pool, which are further reduced by the increased viscosity. This reduces convective mixing in the weld pool. For inward flowing weld pools, this reduces the weld pool depth and increases the weld pool width. For outward flowing weld pools, it increases weld pool depth and reduces the weld pool width.
- On the other hand, the increased thermal conductivity leads to enhanced conductive heat transfer, increasing particularly the depth of the weld pool. For very large values of f, the weld pool flow is almost completely suppressed and most heat transfer is conductive.

For the welding conditions presented by Pitscheneder et al. (1996), we found the best agreement with post-solidification experimental data when using $f = 4$ for a laser power of 3850 W, and $f = 8$ for a laser power of 5200 W. Both values are in line with the use of $f = 7$ by Pitscheneder. The larger optimal value of f for 5200 W may be explained by the increased flow instabilities at this high heat input.

The physical reason for the need to use enhancement factors, as commonly reported in literature, is that flow instabilities, which are not accounted for in 2-D, steady-state, axisymmetric, flat-surface simulations, lead to enhanced heat and momentum transfer in the weld pool. This explanation will be further studied in chapter 5. However, in the present chapter we studied a second possible reason why simulations with $f = 1$ do not agree with experimental data: the neglect of further changes in the fusion zone shape during the solidification phase after the switch-off of the heat source. Whereas in most literature, post-solidification fusion zone shapes have been compared to simulated fusion zone shapes at the end of the heating period, our present simulations have shown that in fact the fusion zone shape may significantly change after the heat source has been switched off. This is particularly the case for welding conditions with a positive $d\sigma/dr$ along the weld pool surface (*i.e.* negative $d\sigma/dT$, as is the case for high concentrations of surface active elements, and high weld pool temperatures), resulting in a radially outward Marangoni flow along the surface. During the cool down phase, the sign of $d\sigma/dT$ may change from negative to positive, resulting in the Marangoni flow direction to change from outward to inward. As a consequence, a significant deepening of the weld pool occurs during the cool down phase. The post-solidification fusion zone may therefore be up to 30% deeper than the weld pool at the end of the heating stage.

Taking into account the deepening of the fusion zone after the heating has been switched off, partly accounts for the fact that experimental post-solidification weld pools are generally deeper than those predicted by simulations. Therefore, when taking this into account, lower enhancement factors f can be used to get good agreement between simulations and experiments. However, even when accounting for post-heating effects, 2-D, steady state, axisymmetric, flat surface simulations of weld pool hydrodynamics do not lead to good agreement with experimental fusion shapes without the use of an enhancement factor $f > 1$. Therefore, in the next chapter, we will study whether this is due to flow instabilities that cannot be captured in 2-D, steady state, axisymmetric, flat surface simulations.

5 CHAPTER

Simulations of laser spot weld pool flows with free surface deformations

5.1 Introduction

In this chapter we study the influence of using a free surface model (section 2.4) instead of a flat surface model (section 2.3) on weld pool simulations. As discussed in chapter 4, this is driven by our objective to compare results of flat and free surface simulations and to study any effects that weld pool free surface deformation have on weld pool hydrodynamics and final weld shapes. As test cases, we again study the conduction mode laser spot welding cases as reported by Pitscheneder et al. (1996)

5.2 Simulation settings

In all simulations presented in this chapter, we use an enhancement factor f = 1 for viscosity and thermal conductivity.

5.2.1 Mesh generation

The simulations employed a 2-D axisymmetric coordinate system with the same mesh resolution used for the flat surface simulation ($n_r \times n_z = 110 \times 160$ in 15 mm $\times$ 15 mm material domain). An additional mesh of $n_r \times n_z = 110 \times 70$ to account for a 15 mm $\times$ 3.5 mm gas region above the weld pool, is used. Thus, in total the mesh resolution is $n_r \times n_z = 110 \times 230$, covering a computational domain of 15 mm $\times$ 18.5 mm. The cell size in the r-direction varies from 0.035 mm close to the symmetry axis to 3 mm at the outer edge of the computational domain. In the z-direction, cell thickness varies from 0.02 mm near the free surface to 1 mm at the bottom and 0.1 mm at the top boundary. A comparison between the meshes used for the flat and free surface simulations is given in figure 5.1.

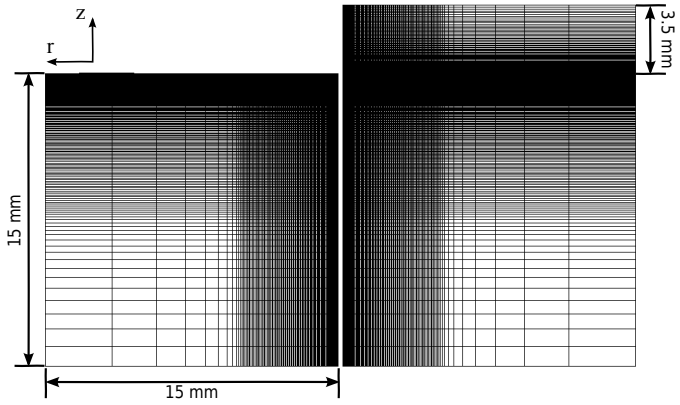

Figure 5.1. 2-D axisymmetric meshes for flat surface (left) and free surface (right) simulations. Note: the flat surface mesh is mirrored horizontally for convenient side-by-side comparison.

5.2.2 Boundary conditions

The boundaries of the computational domain are depicted in figure 5.2. The top boundary is assumed to be always in the gas phase, *i.e.* surface deformations do not reach this boundary. The gas side boundary is also in gas phase. At these boundaries, air can flow freely in and out, and a constant atmospheric pressure is imposed. In order to allow for heat to leave the domain, a radiative boundary condition is imposed at the top boundary (see figure 2.5), with a radiative emissivity ϵ_r = 0.5. At the gas side boundary, an adiabatic temperature is applied.

The side solid and bottom boundaries are always in solid phase, *i.e.* melt fronts do not touch these boundaries, and zero velocities are imposed. Furthermore, a zero pressure gradient and adiabatic temperature boundary conditions are employed at these boundaries.

At the axisymmetry boundary, the symmetry boundary conditions (Eq. 4.2) are used.

5.2.3 Numerical schemes

The transport equations for the free surface model are solved by employing a higher-order NVD scheme with Minmod flux limiters. In particular, the VOF equation is discretized using the Gamma scheme combined with a MULES (Multidimensional Universal Limiter with Explicit Solution) solver. The time derivative terms are treated using a first-order fully implicit time integration scheme. The time step is controlled by a maximum Courant number $Co < 0.1$, associated with a typical time step of 5×10^{-6} s. Convergence is satisfied if the pressure residual is lower than 10^{-8}, and the residuals of volume fraction, velocity, and temperature are lower than 10^{-12}.

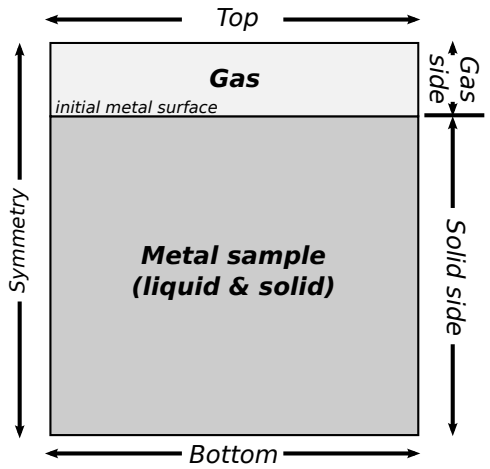

Figure 5.2. Boundaries used for free surface simulation.

5.3 Comparison with flat surface simulation results

5.3.1 Heating stage

The simulations were performed for a laser power of 3850 W and steel samples with sulfur concentrations of 20 and 150 ppm. Comparison of flow and temperature fields between flat and free surface simulations are given in figure 5.3 and 5.4, for 20 ppm and 150 ppm sulfur concentrations, respectively. Snapshots during laser heating at t = 1 and 5 s are shown, whereas during solidification snapshots at t = 5.02, 5.05, and 5.1 s are given.

For 20 ppm sulfur (figure 5.3), the weld pools with flat and free surface show a general similarity in flow direction, *i.e.* the flow is outward, as well as in temperature fields during laser heating. However, the radial surface velocities for the flat surface case is somewhat higher than for the free surface case, leading to a slightly wider weld pool.

On the other hand, the weld pool with free surface shows a strong surface deformation, where it is depressed in the center and elevated at the edge, as a result from the outward flow. Such mechanism for outward flow is consistent with what is reported in Mazumder (1991). The center depression also pushes the melt front lower than that of the flat surface simulation, leading to a deeper weld pool.

Also for 150 ppm (figure 5.4), the flat and free surface simulation show a general similarity in flow and temperature fields. Two counter-rotating flows are formed: outward flow in the center and inward at the edge. Nevertheless, some differences can also be identified. Firstly, there is more heating at the edge of the free surface weld pool, as indicated by a cluster of isotherms at the edge at t = 1 s. Secondly, a steeper temperature gradient at the edge in the flat surface case results in a positive $d\sigma/dT$ in this region, leading to inward flow. For the free surface case, the inward flow at the edge is weaker at t = 1 s, due to a higher temperature and

therefore less positive $d\sigma/dT$. However, as the inward flow is developed, heat at the edge is also convectively transported to the center, thus lowering the edge temperature and strengthening the inward flow further, as shown at t = 5 s.

Since the inward flow is stronger for the flat surface case, the weld pool in this case also gets deeper than that of the free surface case. Additionally, a surface elevation is observed in the free surface case, which results from an initially inward flow when weld pool temperature is still low such that $d\sigma/dT$ is positive. This also causes the melt front at the center to be not as deep as that of the flat case.

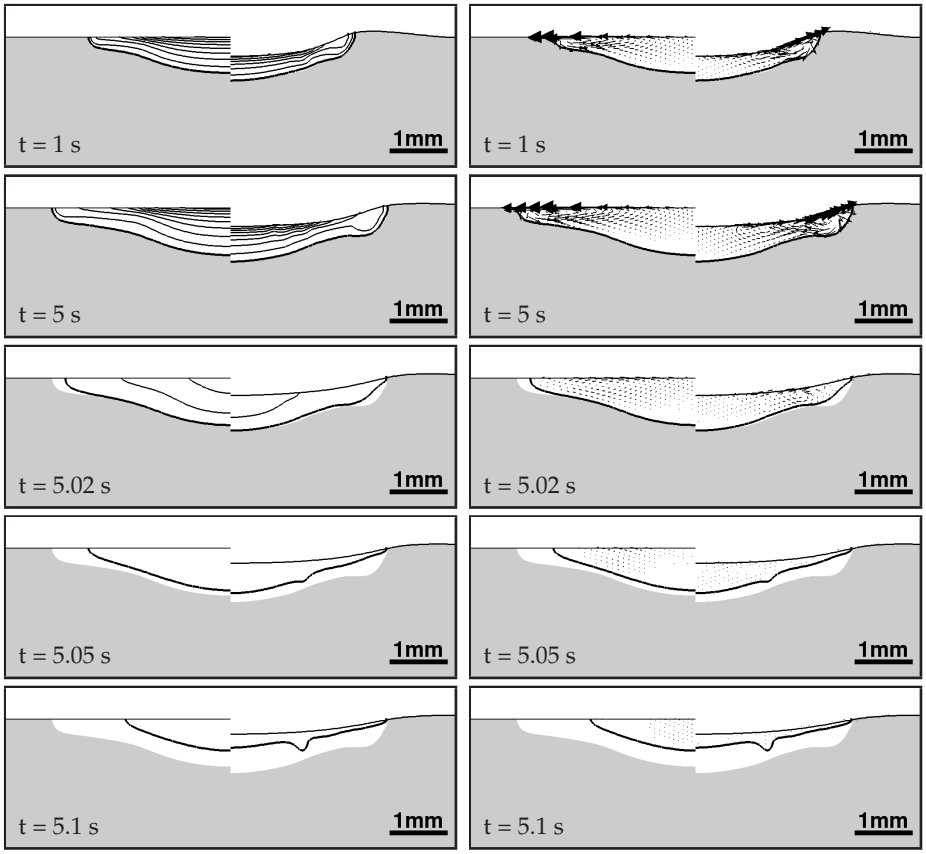

Figure 5.3. Comparison of weld pool temperature (left) and velocity (right) fields for 3850 W, 20 ppm S, between flat (left) and free (right) surface simulations, f = 1. The isotherms start from 1620 K (the melting temperature) at the weld pool boundary, then continue from 1700 K onwards, with an increment of 100 K.

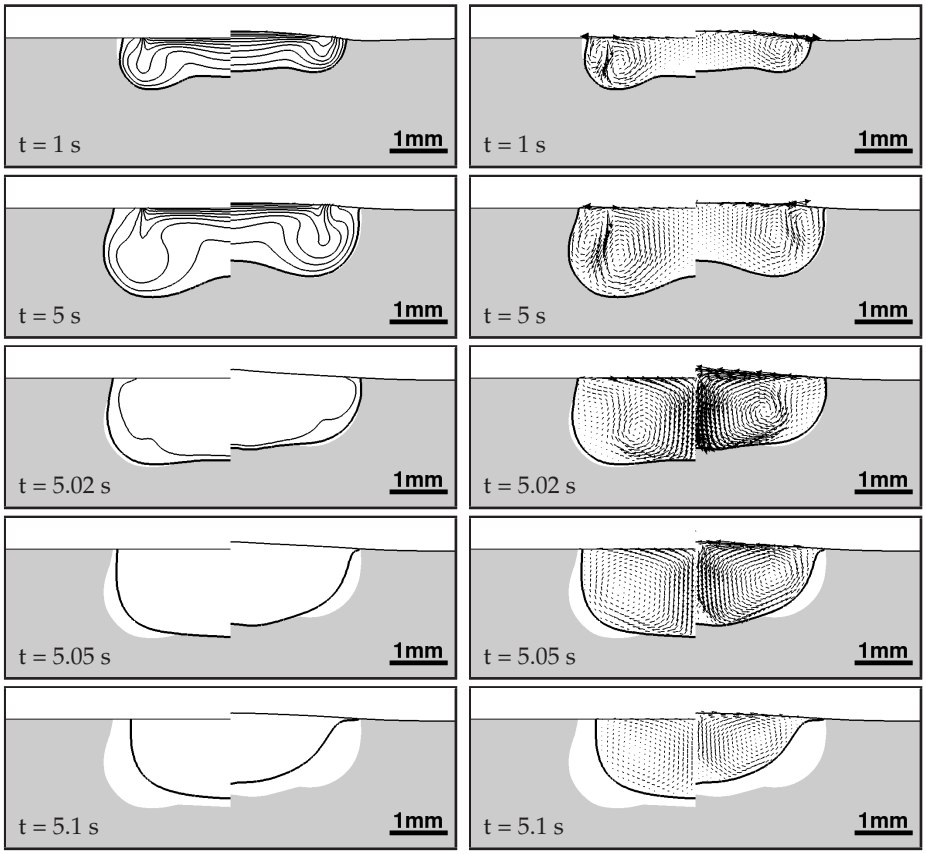

Figure 5.4. Comparison of weld pool temperature (left) and velocity (right) fields for 3850 W, 150 ppm S, between flat (left) and free (right) surface simulations, f = 1. The isotherms start from 1620 K (the melting temperature) at the weld pool boundary, then continue from 1700 K onwards, with an increment of 100 K.

Figure 5.5 shows a comparison of the time evolutions of maximum temperature in the weld pool, between flat and free surface simulations. A comparison of the time evolutions of maximum velocity magnitudes is given in figure 5.6. In general, maximum velocities are lower for the free surface case, probably due to an enhanced momentum transport by means of free surface oscillations (indicated by strong oscillations in the velocity plots). The maximum temperature for the free surface case, on the other hand, is lower for 20 ppm, but higher for 150 ppm, compared to the flat surface case. This can be understood as follows: For 20 ppm S, the flow is outward along the free surface, carrying heat from the hot center to the cooler edges, thus reducing the maximum temperature. When, due to flow instabilities, convective heat transfer is increased, this further reduces the maximum temperature.

For 150 ppm S, on the other hand, the flow is inward, increasing the maximum temperature in the center. When, due to flow instabilities, convective heat transfer is increased, this further increases the maximum temperature.

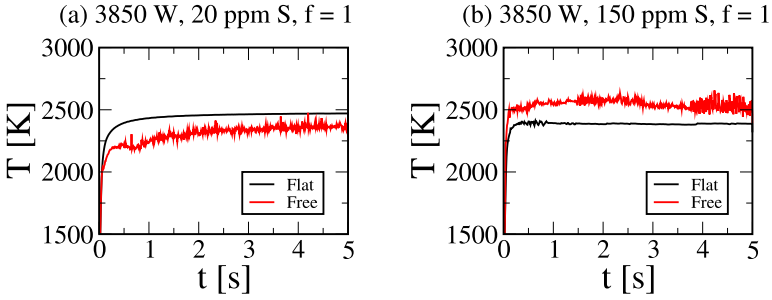

Figure 5.5. Time evolution of maximum temperature for cases (a) 3850 W, 20 ppm, f = 1; and (b) 3850 W, 150 ppm, f = 1.

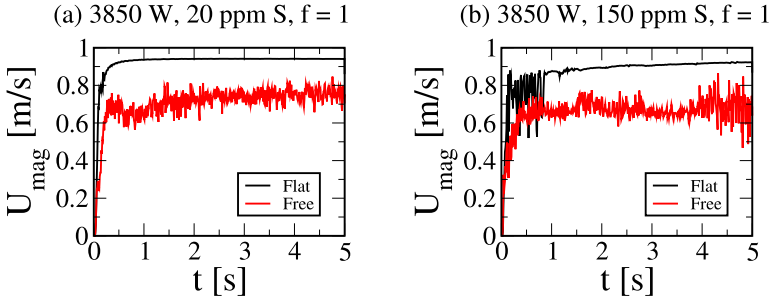

Figure 5.6. Time evolution of maximum velocity magnitude for cases (a) 3850 W, 20 ppm, f = 1; and (b) 3850 W, 150 ppm, f = 1.

A comparison of the time evolution of the free surface elevations at the weld pool center is shown in figure 5.7, and free surface shapes at several time instants are given in figure 5.8. Positive elevations in the center are obtained for the 150 ppm case, whereas negative elevations (surface depression) in the center are found for the 20 ppm case. As discussed above, surface elevation/depression depends on

the flow direction. For low sulfur concentration, the weld pool flow is outward, resulting in surface depression at the center. On the other hand, high sulfur concentration results in inward or counter-rotating flows initiated by inward flows, thus leading to a surface elevation at the center. From figure 5.7, we can see the influence of viscosity and thermal conductivity enhancements on the free surface oscillations, *i.e.* increased momentum and energy transport cause smaller oscillation magnitudes.

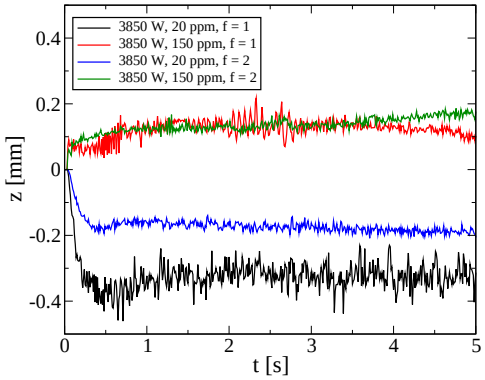

Figure 5.7. Time evolution of free surface elevations at the symmetry axis (weld pool center).

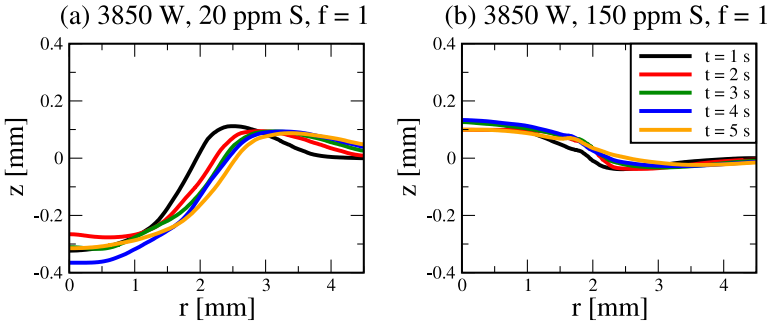

Figure 5.8. Free surface shapes at t = 1, 2, 3, 4, and 5 s for cases (a) 3850 W, 20 ppm, f = 1; and (b) 3850 W, 150 ppm, f = 1.

5.3.2 Mass and energy conservation

During the simulations, it is necessary to check whether conservations of mass and energy are satisfied. Some remarks to demonstrate this are given below.

Mass conservation

In figure 5.3, which is a 2-D axisymmetric case, although there is a free surface depression at the weld pool center, there is also an elevation at the edge. This elevation takes place from the weld pool edge to a certain radius outside the weld pool. This elevation is really small, hardly visible, but it is there due to the diffusive smearing of the weld volume fraction by the VOF method. If we integrate the solid-liquid melt in a 3-D cylindrical sense, the elevated volume at the edge is equal to the depressed volume in the center, thus mass is conserved, when compared to the corresponding flat surface simulation. This can also be checked by comparing the initial and final weld volume fractions. Below is the excerpt from the simulation logfile:

```
Time = 5e-06
DILUPBiCG: Solving for alpha1,
Initial residual = 0, Final residual = 0,
No Iterations 0
Liquid phase volume fraction = 0.810811
Min(alpha1) = 0 Max(alpha1) = 1

Time = 5
DILUPBiCG: Solving for alpha1,
Initial residual = 4.36812e-08, Final residual = 1.05766e-17,
No Iterations 2
Liquid phase volume fraction = 0.810794
Min(alpha1) = -2.50506e- 27 Max(alpha1) = 1
```

From the above, we see that the initial volume fraction is 0.810811 and the final (at 5 s) is 0.810794, which implies mass conservation.

Energy conservation

Energy conservation is satisfied if there is a balance between energy from the laser source (Q_{laser}) and energy in the computational domain (Q_{domain}), *i.e.* the following condition:

$$Q_{\text{laser}} = Q_{\text{domain}} \tag{5.1}$$

Assuming that there is no heat loss from the system, this equation can be written as:

$$Q_{\text{laser}} = \int_V \left[\rho h_{\text{ref}} + \int_{T_{\text{ref}}}^{T} \rho C_P dT + \rho \Delta H \right] dV \tag{5.2}$$

where in the right hand side of Eq. 5.2, the first two terms correspond to the sensible heat and the last term represents the latent heat of phase change.

In the numerical simulation, the above heat balance is considered to be satisfied if the error between Q_{laser} and Q_{domain} falls below a specified tolerance. The percentage of this error is given as:

$$\%\text{Error of } Q(t) = \frac{|Q_{\text{laser}}(t) - Q_{\text{domain}}(t)|}{Q_{\text{laser}}(t)} \times 100 \tag{5.3}$$

The specified tolerance for the heat error during simulation is chosen as 0.01%, and this is illustrated in figure 5.9, which corresponds to the free surface simulation of 3850 W and 20 ppm case (figure 5.3).

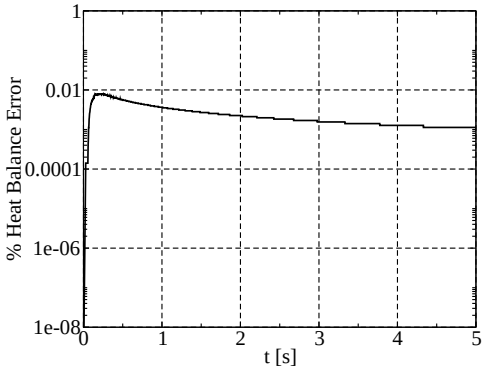

Figure 5.9. Time evolution of error percentage of heat balance for free surface simulation of case 3850 W, 20 ppm S.

5.3.3 Solidification stage

In order to compare the flow and temperature fields between flat and free surface simulations in the solidification stage (t $>$ 5 s), we refer back to figures 5.3 and 5.4, for 3850 W, 20 ppm sulfur and 3850 W, 150 ppm sulfur, respectively.

For 20 ppm, $d\sigma/dT$ is negative and remains negative during cooling down (see figure 4.2). As a result, the flow direction in the weld pool remains in the same direction, with slowly decreasing velocities, and the weld pool shape essentially stays the same during cool-down.

For 150 ppm, on the other hand, $d\sigma/dT$ is negative in the center part of the weld pool during heating, causing an outward flow. During cooling, $d\sigma/dT$ in the center changes from negative to positive, even becoming strongly positive when the weld pool cools down below 1800 K. This induces a strong inward flow, pushing the liquid metal down along the axis, and significantly deepening the weld pool during cool-down. This effect is stronger for the free surface case.

Comparisons of fusion zone shapes at t = 5 s and after solidification between flat and free surface simulations are given in figure 5.10, in which experimental results are also shown. For 20 ppm, both flat and free surface simulations show similarity between shapes at t = 5 s and after solidification. The fusion zones with free surface are deeper, yet slightly less wide than with flat surface. For 150 ppm, the fusion zones after solidification are deeper than those at t = 5 s. The fusion zones with flat surface simulation are slightly deeper than with free surface. However,

the deepening rate is higher for free surface cases. In terms of comparison with experiment, simulations incorporating solidification using f = 2 result in the best agreement, mainly with respect to fusion zone depth. As for the width, it is over-predicted in all simulations, regardless of f and whether free surface deformation and solidification are included.

The discrepancies between the predicted and experimental fusion zone shapes might be attributable to a missing aspect in the simulation. It is assumed that sulfur, as the element of interest in this case, is in an equilibrium state. In other words, its transport along the free surface and to/from the bulk weld pool flow is not taken into account. In reality, flow is likely to redistribute it and influence its local concentration and gradients at the free surface. This implies that surface tension gradients might be different from what have been predicted here. For instance, for 20 ppm sulfur, the experimental fusion zone shape is narrower than predicted. This could be due to a high sulfur concentration locally at the edge, which is brought about by the outward flow from the center. Such high concentration could change the local $d\sigma/dT$ such that an inward flow at the edge might occur. Similarly for 150 ppm, a high sulfur concentration at the edge might also intensify the inward flow, so as to cause a deeper weld pool than predicted.

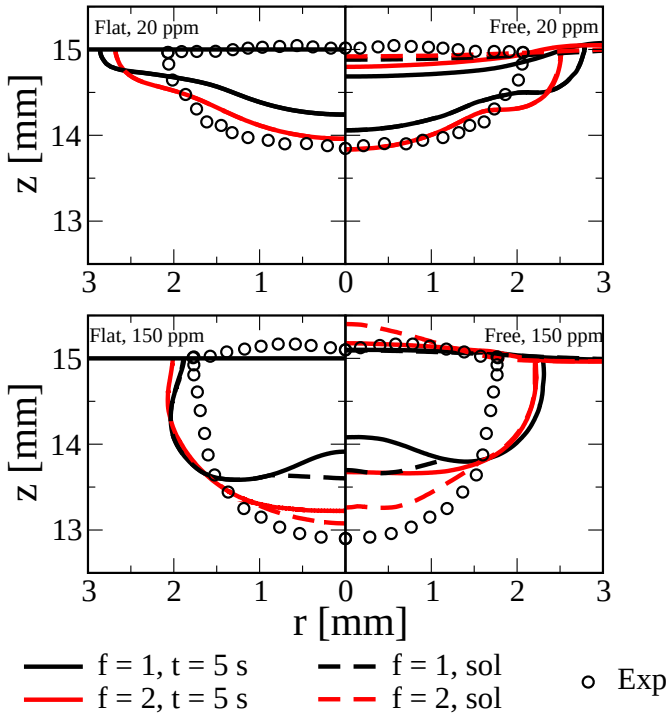

Figure 5.10. Comparisons of predicted fusion zone shapes for case 3850 W, 20 ppm S (top) and 150 ppm S (bottom) with f = 1 and 2 at t = 5 s and after solidification between flat (left) and free (right) surface simulations, as well as experimental results from Pitscheneder et al. (1996). Note that for the flat and free surface simulations in case of 20 ppm S, the fusion zone boundaries for f = 1 at t = 5 s coincide with those after solidification.

5.4 Concluding remarks

This chapter presents results of 2-D, axisymmetric weld pool simulation incorporating free surface deformation for the same cases that were studied in chapter 4 with flat surface assumption.

It has been shown that free surface simulation results in somewhat different flow and temperature fields, as well as fusion zone shapes, compared to flat surface simulation. In general, free surface oscillation leads to lower maximum velocities, indicating an enhanced momentum transfer. For low element concentration, where an outward convective heat transfer occurs, the enhanced outward convective heat transfer also lowers the maximum temperature at the center. For high element concentration, enhanced inward convective heat transfer leads to an increased temperature in the center. Such a difference in mechanism of convective heat transfer between flat and free surface flows might indicate that the two cases could also be different when the transport of surface active element is considered. When element mixing is of main interest, accounting for free surface deformations is thus essential.

With respect to fusion zone shapes, for low sulfur concentration, a deeper weld pool is obtained with a free surface, due to a depressed free surface in the center caused by the outward flow. On the other hand, for high sulfur concentration, flat surface simulation gives a deeper weld pool. Furthermore, during the solidification stage an inward flow occurs for high element concentration, but not for low concentration. This results in a deepening of the weld pool for high concentration case, where the penetration rate for free surface case is slightly higher than for flat surface case.

In both flat and free surface case, using an enhancement factor $f = 2$ results in a fairly good prediction of experimental fusion zone depth, when solidification is taken into account. It can therefore be concluded that the need for the use of a much higher enhancement factor $f = 7$ in the reference paper by Pitscheneder et al. (1996) might be due to the absence of the solidification stage in the simulation.

In general, the predicted fusion zones are still somewhat different from the experimental results, mainly in terms of width. A possible factor could be that the current model does not account for redistribution of surface active elements (sulfur in this case). Accumulation of sulfur at the edge due to outward flow might occur in reality and this could alter the Marangoni-driven flow and energy transfer, and hence fusion zone shapes.

6 CHAPTER

Simulations of laser spot weld pool flows influenced by oxygen absorption

6.1 Introduction

This chapter reports numerical simulations of laser spot weld pool hydrodynamics influenced by oxygen absorption from the environment, based on the experiments by Zhao (2011). In conjunction with temperature, the concentration of oxygen as surface active element affects the surface tension distribution at the weld pool surface. This affects the Marangoni forces acting at the free surface and thus also the flow and heat transfer in the weld pool, which consequently also influence the final fusion zone shape.

The effects of surface active elements on Marangoni flows in weld pools as well as fusion zone shape have been reported widely in literature. Heiple and Roper (1982) and Heiple et al. (1983) showed that a minor presence of surface active elements can substantially change the temperature dependence of surface tension, affecting the flow patterns and eventually the fusion zone geometry. Zacharia et al. (1990) demonstrated numerically that the effect of surface active elements is a strong function of surface temperature and, hence, the welding parameters. Aidun and Martin (1997) reported that an increase in the oxygen content leads to an increase in the depth-to-width ratio of the fusion zone of both low- (type 304) and high-sulfur (type 316) stainless steel in laser welding. Winkler et al. (2000) developed a physicochemical transport model to approach the transport of surfactants at the surface and in the bulk flow of Gas Tungsten Arc weld pools, in contrast to the generally used assumption of a uniform surfactant concentration in the weld. Using this model, they were able to predict the accumulation of sulfur at the stagnation points at the surface (regions where two counter-rotating Marangoni-driven vortices meet), which was validated by microstructure experiments. Moreover, Winkler and Amberg (2005) extended the model to deal with the ternary Fe-S-O system and showed that a better agreement with experiments

was obtained.

In the experiment by Zhao (2011), cases with different oxygen levels in the environment, varying from 59 ppm to 20.9%, were studied. At low ambient oxygen levels (lower than 3.1% for the studied welding condition), outward weld pool flows were present without any observed inward flows. At sufficiently high ambient oxygen levels, a transition in flow direction occurred during the welding process, *i.e.* at a specific moment during welding, the initially outward flow reversed into an inward flow. Moreover, for low ambient oxygen levels, the dissolved oxygen in the weld pool was found to be uniformly distributed, whereas it was non uniform at high ambient oxygen levels that caused flow reversals. At high ambient oxygen levels, the laser absorptivity is also high, which in combination with the inward flow led to a full penetration of the weld pool. This resulted in a presence of an additional free surface at the bottom of the material, causing more complex flows. The cross sections of the experimental solidified fusion zones for varying ambient oxygen level are shown in figure 6.1.

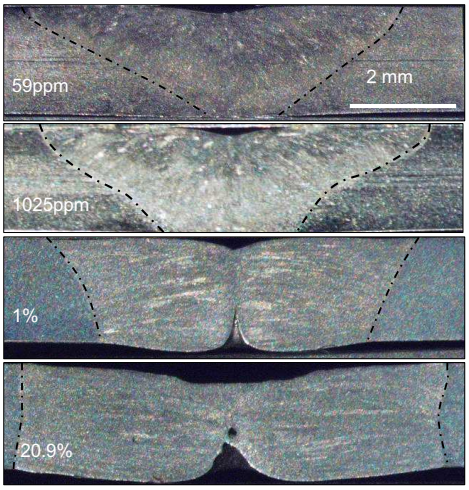

Figure 6.1. Cross sections of the solidified fusion zones for ambient oxygen concentrations of 59 ppm, 1025 ppm, 1%, and 20.9%. (Zhao (2011)).

In this chapter, we consider the experimental case of 59 ppm ambient oxygen concentration, since based on the experimental findings this is the most representative case of the conduction mode welding pertaining to our simulation code, *i.e.* full penetration occurred but hardly induced a secondary free surface deformation at the bottom boundary.

6.2 Problem description

6.2.1 Process parameters and material properties

In the experiment, a sample of stainless steel SS304 with the following dimensions is used: length $\times$ thickness $\times$ width = 20 mm $\times$ 2 mm $\times$ 20 mm. During 1 second, the sample was subjected to a stationary Nd:YAG laser beam with power of 2808 W and a beam radius of 6.3 mm. The sample was confined in a closed chamber, in which the concentration of oxygen as the active element of interest can be controlled. The experimental setup is sketched in figure 6.2, and the material properties and process parameters are given in table 6.1.

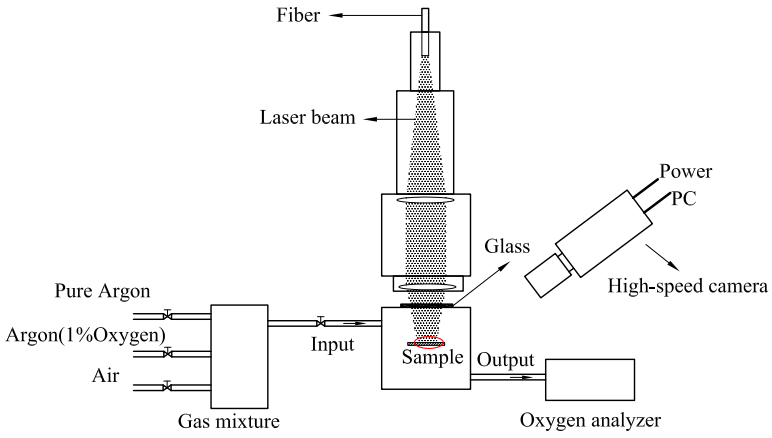

Figure 6.2. Experiment setup (Zhao (2011)).

Property/parameter	Value	Unit
Solid and liquid metal density, ρ	7200	kg/m^3
Molecular value of dynamic viscosity of liquid, μ	0.006	$kg/(m \cdot s)$
Surface tension, σ_0	1.9	N/m
Solidus temperature, T_S	1697	K
Liquidus temperature, T_L	1727	K
Specific heat of solid and liquid, C_p	712	$J/(kg \cdot K)$
Thermal conductivity of solid, k_S	15	$W/(m \cdot K)$
Thermal conductivity of liquid, k_L	33	$W/(m \cdot K)$
Latent heat of melting, L	2.47×10^5	J/kg
Laser power, Q	2808	W
Laser absorptivity, η (see section 6.2.4)	0.5	-
Laser beam radius, r_q	6.3	mm

Table 6.1. Material properties and process parameters

6.2.2 Estimation of oxygen absorptivity

During welding, oxygen from the ambient gas mixture in the chamber is absorbed into the weld pool and thus affects the surface tension. The transient absorption of oxygen by the liquid steel is a complex process, as it depends on the surface conditions, *i.e.* local temperature and the presence or absence of a surface oxide layer. The surface oxide layer is formed by the reaction between the absorbed oxygen and other components in the weld pool. All the involved components can be convected along the free surface as well as transported to and from the bulk weld pool flow. Our current model does not take into account the transient transport of species and thus we relied on an estimation of the oxygen concentration in the weld pool, which is needed for the calculation of the surface tension gradients. As an initial estimate, we assumed that the oxygen concentration in the metal was equal to the oxygen concentration in the gas.

6.2.3 Temperature gradient of surface tension

Having obtained the estimated oxygen content in the weld, we can use the model by Sahoo et al. (1988) (Eq. 4.3 and 4.4) to obtain the temperature gradient of surface tension as a function of temperature, shown in figure 6.3 for several oxygen concentrations. The corresponding parameters in Eq. 4.3 and 4.4 for the Fe-O system are given in table 6.2.

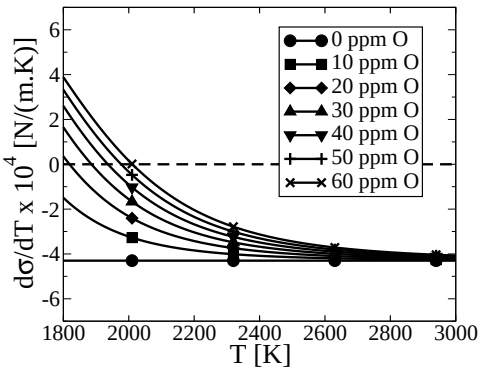

Figure 6.3. Temperature gradient of surface tension as a function of temperature and oxygen level in the Fe-O system.

6.2.4 Laser absorptivity

In addition to the uncertainty in the oxygen level in the weld pool, the laser absorptivity is also not accurately known. Laser absorptivity is dependent on surface cleanliness and degree of oxidation. The higher the oxidation is, the more laser energy is absorbed. This is indicated by the decrease of the melting onset

Parameters	Values	Units
$\frac{d\sigma}{dT}\Big\vert_0$	-4.3 $\times$ 10^{-4}	N/(m $\cdot$ K)
Γ_S	2.03 $\times$ 10^{-8}	kmole/m^2
k_1	0.0138	-
ΔH^0	-1.463 $\times$ 10^8	J/(kmole)
$\Delta \overline{H}_i^M$	0	J/(kmole)

Table 6.2. Parameters for the calculation of temperature gradient of surface tension for Fe-O system.

time as the ambient oxygen level is increased, as shown in table 6.3. In the experiment, a calorimeter measurement was carried out in order to determine how much laser energy is absorbed for a certain ambient oxygen level. For the case being studied here, *i.e.* 59 ppm oxygen in ambient, the suggested laser absorptivity is 50%.

Ambient oxygen level	Melting onset time (s)
59 ppm	0.1441
1025 ppm	0.1384
1%	0.1171
20.9%	0.0266

Table 6.3. Melting onset time obtained from experiment by Zhao (2011).

6.3 Simulation settings

6.3.1 Mesh size

The employed 3-D mesh is shown in figure 6.4. In the x- and z-direction, we used grid cells with uniform size of $\Delta x = \Delta z$ = 0.05 mm to cover the 10 mm $\times$ 10 mm area in the center of the sample, where high temperature gradients and velocities are expected to occur. The size of this center region was also determined based on the observed weld pool size in the experiment. Outside this center area, towards the edge, the grid cell size is gradually increased. In the y-direction, cells with Δy = 0.02 mm are used in the vicinity of the initial free surface, in order to accurately capture the free surface deformation, and are gradually expanded towards the bottom and the top boundaries of the domain. The cell thickness Δy = 0.02 mm is 10% of the observed maximum surface elevation/depression in the experiment (0.2 mm). In total, the employed 3-D mesh is 224 $\times$ 60 $\times$ 224, *i.e.* 3,010,560 computational cells.

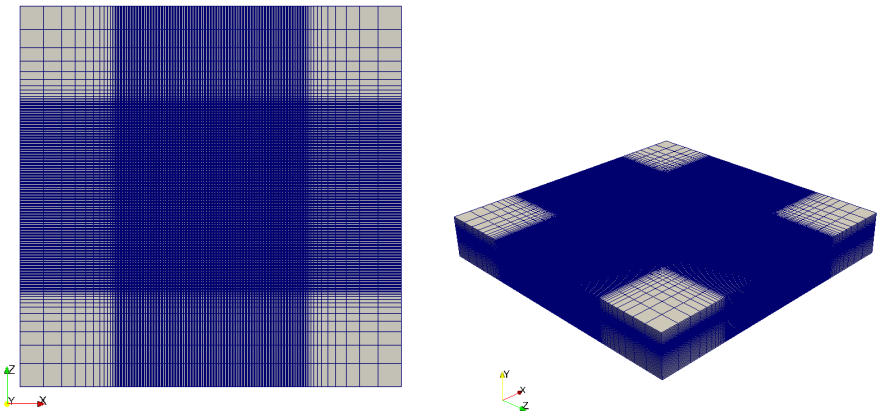

Figure 6.4. Mesh used in this chapter: Top view (left) and 3-D perspective (right).

6.3.2 Boundary conditions

The boundary conditions are similar to those used in 2-D axisymmetric free surface simulation in section 5.2.2, with the only difference being that no symmetry axis is present in the 3-D simulation in this chapter.

6.3.3 Numerical schemes

The Navier - Stokes and energy equations are solved using a higher-order NVD scheme with Minmod flux limiters. The VOF equation is solved using the Gamma scheme combined with a MULES (Multi-dimensional Universal Limiter with Explicit Solution) solver. The transient terms are handled using a first-order fully implicit time integration scheme. The time step is controlled by a maximum Courant number $Co < 0.1$, associated with the typical time step of 1×10^{-5} s. Convergence is satisfied if the pressure residual is lower than 10^{-8}, and the residuals of volume fraction, velocity, and temperature are lower than 10^{-12}.

6.3.4 Computational speedup

OpenFOAM features the capability of parallel simulation on a number of processors for computational speedup. For the 3-D simulations in this chapter, we made use of 16 processors. Before running the simulation, the 3-D mesh was decomposed into a number of subdomains, each of which is associated with a single processor (figure 6.5 (left), for 16 processors). Speedup performance of OpenFOAM based on simulations on 1, 2, 4, 8, and 16 processors is shown in figure 6.5 (right). Using 16 processors, computation speedup is 5.

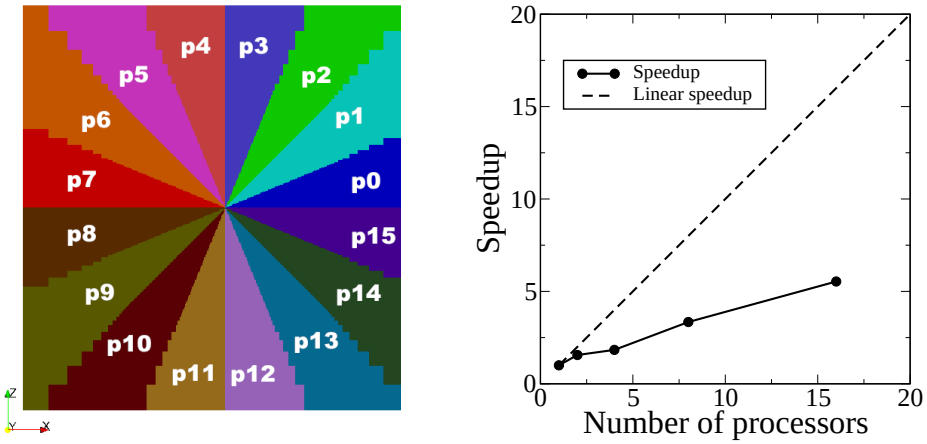

Figure 6.5. Top view of 16 computational subdomains after decomposition (left) and computational speedup obtained for 3-D free surface simulations (right).

6.4 Results and discussion

6.4.1 Cell Peclet number

When simulating fluid flows with high Reynolds numbers using high order spatial discretization schemes, one can encounter numerical problems which may also manifest in unrealistic physics of the flow. It is important to keep the cell Peclet number below some critical number, normally below 2 (Hirsch (2007)) to avoid such instability. The cell Peclet number is defined as

$$\mathrm{Pe}_{\mathrm{cell}} = \frac{U\Delta}{\nu} \tag{6.1}$$

where U is the velocity, Δ the grid spacing, and ν the kinematic viscosity.

In order to remedy the instability problem, one can reduce the mesh size Δ such that the condition $\mathrm{Pe}_{\mathrm{cell}} < 2$ is satisfied throughout the computational domain. However, for the current problem with $U \sim 1$ m/s and $\nu \sim 10^{-6}$ m^2/s, we need $\Delta \sim 10^{-3}$ mm to satisfy this requirement, which makes the computational cost quite prohibitive. An alternative would be to use a hybrid scheme, which combines the use of 1st-order upwind scheme in the region with $\mathrm{Pe}_{\mathrm{cell}} > 2$, and CDS when $\mathrm{Pe}_{\mathrm{cell}} < 2$. Unfortunately, we would have a large region with $\mathrm{Pe}_{\mathrm{cell}} > 2$, making most of the solution only 1st-order accurate.

A recommended way is to use schemes with nonlinear limiters to ensure monotonicity of solutions. With the use of such schemes, one can perform simulations with $\mathrm{Pe}_{\mathrm{cell}} > 2$. The superiority of schemes with nonlinear limiters to tackle convection dominated numerical simulations was reported by Wang and Hutter

(2001), where low numerical errors were obtained for cases with $\mathrm{Pe}_{\mathrm{cell}} > 10$. This approach is used in this thesis.

In the current simulation, we checked the results on coarse and fine meshes. The number of cells in these meshes are 752,640 and 3,010,560, respectively. In figure 6.6, we compare free surface velocities, temperature contours, and local cell Peclet numbers between the coarse and fine mesh. It is clear that on the coarse mesh, the flow and the temperature fields in the weld pool center take a square-ish shape, which is unlikely to be physical, and the weld pool flow is asymmetric. Such a peculiarity is confirmed by the very high cell Peclet numbers on this mesh, around 15 in the center and 30 at the pool edge. On the other hand, on the fine mesh the velocity field and the temperature contours look circular and symmetric, which seems to be much more realistic. The cell Peclet number in the weld pool is also lower than that on coarse mesh, taking maximum values of around 7.5 near the pool edge.

6.4.2 Mass conservation

To check mass conservation in our simulations of free surface weld pool flows using the Volume of Fluid approach, we monitor the total metal mass in the computational domain, which corresponds with the integrated volume fraction ($\gamma_1 = \int_V \gamma dV_1$). In figure 6.7, we plot the time evolution of error percentage of weld sample volume fraction:

$$\%\text{Error of } \gamma_1 = \frac{|\gamma_1 - \gamma_{1\ t=0}|}{\gamma_{1\ t=0}} \times 100 \tag{6.2}$$

The error is still very low at t = 1 s, *i.e.* below 0.005%. This certainly gives confidence that mass conservation is well satisfied during simulation.

6.4.3 Melting onset

Checking the melting onset time in the simulation is important as it can give some feeling on whether the laser absorptivity of 0.5, as suggested by experiment (section 6.2) is accurate. The melting onset time in the simulation can be obtained by *e.g.* monitoring the weld pool maximum temperature in time. Melting starts as soon as the maximum temperature exceeds the melting temperature.

From figure 6.8, the simulated melting onset time is found to be 0.12 s, which is very close to the 0.1441 s in experiment. Accordingly, we assume that the energy rate absorbed in the simulation is representative of that in experiment.

6.4.4 Free surface flow and temperature fields

Top view snapshots of the in-plane free surface velocity and temperature fields at t = 0.3, 0.5, 0.7, and 1 s, for an oxygen concentration of 59 ppm in the weld pool,

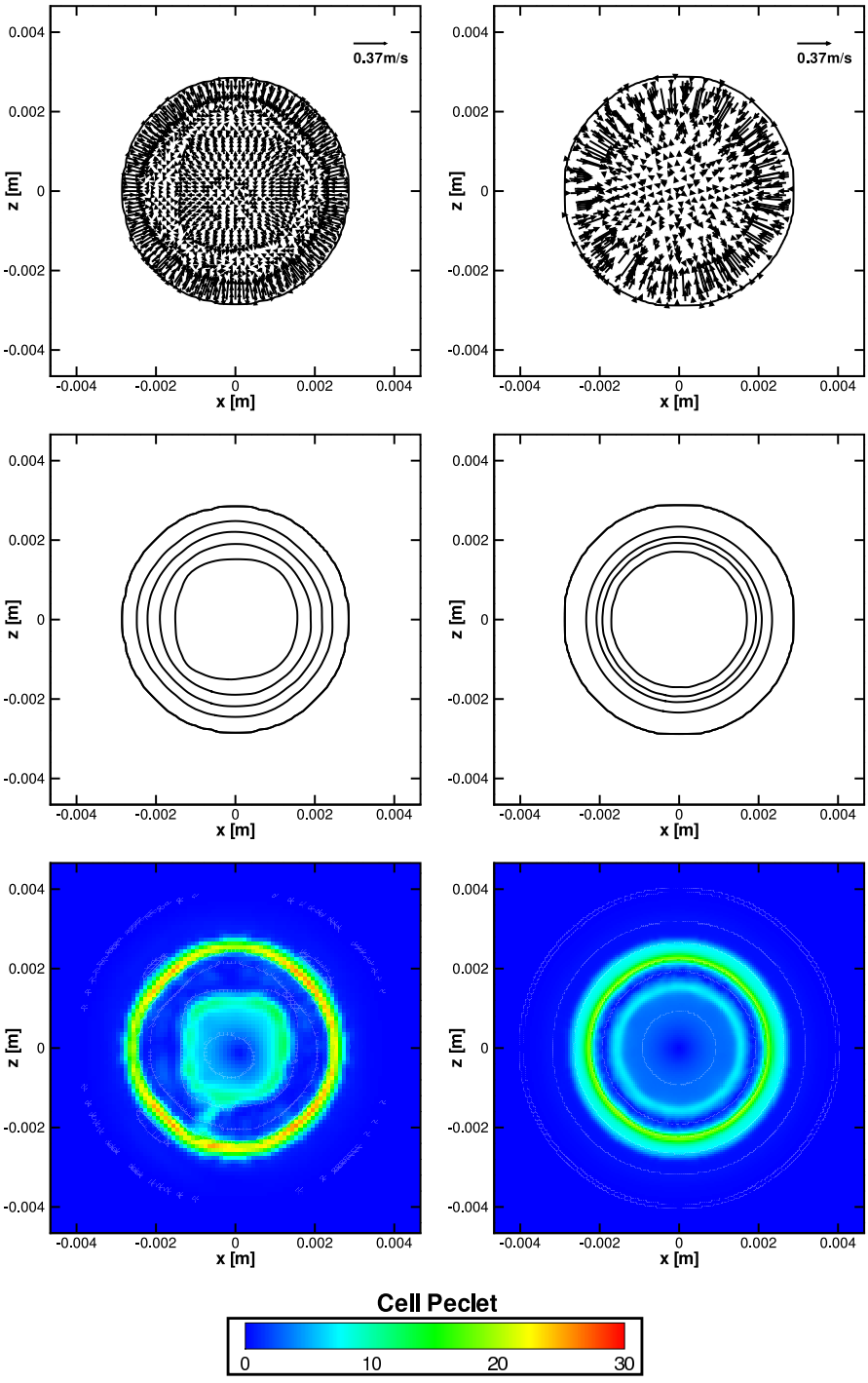

Figure 6.6. Top view of free surface velocities (top), temperatures (middle), and cell Peclet numbers (bottom) for coarse (left) and fine (right) meshes at t = 0.4 s. Note: temperature isotherms are 1712, 1800, 1900, 2000, and 2100 K.

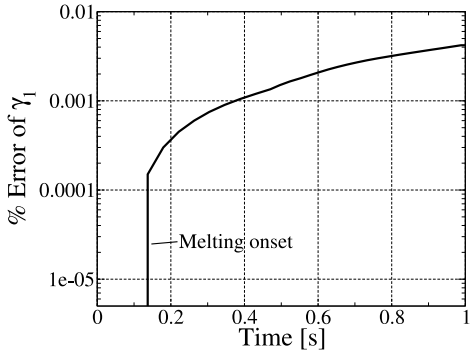

Figure 6.7. Time evolution of error percentage of weld sample volume fraction.

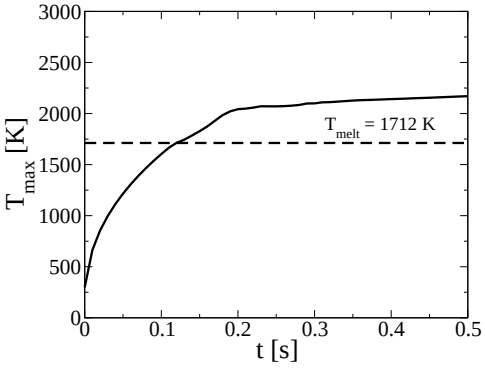

Figure 6.8. Time evolution of maximum temperature

are shown in figure 6.9 and 6.10, respectively. At t = 0.3 s, the flow in the center part (up to the radius of approximately half of the weld pool radius) is outward, whereas it is inward near the edge. The outward flow is caused by the negative values of the surface tension gradient in the high temperature region (higher than approximately 2000 K, figure 6.3), while the positive surface tension gradient near the edge causes the inward flow. The velocity magnitude near the edge, however, is considerably larger than that in the center. This is due to higher surface tension gradient magnitude and higher temperature gradient at the pool edge. As time progresses, in the center the temperature gradients are increased, resulting in a velocity increase and a larger region of outward flows.

Numerical results showed symmetrical surface flows for an oxygen concentration in the weld pool of 59 ppm. Consequently, the shape of the weld pool is also circular. The inward flow at the edge observed numerically is not confirmed in experiment, where there was no inward flow observed for an ambient oxygen concentration below 3.1% (Zhao (2011)). This suggests that the oxygen concentration of 59 ppm used in the simulation, which is equal to the oxygen level in the environment, might be higher than that actually absorbed in experiment.

At 59 ppm oxygen in the metal, $d\sigma/dT$ takes both positive and negative values over the temperature range observed in the weld pool (see figure 6.3, $d\sigma/dT > 0$ for T $<$ 2000 K and $d\sigma/dT < 0$ for T $>$ 2000 K). At lower oxygen concentration in the metal, the temperature at which $d\sigma/dT$ changes sign is lowered. At an oxygen concentration of 20 ppm, for instance, the sign change in $d\sigma/dT$ occurs at T $\approx$ 1900 K, resulting in a much smaller and weaker region of inward flow.

6.4.5 Cross section and surface elevations

Figure 6.11 shows cross sectional views of temperature and velocity fields of the weld pool with 59 ppm oxygen at t = 0.3, 0.5, 0.7, and 1 s. Two counter-rotating flows, inward and outward, are shown to coexist in the weld pool due to the presence of regions with negative and positive surface tension gradients.

The presence of the two counter-rotating vortices influences the way in which the free surface deforms. Figure 6.12 shows the 3-D free surface elevation at t = 0.3 and 1 s, and the time evolution of free surface elevation at the weld pool center point. Initially, at t = 0.3 s, the inward flow at the edge is more dominant than the outward flow in the center since temperature gradients in the periphery are larger than in the center. The higher inward velocities lead to the elevation of the weld pool surface in the center. As time progresses until t = 0.7 s, the outward flow in the center becomes stronger and somewhat balances the inward flow at the edge, causing the free surface to flatten.

We can also relate our prediction on weld pool flow velocities and the free surface deformations by calculating the Capillary number of the studied problem. According to figure 6.11, the average temperature at the weld pool surface is around 2100 K. For 59 ppm of oxygen, this corresponds with a $d\sigma/dT$ of around -1 $\times$ 10^{-4} N/(m.K) (figure 6.3). Using a temperature difference $\Delta T = T_{max} - T_m \simeq 600$ K and a surface tension σ_0 = 1.9 N/m, the Capillary number (Eq. 1.8) is 0.03. This

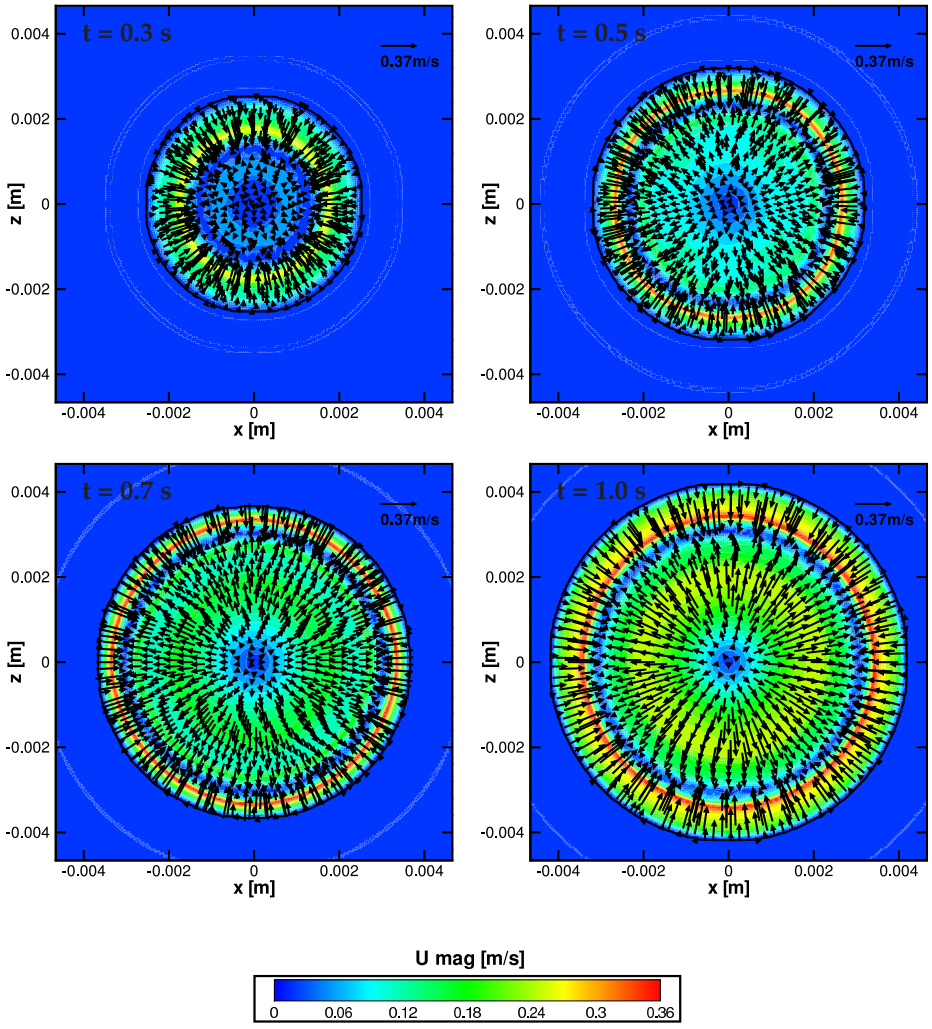

Figure 6.9. Top view of free surface flow fields, t = 0.3, 0.5, 0.7, 1 s. Ambient oxygen content is 59 ppm. The maximum vector at each time instant is 0.272, 0.352, 0.375, and 0.354 m/s, respectively.

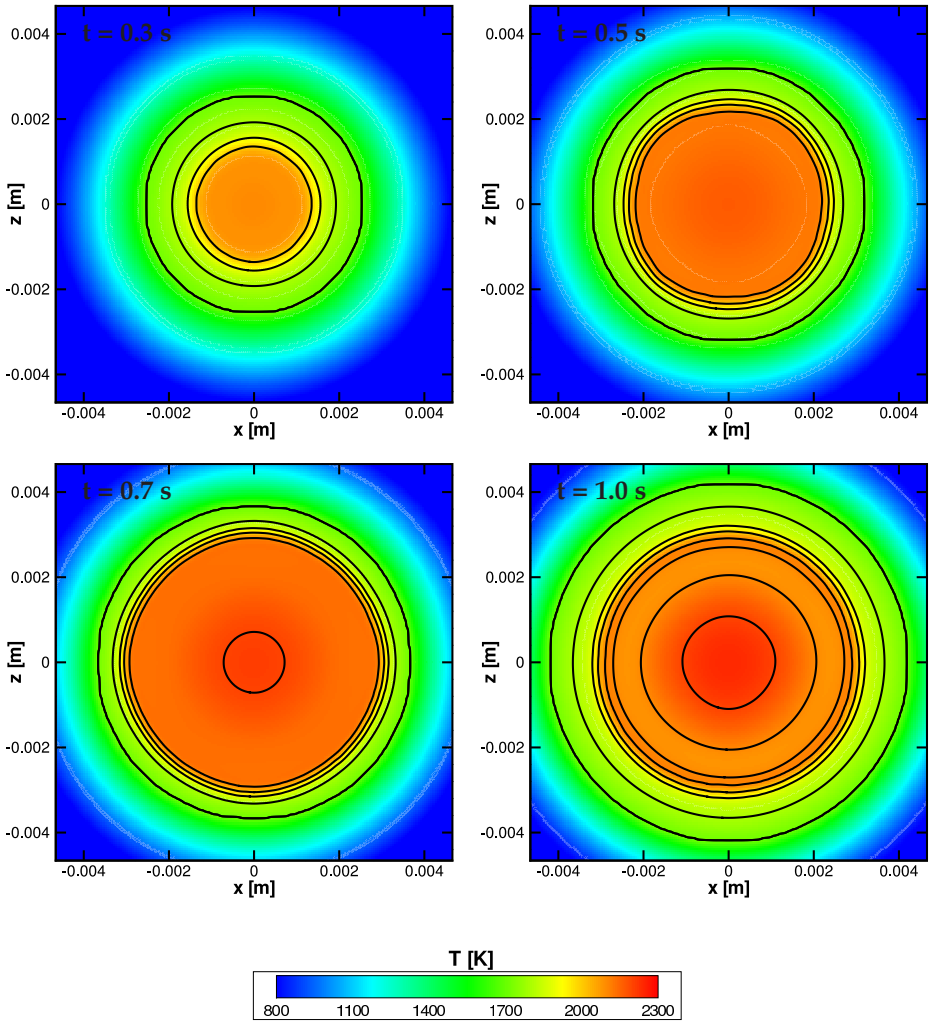

Figure 6.10. Top view of free surface temperature fields, t = 0.3, 0.5, 0.7, 1 s. Oxygen content is 59 ppm. The isotherms start from 1712 K (the melting temperature) at weld pool boundary, then continue from 1800 K onwards, with increment of 100 K.

low value implies a small deformation, which is the case in figure 6.12, *i.e.* the maximum deformation is only 3% of the material thickness or around 0.06 mm.

Up to t = 0.5 s, the weld pool depth decreases monotonically from the center to the edge. At the later stage, t = 1 s, the strong inward flow at the edge contributes to intensifying the heat transfer to the base of the pool. This causes a wavy shape of the weld pool. Such weld pool shape is consistent with the numerical findings and analysis by Wei et al. (2009), who showed that a wavy shape can be obtained for a Marangoni number Mg $> 10^2$ and a Prandtl number Pr < 0.1. The simulation results considered here are associated with Mg = 2000 and Pr = 0.1.

As addressed earlier in section 6.4.4, assuming the oxygen concentration in the weld pool to be equal to that in the environment, *i.e.* 59 ppm, leads to the presence of two counter-rotating flows, which were not observed in the experiment. In addition to 59 ppm, simulations using oxygen contents of 20 and 30 ppm were also carried out to test the hypothesis that the actual oxygen content in the weld pool should be lower than 59 ppm. The temperature and velocity fields obtained from these two additional simulations are given in figure 6.13 and 6.14. The time evolution of temperature and velocity fields, as well as weld pool shapes, are very similar for oxygen concentrations of 20 and 30 ppm. Owing to the negative $d\sigma/dT$, the flows are outward, as is observed in the experiment. There is a slight difference at the periphery though, where it seems that a small inward vortex starts to occur for 30 ppm at the later stage. Accordingly, the shape of 30 ppm looks more wavy at the periphery than that for 20 ppm.

Figure 6.15 shows a comparison of the weld pool width, normalized by the laser spot diameter, between experiment with 59 ppm ambient oxygen and simulations with material oxygen contents of 20, 30, and 59 ppm. In the simulations, a lower oxygen concentration leads to a wider weld pool. This is due to the negative $d\sigma/dT$ that results in outward flow and a very weak or no inward flows at the edge. The case of 20 ppm thus gives the best agreement with experiment.

Figure 6.16 shows comparisons between cross sectional post-solidification weld shape from experiment, and simulations with different oxygen contents. It must be noted that the simulation results shown in this figure are based on the melting front position at t = 1 s, when the laser was switched off. Therefore, it is not surprising to see that the simulated weld pools are not as deep as the solidified experimental weld. It is thus important to extend the simulation into the solidification regime after the laser is switched off, in order to have a more proper comparison of fusion zone shapes. This will be discussed further in section 6.4.7.

6.4.6 Comparison with 2-D axisymmetric simulations

It is interesting to compare the full 3-D results with 2-D axisymmetric results. Comparisons of cross sectional velocity and temperature fields are given in figure 6.17 and 6.18, respectively. It is obvious that the velocity direction and magnitude, temperatures, surface elevations, and weld pool shapes are in a very good agreement with each other. However, at t = 1 s, the 2-D inward velocity magnitude in

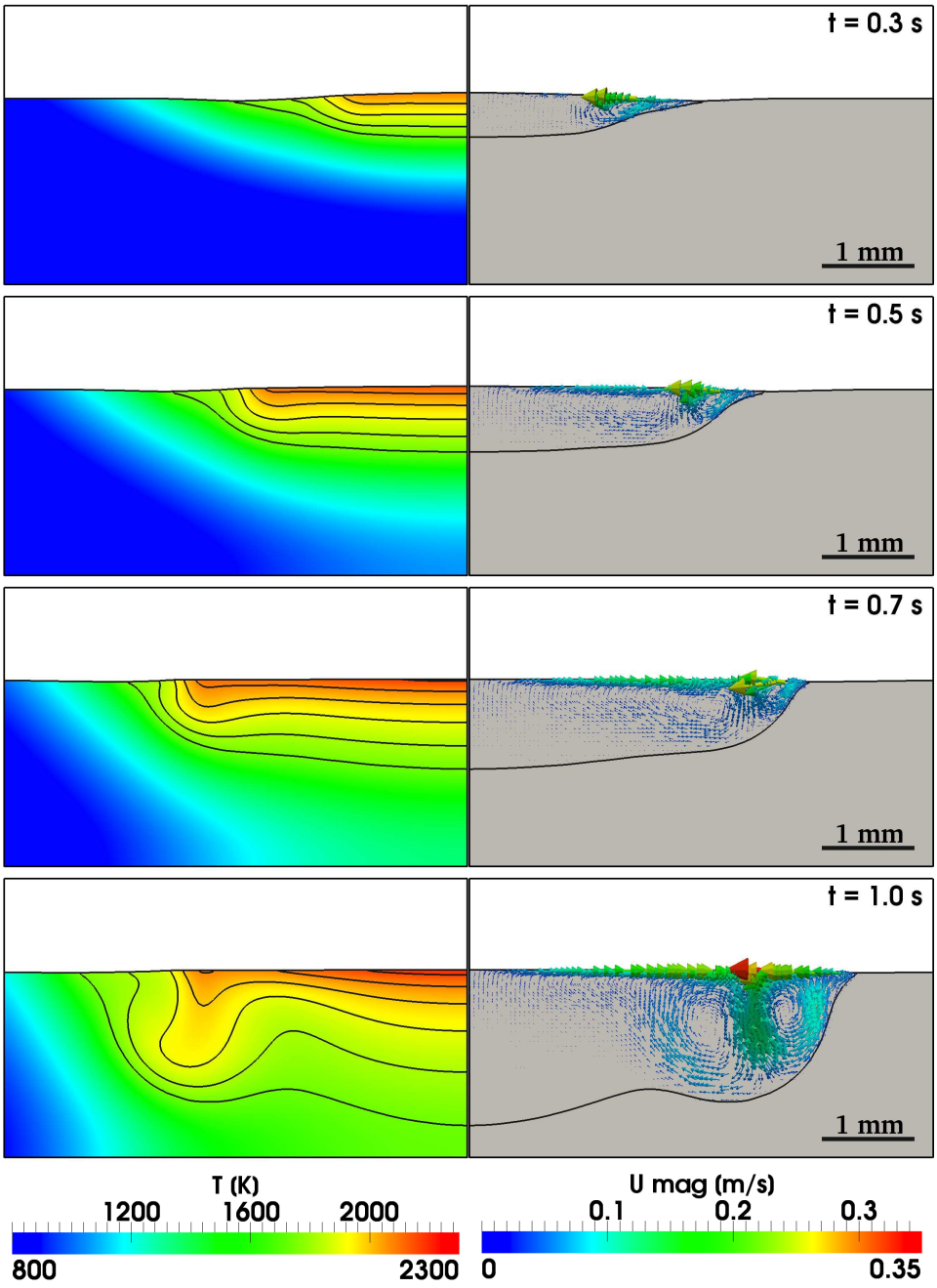

Figure 6.11. Cross sectional views of temperature (left) and velocity (right) fields, t = 0.3, 0.5, 0.7, 1 s. Oxygen content is 59 ppm. The isotherms start from 1712 K (the melting temperature) at weld pool boundary, then continue from 1800 K onwards, with increment of 100 K.

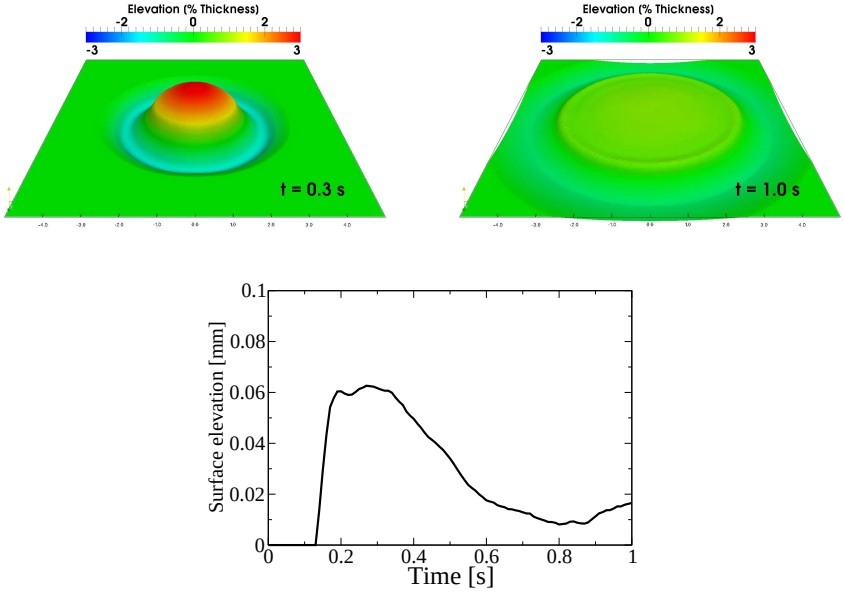

Figure 6.12. Free surface elevation at t = 0.3 s (top left) and 1 s (top right). (Note: The vertical scale is different from the horizontal scale, where a factor of 20 is used). Time evolution of the free surface elevation at the center point ([x, z] = [0, 0] mm) (bottom). Oxygen content in the weld is 59 ppm.

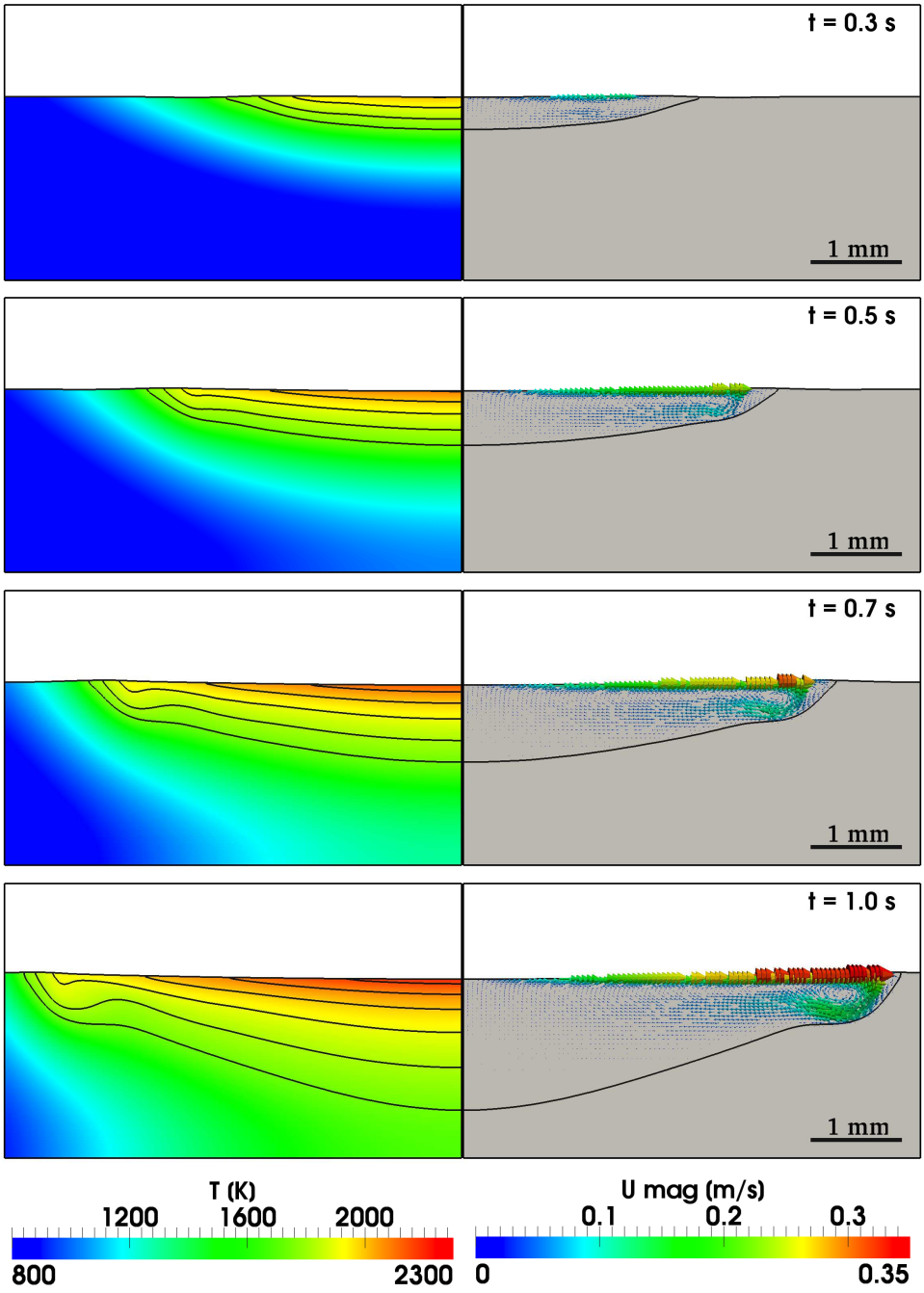

Figure 6.13. Cross sectional views of temperature (left) and velocity (right) fields, t = 0.3, 0.5, 0.7, 1 s. Oxygen content is 20 ppm. The isotherms start from 1712 K (the melting temperature) at the weld pool boundary, then continue from 1800 K onwards, with an increment of 100 K.

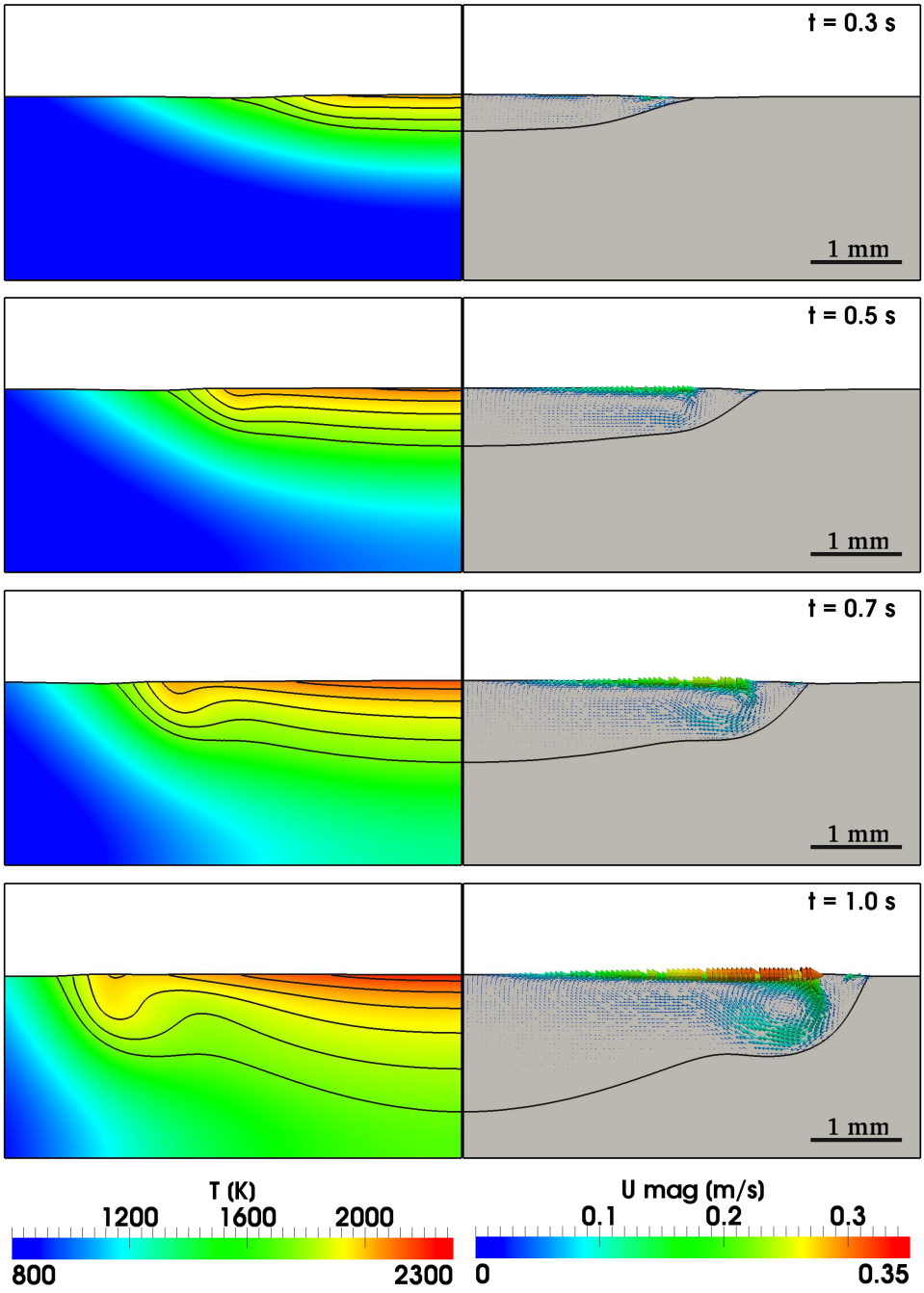

Figure 6.14. Cross sectional views of temperature (left) and velocity (right) fields, t = 0.3, 0.5, 0.7, 1 s. Oxygen content is 30 ppm. The isotherms start from 1712 K (the melting temperature) at the weld pool boundary, then continue from 1800 K onwards, with an increment of 100 K.

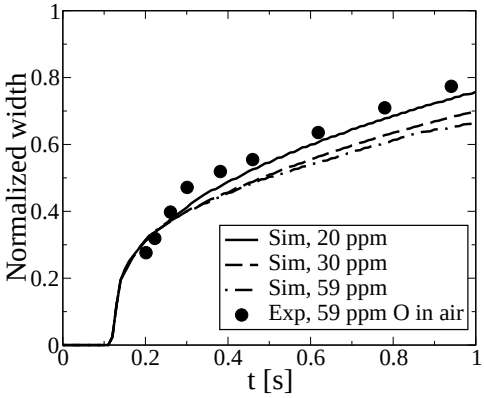

Figure 6.15. Comparison of weld pool width normalized by laser spot diameter between experiment with 59 ppm oxygen in environment and simulations with material oxygen contents of 20, 30, and 59 ppm.

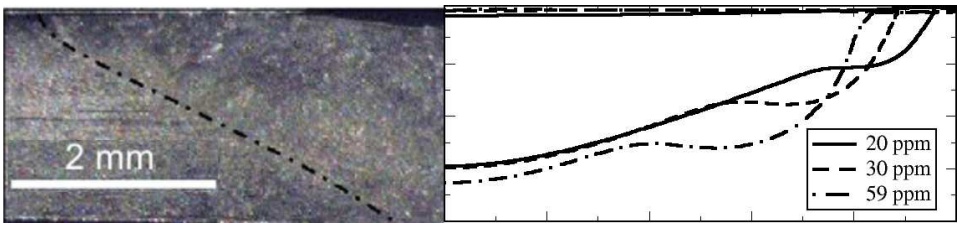

Figure 6.16. Comparison of cross sectional solidified weld shape from experiment (left) and weld shapes based on melting front position at t = 1 s predicted by simulations with varying oxygen contents (right).

the periphery is lower than that of the 3-D simulation. This results in a weaker inward flow and a less wavy weld pool shape.

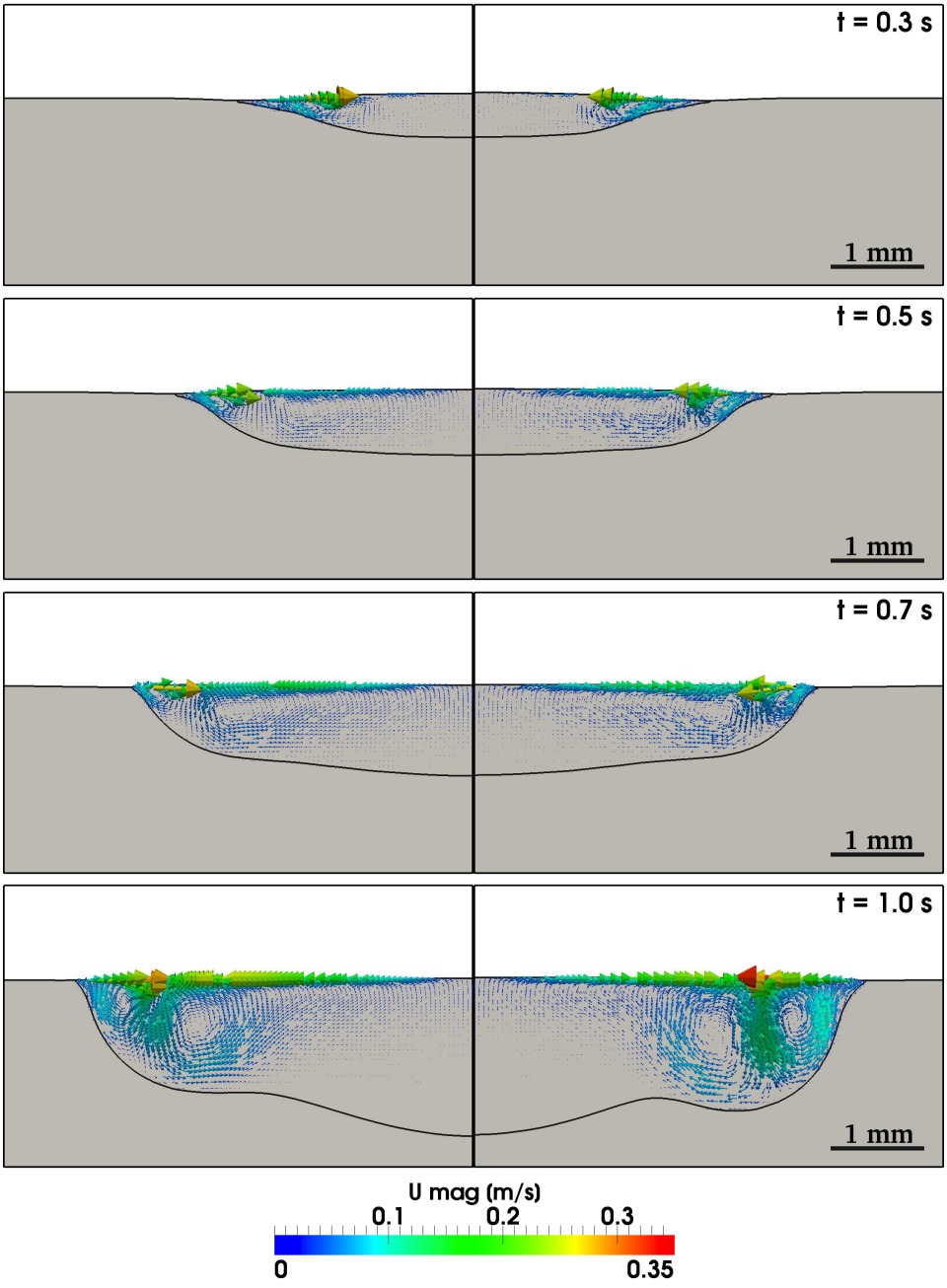

Figure 6.17. Cross sectional views of velocity fields, 2-D axisymmetric (left) and 3-D (right) free surface simulations, t = 0.3, 0.5, 0.7, 1 s.

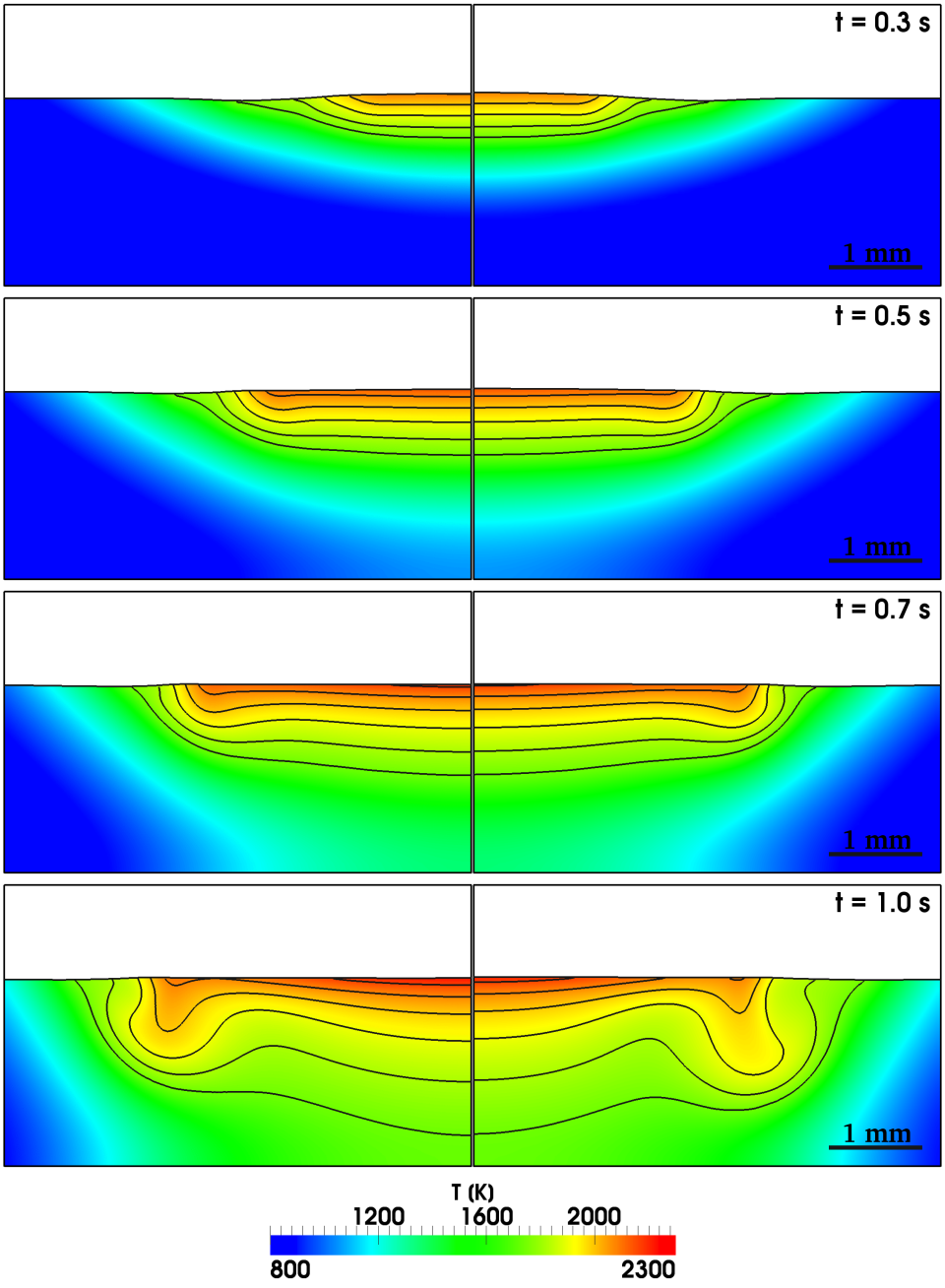

Figure 6.18. Cross sectional views of temperature fields, 2-D axisymmetric (left) and 3-D (right) free surface simulations, t = 0.3, 0.5, 0.7, 1 s. The isotherms start from 1712 K (the melting temperature) at the weld pool boundary, then continue from 1800 K onwards, with an increment of 100 K.

Figure 6.19 shows the time evolution of the radial and vertical velocity components at two monitoring points P_1 and P_2, located just 0.05 mm below the initial free surface. The radial positions of P_1 and P_2 are 1 and 3 mm, respectively. At P_1, 2-D and 3-D simulations gave an excellent agreement in terms of radial and vertical velocities. During laser heating, P_1 mainly experienced a rise in radial velocity, implying an outward flow. At around 0.2 s, however, there is a drop of velocity from 0.05 to - 0.03 m/s, which might be related to the effect of inward flow formation at the weld pool edge. This is also shown by oscillations in the vertical velocity component, possibly indicating a competition between outward and inward flows. Afterward, as the heating continues, P_1 encounters a negative $d\sigma/dT$ and the flow is outward. At P_2, located close to the weld pool edge, 2-D and 3-D simulations generally show a good agreement. Nevertheless, at the later stage of heating (t $>$ 0.9 s) the radial velocity of the 3-D simulation decreases rapidly, whereas it increases for the 2-D case. This can be explained with the aid of figure 6.17. At t = 1 s, P_2 for the 3-D simulation is located in the inward vortex at the weld pool edge, and very close to the meeting point between the two counter-rotating vortices. On the other hand, for the 2-D case, it is still located in the outward vortex. Accordingly, there is a pronounced drop of radial velocity at P_2 for the 3-D case, as shown in 6.19.

A good agreement between the 3-D, and 2-D axisymmetric results confirms that the 3-D flow is symmetrical. Accordingly, for other cases with similar welding conditions (low oxygen contents, conduction mode laser powers), performing a 2-D simulation might be sufficient, and more advantageous than 3-D simulations in terms of computational cost.

6.4.7 Effects of solidification

As already pointed out at the end of section 6.4.5, the simulated weld pool shapes at the time the laser is switched off (t = 1 s) were not in good agreement with experimentally observed post-solidification weld shapes, most likely due to the absence of solidification regime in the simulations. In this section, the simulations with varying oxygen contents in section 6.4.5 are extended into the solidification regime (t $>$ 1 s) by switching off the laser.

Laser switch-off was incorporated by deactivating the volumetric heat input at the free surface. Heat loss effects were included by (1) adding a heat sink term corresponding to radiative loss in the energy equation; and (2) imposing negative fluxes associated with radiative loss at the top and bottom boundaries of the computational domain. On both boundaries a, rather arbitrary, radiative emissivity of 0.5 was applied. The convective heat loss is already taken into account by means of flow in the gas phase above the weld pool.

Figure 6.20, 6.21, and 6.22 show the evolution of temperature and velocity fields during the solidification process of weld pools with oxygen content 20, 30, and 59 ppm, respectively. In all cases, cooling in the weld pool resulted in the shifting of $d\sigma/dT$ at the weld pool surface from negative (in the high temperature region) to positive (low temperature). As a result, the outward flows initially observed

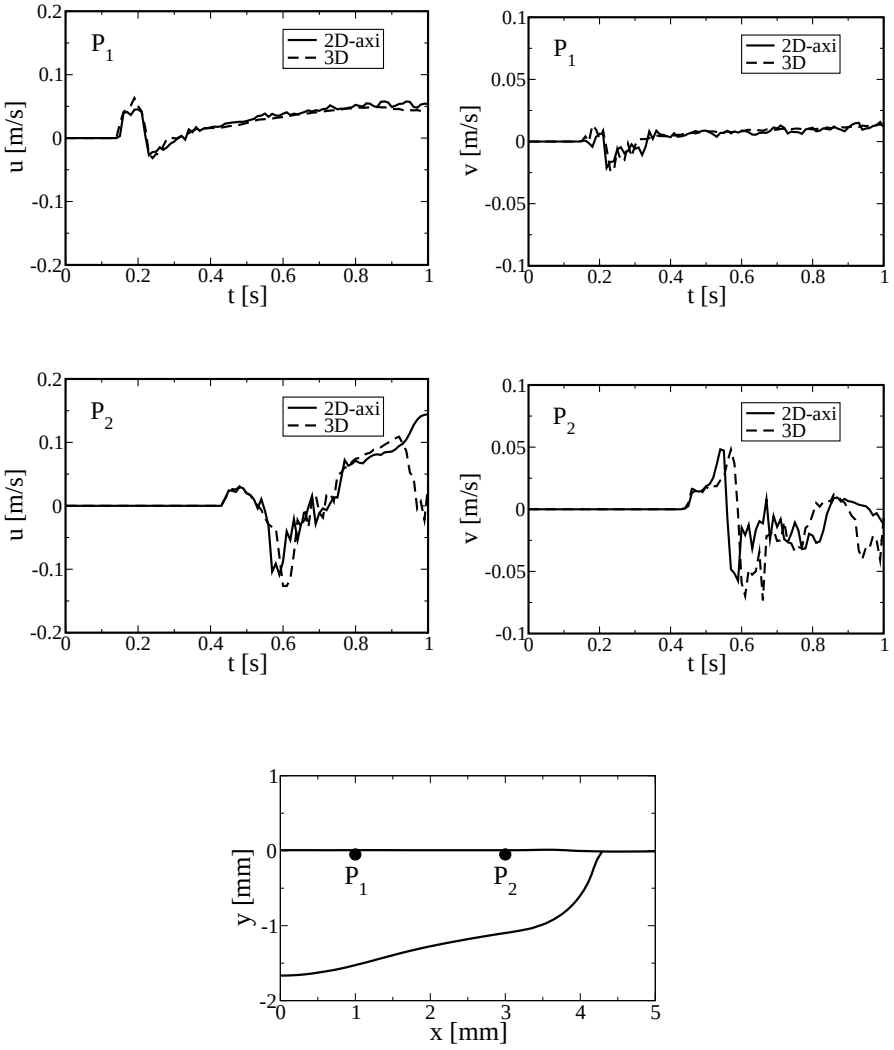

Figure 6.19. Time evolution of radial (left) and vertical (right) velocity components at monitoring points P_1 (top) and P_2 (middle). Data is extracted at 0.01 s time intervals. Illustration of the position of the monitoring points in the weld pool (bottom).

in the center region changed direction to inward. The inward flow leads to a downward motion near the center and, hence, convectively transports heat to the bottom of the weld pool. This physically results in a deeper weld pool. During this downward transport of heat, the melting front at some point in time touched the bottom boundary of the sample.

The magnitude of the inward velocities is dependent on the oxygen content, where the inward velocity increases with increasing oxygen content. At lower oxygen content, the magnitude of $d\sigma/dT$ in the low temperature regime is lower than that for high oxygen content. At 59 ppm, the strong inward flow is also assisted by the inward vortice already present at the edge before laser switch-off.

As solidification continues, more heat is taken from the weld pool and temperature gradients decrease. This causes a decay in velocities and surface deformations, leading to an almost flat surface as full solidification is eventually reached.

For all cases, the cross section of the fully solidified fusion zones at t = 2 s are shown, even though the total solidification time differs for each case. In all three cases of oxygen contents considered, full penetration of weld is reached. At this point, we can have a more proper comparison of fusion zones with the experimentally observed post-solidification weld shapes. Such a comparison is given in figure 6.23. The best agreement with experiment is found for the 20 ppm case, which is consistent again with our earlier conclusion that probably the oxygen concentration in the weld pool during welding was lower than the oxygen concentration of 59 ppm in the ambient gas. However, for 20 ppm we predict a fusion zone width that is approximately 10% too large, whereas there is a very good agreement in fusion zone width when oxygen content of 30 ppm or 59 ppm is assumed.

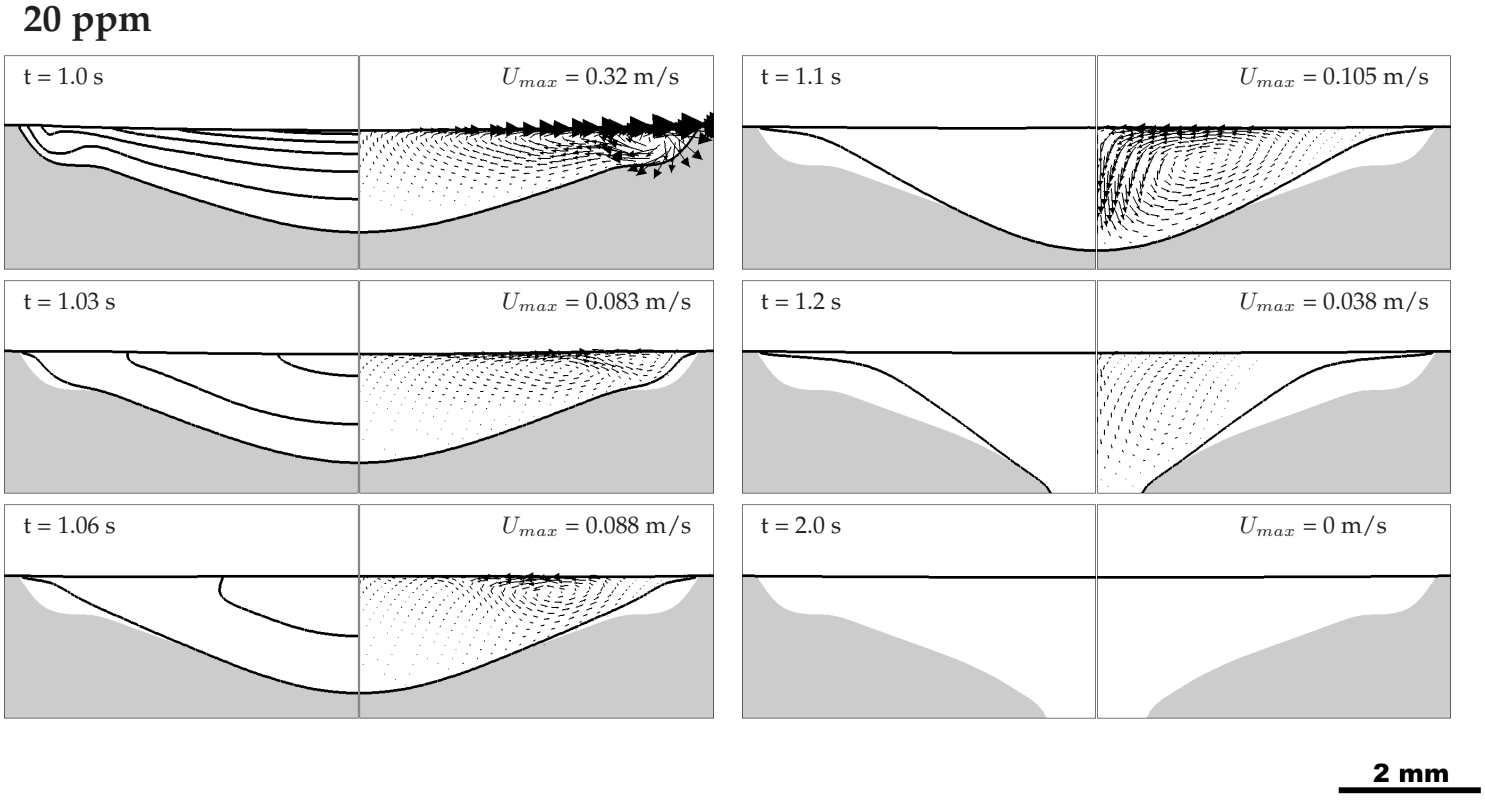

Figure 6.20. Temperature (left) and velocity (right) fields during cooling of the weld pool (20 ppm O) after laser switch-off at t = 1 s. The isotherms start from 1712 K (the melting temperature) at weld pool boundary, then continue from 1800 K onwards, with increment of 100 K.

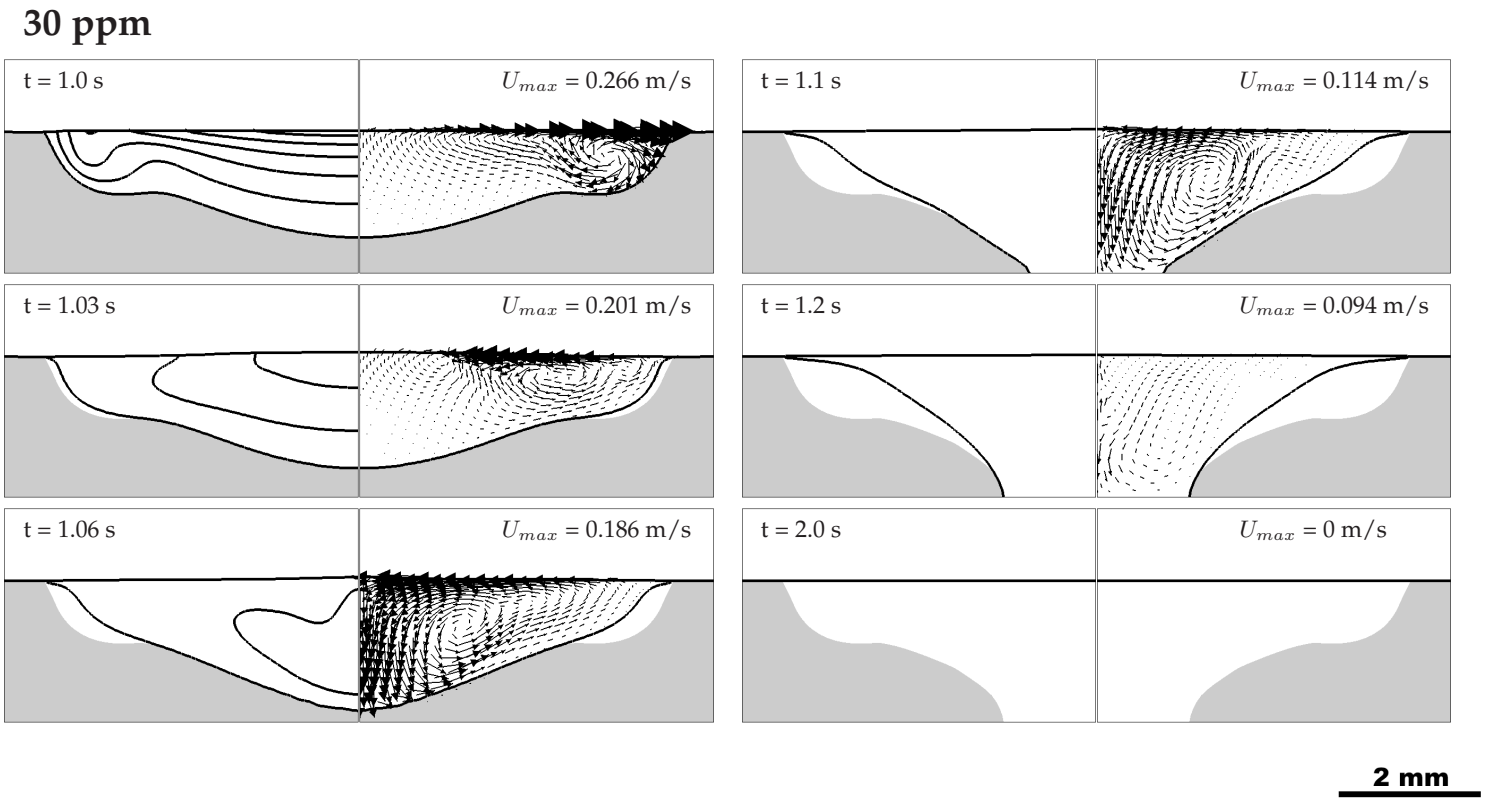

Figure 6.21. Temperature (left) and velocity (right) fields during cooling of the weld pool (30 ppm O) after laser switch-off at t = 1 s. The isotherms start from 1712 K (the melting temperature) at weld pool boundary, then continue from 1800 K onwards, with increment of 100 K.

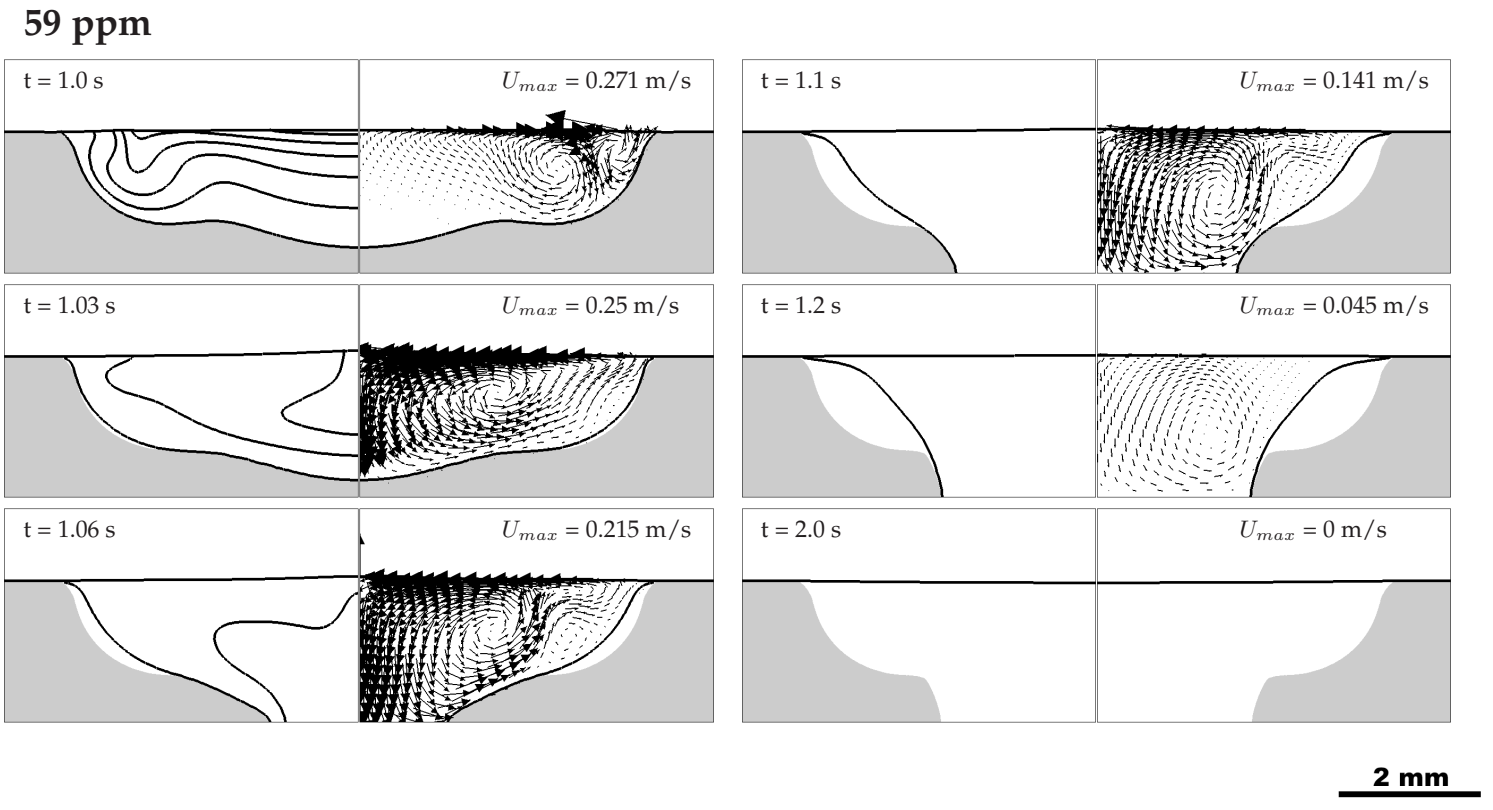

Figure 6.22. Temperature (left) and velocity (right) fields during cooling of the weld pool (59 ppm O) after laser switch-off at t = 1 s. The isotherms start from 1712 K (the melting temperature) at weld pool boundary, then continue from 1800 K onwards, with increment of 100 K.

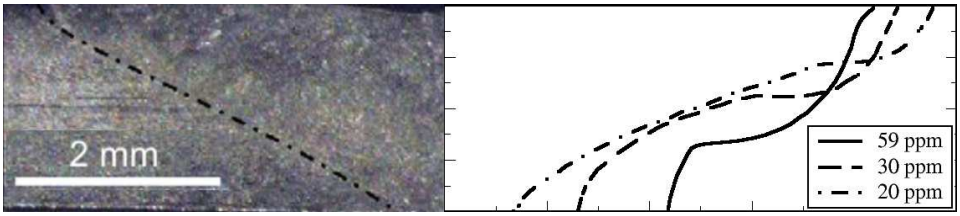

Figure 6.23. Comparison of cross sectional solidified weld shapes between experiment with 59 ppm oxygen in environment (left) and simulations with material oxygen contents of 20, 30, and 59 ppm (right).

6.4.8 Comparison with flat surface simulations

In addition to the simulations with deformable free surface, simulations with a flat surface were also carried out. This ultimately serves as the basis to study the influence of free surface deformation on the weld pool flow. Comparisons of the time evolution of the fusion zone depth, width, and aspect ratio (*i.e.* ratio of depth to width) between free surface and flat surface simulations for varying oxygen contents are given in figure 6.24. Comparisons of fusion zone shapes at laser switch-off time (t = 1 s) and after solidification are shown in figure 6.25.

A fairly good agreement between flat and free surface simulations is obtained for all considered oxygen contents until laser switch-off time. After solidification, the free surface simulations resulted in a full weld penetration for all cases. On the other hand, the flat surface simulations only gave full weld penetration for 30 and 59 ppm. The fusion zone width at the bottom boundary for these oxygen contents, however, is smaller than that obtained using free surface simulation.

In general, although differences between flat and free surface simulations are observed, these are rather small. This is not surprising, since surface deformations are very small for the studied low values of oxygen concentrations.

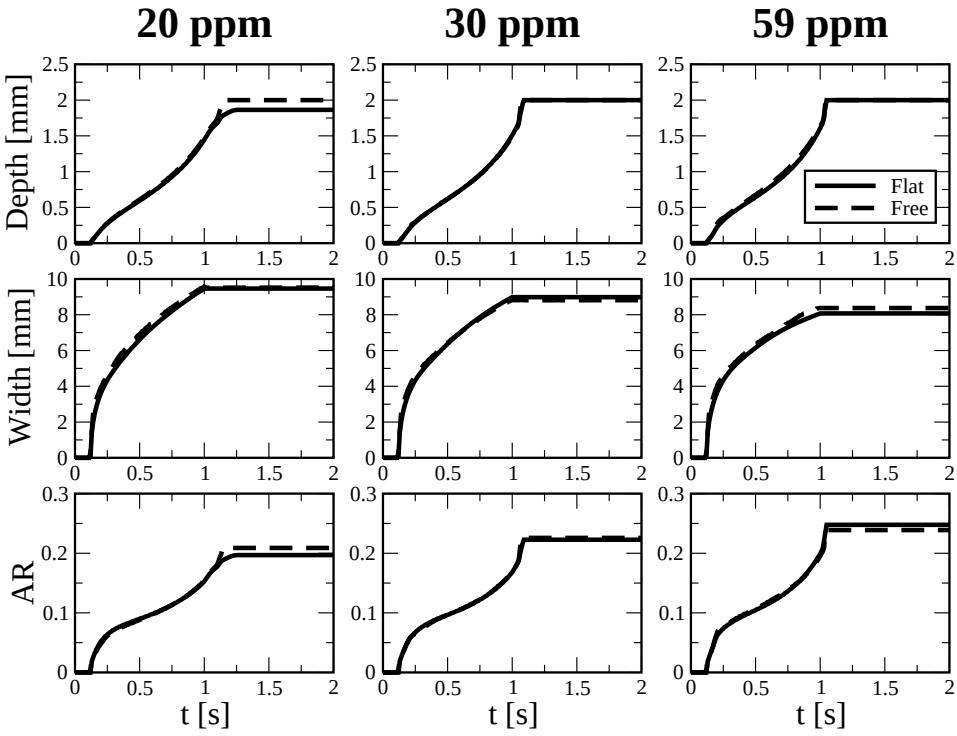

Figure 6.24. Comparisons of depth (top), width (middle), and depth-to-width aspect ratio (bottom) of fusion zone between flat and free surface simulations for 20 ppm (left), 30 ppm (center), and 59 ppm (right) cases.

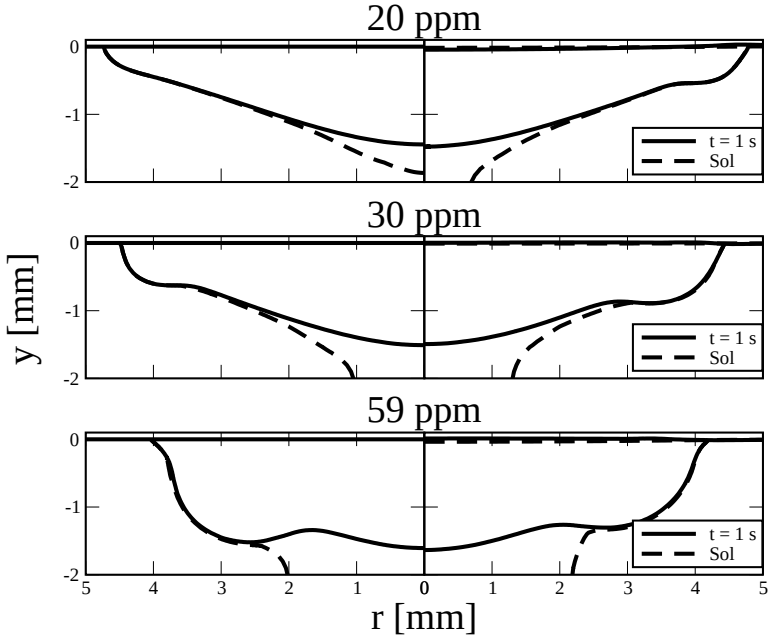

Figure 6.25. Comparisons of fusion zone shapes at laser switch-off (t = 1 s) and after solidification, between flat (left) and free (right) surface simulations for 20 ppm (top), 30 ppm (middle), and 59 ppm (bottom) cases.

6.5 Concluding remarks

In this chapter, 3-dimensional free surface simulations were performed to study the hydrodynamics in laser spot weld pools as studied experimentally in the parallel PhD project by Zhao (2011). In the experiments, welding was performed in a gas ambient of varying oxygen concentration, between 59 ppm and 20.9%. Only for the smallest, 59 ppm, ambient oxygen concentration, the welding process was in the conduction mode. Since our model is not yet suited for modeling keyhole welding, we limited our studies to the lowest ambient oxygen case.

The experimental oxygen concentration in the weld pool and at the weld pool surface, which have a very strong effect on the weld pool hydrodynamics as they determine the Marangoni forces, were not very well known. Moreover, our model does not yet account for oxygen absorption and transport in the weld pool. Therefore, we estimated the oxygen concentration in the weld pool as equal to the 59 ppm oxygen concentration in the ambient gas, and we also studied two lower concentrations of 30 and 20 ppm oxygen in the weld pool.

Only at 20 ppm oxygen concentration, the simulations showed the fully outward surface flow that was observed in the experiments, whereas the simulated surface flow was partly inward for 30 and 59 ppm oxygen. Also, the simulated post-solidification fusion zone shape was in best agreement with experimental observations for 20 ppm oxygen in the weld pool. Additionally, the predicted post-solidification fusion zone shape was in closest agreement to experiments when assuming 20 ppm oxygen in the weld pool. Both observations suggest that the experimental oxygen concentration in the weld pool, for welding in 59 ppm oxygen ambient, was probably close to 20 ppm.

At the low studied oxygen concentrations, the surface deformation is rather weak and the resulting weld pool flows are nearly axisymmetrical, as exemplified by a close agreement between 3-dimensional and 2-dimensional axisymmetric simulation results. This observation deviates from experimental observations, in which asymmetrical flows were observed. This may possibly be ascribed to small asymmetries in the experimental conditions, *e.g.* in the laser heat flux distribution. Because of the small surface deformations, small differences were observed between free and flat surface simulations. However, the free surface simulations led to somewhat deeper fusion zones. In particular, for 20 ppm oxygen the free surface simulations resulted in a full weld penetration, as observed experimentally, whereas this was not the case for the flat surface simulations.

Because of the small, but distinct, differences between flat and free surface simulations, even when surface deformation is very small, it would be interesting to see how a more pronounced surface deformation affects the weld pool flow and heat transfer. This would be the case when the Marangoni and Capillary numbers would be higher than for the low oxygen cases studied in this chapter. This can be achieved by using a higher oxygen level in the environment and a higher laser power density. Experiments by Zhao (2011) under such conditions show highly unstable, asymmetric flows with large surface deformation. Under such conditions, 3-D free surface simulations will probably lead to results that are very

different from those obtained with 2-D axisymmetric free surface simulations, or even 2-D axisymmetric flat surface simulations. Because of the high velocities reached under such conditions (experiments show velocities up to 1 m/s, *i.e.* one order of magnitude higher than observed in this chapter), such simulations would be computationally very demanding, requiring a very fine mesh and small time steps.

In order to be truly predictive, the model would have to include the absorption into, and the transport in, the weld pool of surface active elements such as oxygen.

7 CHAPTER

Closure

7.1 General conclusions

This thesis presents computational simulation studies of Marangoni driven free surface hydrodynamics in liquid steel weld pools during conduction mode laser spot welding. To this end, a CFD code within the framework of the open source code OpenFOAM has been developed, incorporating several physical aspects that are important for weld pool hydrodynamics, *viz.* melting-solidification phase change, thermocapillarity, and free surface deformation. The implementation of these individual and combined aspects was successfully tested in a number of validation cases. Moreover, when applied to laser spot conduction mode welding the code produces results that are in good agreement with simulations and experiments reported in the literature.

The main question addressed in this thesis is why, in literature, it is found that one needs to artificially increase the thermal conductivity and viscosity of the liquid steel by a significant factor, in order to get a good agreement between simulated weld pool shapes and experimentally observed post-solidification fusion zone shapes. Such a so-called enhancement factor is applied in almost all published weld pool hydrodynamics simulation studies, without proper justification other than the occasional remark that this is to account for enhanced momentum and heat transport due to flow instabilities. Not only is such an enhancement unphysical, but the proper value of the enhancement factor is also unknown *a priori* and is found to strongly depend on the welding conditions.

We have extensively evaluated the hypothesis that heat and momentum transport are enhanced by flow instabilities that can not be observed in 2-dimensional, flat surface simulations, as mostly performed in literature. To this end, we extensively compared weld pool shapes predicted by 2-D flat surface simulation, 2-D free surface simulations, and 3-D free surface simulations. The expectation was that performing 3-D free surface simulations on a fine mesh with small time steps would resolve all flow instabilities and thus eliminate the need for the use of an enhancement factor.

This was found to be partly true. Free surface simulations indeed lead to stronger flow instabilities and enhanced momentum and heat transfer compared to flat surface simulations. With increasing concentrations of surface active elements and laser power, the free surface simulations increasingly deviate from the flat surface simulations, as these high concentrations and high laser powers tend to increase surface deformation due to increased Marangoni driven velocities. As a consequence, when not using enhancement factors, weld pool shapes predicted by free surface simulations are in somewhat better agreement with experiments than flat surface simulations, but the difference with experimental fusion zone shapes is still significant. In order to get a good agreement with experimental fusion zone shapes, enhancement factors were still needed in free surface simulations, although they could be chosen smaller than for flat surface simulations.

Our studies led to a second hypothesis for the discrepancy between simulated and experimentally observed fusion zone shapes. In literature, experimentally observed post-solidification fusion zone shapes are commonly compared to simulated liquid weld pool shapes at the moment of laser switch off. Our studies, however, have shown that the fusion zone shape still changes significantly during the cool down period after laser switch-off. Including this cool down stage further increases the agreement between experimentally observed and simulated fusion zone shapes.

With the use of free surface simulations and the inclusion of the cool down stage, good agreement between simulations and experiments was obtained when applying an enhancement factor of the order of 2, as opposed to the much larger enhancement factors used in literature. So, inclusion of the free surface and cool down are important aspects in the simulation of welding hydrodynamics.

The fact that even after the inclusion of all mentioned effects good agreement with experiments is only obtained with the application of an enhancement factor indicates that important aspects of the physics are still missing. The most probable is the non-uniform distribution of surface active elements along the weld pool surface, which will lead to further enhanced Marangoni forces and heat and momentum transport. An important next step to be made is therefore to include the transport of surface active elements in the weld pool and along its surface into our computational model.

This need was also exemplified in chapter 6, in which an attempt was made to reproduce experimental results by Zhao (2011) in a parallel PhD project. Zhao studied weld pool hydrodynamics for conduction mode laser spot welding of steel in ambients of varying oxygen concentration. Larger ambient oxygen concentrations lead to larger oxygen concentrations in the weld pool due to absorption, and consequently larger Marangoni forces. The precise oxygen concentrations in the weld pool and along its surface, however, were not accurately known and cannot be predicted by our current model. Experimentally, large ambient oxygen concentration led to highly unstable weld pools with fierce surface deformations. For all but the lowest ambient oxygen concentrations, a keyhole was formed at the bottom of the welding piece. This could not be handled by our current model. Nevertheless, for conduction mode welding at low ambient oxygen concentrations of 59 ppm, very good agreement was found between our model simulations and ex-

perimental observations, without the use of enhancement factors, when assuming an oxygen concentration of 20 ppm in the weld pool. Under these conditions, the free surface deformation is small and consequently only small differences were observed between 2-D flat surface simulations and 3-D free surface simulations. The latter, however, were in marginally better agreement with experiments.

An uncertainty in transport properties could also be a factor that causes discrepancies with experimental results. This is most likely to be the case for the surface tension as a function of temperature and surface active element concentration. The currently used theoretical prediction of surface tension, which is based on a thermodynamics relation, is relevant only for a single component surfactant case. In reality, several active elements are present with different concentrations, and simultaneously influence the surface tension distributions.

7.2 Recommendations for future work

Considering the limitations and potentials of the numerical code developed in this project, some recommended future developments are recommended.

Although it has been shown that the employed VOF model is capable of dealing with a deformed free surface while minimizing parasitic currents, it has to be noted that this is achieved with a very strict mesh and time step resolution constraint. An alternative method, in order to relax such constraints, is thus necessary. For instance, in recent years investigations on combining VOF with LS (Level Set) methods have been very popular. Such combination benefits from the advantages of both methods: mass is better conserved using VOF, while a sharper interface is captured using LS.

One factor that leads to the need for a high mesh resolution in weld pool hydrodynamics simulations with a free surface is that high gradient regions occur in several parts of the weld pool, *viz.* near the free surface, melting front, and converging point between two counter-rotating flows. The position of these regions, however, dynamically changes in time. Accordingly, the use of an adaptive mesh refinement approach could help alleviate the computational burden, while maintaining or improving accuracy. If this can be addressed further, a full 3-D simulation can be carried out at a reasonably fair computational cost.

The current model still uses the assumption that surface active elements are in equilibrium state, *i.e.* their concentrations are uniform throughout the weld pool. It is thus essential to extend the model by incorporating the transport of species that allows for prediction of element redistribution in the weld pool and along its free surface. With this capability in hand, the thermocapillary problem is expanded to a thermo-soluto-capillary problem, which is more likely to be able to model realistic welding cases. Furthermore, a more in-depth model predicting the net effects of multi-component active element on surface tension is also necessary, since in reality several surface active elements are simultaneously present in the weld pool.

The main focus in this thesis has been on a conduction mode laser spot welding. In the future, other welding processes can also be simulated by expanding the open source code to incorporate all relevant ingredients, *e.g.* laser keyhole welding, arc welding, and Gas Metal Arc Welding, with fixed or moving heat source.

In terms of experimental validation, several aspects are worthy of investigation. First, measurements of boundary conditions. The boundary conditions, such as incoming heat flux, are likely to be asymmetrical. Feeding experimentally measured boundary conditions into the numerical model could help in the prediction of the weld pool hydrodynamics. Second, experimental measurement of internal flow has recently become feasible using X-ray techniques. This could help bring validation towards a one-on-one temporal comparison of internal flows. Third, a recent breakthrough in a thermal camera technology has allowed for surface temperature measurement. Validation of surface temperature distribution is thus also possible.

Bibliography

M. Aboutalebi, M. Hasan, and R. Guthrie, "Numerical study of coupled turbulent-flow and solidification for steel slab casters," *Numerical Heat Transfer, Part A - Applications*, vol. 28, no. 3, pp. 279–297, 1995.

D. Aidun and S. Martin, "Effect of sulfur and oxygen on weld penetration of high-purity austenitic stainless steels," *Journal of Materials Engineering and Performance*, vol. 6, pp. 496–502, 1997.

M. A. Alves, P. J. Oliveira, and F. T. Pinho, "A convergent and universally bounded interpolation scheme for the treatment of advection," *International Journal for Numerical Methods in Fluids*, vol. 41, no. 1, 2003.

J. J. Batteh, M. M. Chen, and J. Mazumder, "A stagnation flow analysis of the heat transfer and fluid flow phenomena in laser drilling," *Journal of Heat Transfer - Transactions of The ASME*, vol. 122, no. 4, pp. 801–807, 2000.

E. Berberović, "Investigation of free-surface flow associated with drop impact: Numerical simulations and theoretical modeling," Ph.D. dissertation, TU Darmstadt, 2010.

E. Berberović, N. P. van Hinsberg, S. Jakirlić, I. V. Roisman, and C. Tropea, "Drop impact onto a liquid layer of finite thickness: Dynamics of the cavity evolution," *Physical Review E*, vol. 79, p. 036306, 2009.

T. L. Bergman and J. R. Keller, "Combined buoyancy, surface tension flow in liquid metals," *Numerical Heat Transfer A*, vol. 13, pp. 49–63, 1988.

J. U. Brackbill, D. B. Kothe, and C. Zemach, "A continuum method for modeling surface tension," *Journal of Computational Physics*, vol. 100, pp. 335–354, 1992.

A. Brent, V. Voller, and K. Reid, "Enthalpy-porosity technique for modeling convection-diffusion phase change: Application to the melting of pure metal," *Numerical Heat Transfer B*, vol. 13, pp. 297–318, 1988.

G. Cerne, S. Petelin, and I. Tiselj, "Coupling of the interface tracking and the two-fluid models for the simulations of incompressible two-phase flow," *Journal of Computational Physics*, vol. 171, pp. 776–804, 2001.

C. Chan, J. Mazumder, and M. M. Chen, "A three-dimensional model for convection in laser melted pool," *Journal of Metals*, vol. 35, no. 12, p. 47, 1983.

C. Chan, J. Mazumder, and M. M. Chen, "A two-dimensional transient model for convection in laser melted pool," *Metallurgical Transactions A - Physical Metallurgy and Materials Science*, vol. 15, no. 12, pp. 2175–2184, 1984.

C. L. Chan, J. Mazumder, and M. M. Chen, "3-dimensional axisymmetrical model for convection in laser melted pools," *Materials Science and Technology*, vol. 3, no. 4, pp. 306–311, 1987.

D. Chatterjee and S. Chakraborty, "Large-eddy simulation of laser-induced surface-tension-driven flow," *Metallurgical and Materials Transactions B*, vol. 36, pp. 743–754, 2005, 10.1007/s11663-005-0078-0.

R. Choo, J. Szekely, and S. David, "On the calculation of the free surface temperature of gas-tungsten-arc weld pools from first principles: Part ii. modeling the weld pool and comparison with experiments," *Metallurgical and Materials Transactions B*, vol. 23, pp. 371–384, 1992.

R. T. C. Choo and J. Szekely, "Possible role of turbulence in gta weld pool behavior," *Welding Journal (Miami, Fla)*, vol. 73, no. 2, pp. 25s–31, 1994.

A. Colagrossi and M. Landrini, "Numerical simulation of interfacial flows by smoothed particle hydrodynamics," *Journal of Computational Physics*, vol. 191, pp. 448–475, 2003.

J. A. Dantzig, "Modeling liquid-solid phase changes with melt convection," *International Journal for Numerical Methods in Engineering*, vol. 28, pp. 1769–1785, 1989.

S. A. David and T. DebRoy, "Current issues and problems in welding science," *Science*, vol. 257, no. 5069, pp. 497–502, 1992.

A. De and T. DebRoy, "A smart model to estimate effective thermal conductivity and viscosity in the weld pool," *Journal of Applied Physics*, vol. 95, no. 9, pp. 5230–5240, 2004.

A. De and T. DebRoy, "Reliable calculations of heat and fluid flow during conduction mode laser welding through optimization of uncertain parameters," *Welding Journal (Miami, Fla)*, vol. 84, no. 7, pp. 101–112, 2005.

T. Debroy and S. A. David, "Physical processes in fusion welding," *Reviews of Modern Physics*, vol. 67, no. 1, pp. 85–112, 1995.

D. Delapp, G. Cook, A. Strauss, and W. Hofmeister, "Quantitative observations of surface flow and solidification on autogenous gta weld pools," in *ASM Proceedings of International Conference of Trends in Welding Research*, 2005.

M. Do-Quang, G. Amberg, and C. O. Pettersson, "Modeling of the adsorption kinetics and the convection of surfactants in a weld pool," *Journal of Heat Transfer*, vol. 130, no. 9, pp. 092–102, 2008.

A. Egelja, M. Schafer, and F. Durst, "An adaptive grid Eulerian method for the computation of free surface flows," *International Journal of Computational Fluid Dynamics*, vol. 10, no. 3, pp. 213–224, 1998.

J. H. Ferziger and M. Perić, *Computational methods for fluid dynamics*. Springer, Berlin, Germany, 1996.

M. M. Francois, J. M. Sicilian, and D. B. Kothe, "Modeling of thermocapillary forces within a volume tracking algorithm," in *Modeling of Casting, Welding and Advanced Solidification Processes XI*, C. A. Gandin and M. Bellet, Eds. The Minerals, Metals and Materials Society, 2006, pp. 935–942.

C. Gau and R. Viskanta, "Melting and solidification of a pure metal on a vertical wall," *Journal of Heat Transfer*, vol. 108, pp. 174–181, 1986.

M. Giangi, F. Stella, E. Leonardi, and G. de Vahl Davis, "A numerical study of solidification in the presence of a free surface under microgravity conditions," *Numerical Heat Transfer A*, vol. 41, no. 6, pp. 579–595, 2002.

E. J. Ha and W. S. Kim, "A study of low-power density laser welding process with evolution of free surface," *International Journal of Heat and Fluid Flow*, vol. 26, no. 4, pp. 613–621, 2005.

N. Hannoun, V. Alexiades, and T. Z. Mai, "Resolving the controversy over tin and gallium melting in a rectangular cavity heated from the side," *Computer Methods in Applied Mechanics and Engineering*, vol. 19, pp. 59–98, 2003.

A. Harten, "High resolution schemes for hyperbolic conservation laws," *Journal of Computational Physics*, vol. 49, no. 3, pp. 357 – 393, 1983.

X. He, P. Fuerschbach, and T. DebRoy, "Heat transfer and fluid flow during laser spot welding of 304 stainless steel," *Journal of Physics D: Applied Physics*, vol. 36, pp. 1388–1398, 2003.

C. R. Heiple and J. R. Roper, "Mechanism for minor element effect on gta fusion zone geometry," *Welding Journal*, vol. 61, no. 4, pp. 97s–102s, 1982.

C. R. Heiple, J. R. Rope, R. T. Stagner, and R. J. Aden, "Surface active element effects on the shape of the gta, laser, and electron beam welds," *Welding Journal (Miami, Fla)*, vol. 62, no. 3, p. 72s, 1983.

P. Henrikson, "Visualisation of weld pool surface flow during tig welding of stainless steel 316l plates," in *Mathematical Modelling of Weld Phenomena*, H. Cerjak and H. Bhadeshia, Eds., vol. 7. Institute of Materials, London SW1Y 5DB, UK, 2005, pp. 125–147.

C. Hirsch, *Numerical computation of internal and external flows. Volume 1: Fundamentals of Computational Fluid Dynamics*. Butterworth-Heinemann, 2007.

C. W. Hirt, "Thermocapillary sample problems," FlowScience, Inc., Technical Note TN47, 1998.

C. W. Hirt and B. D. Nichols, "Volume of fluid (vof) method for the dynamics of free boundaries," *Journal of Computational Physics*, vol. 39, pp. 201–225, 1981.

K. Hong, D. C. Weckman, A. B. Strong, and W. Zheng, "Modelling turbulent thermofluid flow in stationary gas tungsten arc weld pools," *Science and Technology of Welding and Joining*, vol. 7, no. 3, pp. 125–136, 2002.

K. Hong, D. C. Weckman, A. B. Strong, and W. Zheng, "Vorticity based turbulence model for thermofluids modelling of welds," *Science and Technology of Welding and Joining*, vol. 8, no. 5, pp. 313–324, 2003.

R. I. Issa, "Solution of the implicit discretized fluid flow equations by operator splitting," *Journal of Computational Physics*, vol. 62, pp. 40–65, 1986.

J. Jaidi and P. Dutta, "Three-dimensional turbulent weld pool convection in gas metal arc welding process," *Science and Technology of Welding and Joining*, vol. 9, no. 5, pp. 407–414, 2004.

H. Jasak, H. G. Weller, and A. D. Gosman, "High resolution nvd differencing scheme for arbitrarily unstructured meshes," *International Journal for Numerical Methods in Fluids*, vol. 31, pp. 431–449, 1999.

S. Katayama, N. Seto, M. Mizutani, and A. Matsunawa, "X-ray transmission insitu observation of fluid flow inside molten pool during tig arc welding of stainless steel," in *Transactions of JWRI. Special Issue: 3rd International Conference of High Temperature Capillarity 2000*, vol. 30, 2001.

S. Kou, C. Limmaneevichitr, and P. Wei, "Oscillatory marangoni flow: A fundamental study by conduction-mode laser spot welding," *Welding Journal*, vol. 90, pp. 229s–240s, 2011.

N. Kumar, S. Dash, A. K. Tyagi, and B. Raj, "Hydrodynamical phenomena in the process of laser welding and cutting," *Science and Technology of Welding and Joining*, vol. 12, no. 6, pp. 540–548, 2007.

C. Lan, M. Su, and M. Liang, "A visualization and computational study of horizontal bridgman crystal growth," *Journal of Crystal Growth*, vol. 208, no. 1-4, pp. 717–725, 2000.

J. F. Lancaster, "The physics of welding," *Physics in Technology*, vol. 15, no. 2, pp. 73–79, 1984.

B. P. Leonard, "A stable and accurate convective modelling procedure based on quadratic upstream interpolation," *Computer Methods in Applied Mechanics and Engineering*, vol. 19, pp. 59–98, 1979.

B. P. Leonard, "The ultimate conservative difference scheme applied to unsteady one-dimensional advection," *Computer Methods in Applied Mechanics and Engineering*, vol. 88, pp. 17–74, 1991.

M. Liang and C. Lan, "Three dimensional thermocapillary and buoyancy convections and interface shape in horizontal bridgman crystal growth," *Journal of Crystal Growth*, vol. 180, no. 3-4, pp. 587–596, 1997.

C. Limmaneevichitr, "Flow visualization of marangoni convection in simulated weld pools," Ph.D. dissertation, University of Wisconsin - Madison, USA, 2000.

J. Mazumder, "Overview of melt dynamics in laser processing," *Optical Engineering*, vol. 30, no. 8, pp. 1208–1219, 1991.

K. C. Mills, B. J. Keene, R. F. Brooks, and A. Shirali, "Marangoni effects in welding," *Philosophical Transactions: Mathematical, Physical and Engineering Sciences*, vol. 356, no. 1739, pp. 911–925, 1998.

S. Mishra and T. Debroy, "A heat-transfer and fluid-flow-based model to obtain a specific weld geometry using various combinations of welding variables," *Journal of Applied Physics*, vol. 98, no. 4, pp. 1–10, 2005.

M. Mizutani, S. Katayama, and A. Matsunawa, "Observation of molten metal behavior during laser irradiation: basic experiment to understand laser welding phenomena," in *First International Symposium on High-Power Laser Macroprocessing*, I. Miyamoto, K. F. Kobayashi, K. Sugioka, R. Poprawe, and H. Helvajian, Eds., vol. 4831. SPIE, 2003, pp. 208–213.

K. Mundra and T. DebRoy, "Toward understanding alloying element vaporization during laser beam welding of stainless steel," *Welding Journal*, vol. 72, no. 1, pp. 1s–9s, 1993.

S. Muzaferija, M. Peric, P. Sames, and T. Schelin, "A two-fluid navier-stokes solver to simulate water entry," in *Twenty-Second Symposium on Naval Hydrodynamics*. Commission on Physical Sciences, Mathematics, and Applications, 1998, pp. 638–651.

Y. Naito, M. Mizutani, and S. Katayama, "Effect of oxygen in ambient atmosphere on penetration characteristics in single yttrium-aluminum-garnet laser and hybrid welding," *Journal of Laser Applications*, vol. 18, no. 1, pp. 21–27, 2006.

OpenCFD, *OpenFOAM, The Open Source CFD Toolbox, User's Guide*, 2008.

G. M. Oreper and J. Szekely, "Heat- and fluid-flow phenomena in weld pools," *Journal of Fluid Mechanics*, vol. 147, pp. 53–79, 1984.

S. Osher and R. Fedkiw, *Level Set Methods and Dynamic Implicit Surfaces*. Springer, 2002.

S. V. Patankar, *Numerical heat transfer and fluid flow*. Hemisphere, New York, USA, 1980.

S. V. Patankar and D. B. Spalding, "A calculation procedure for heat, mass and momentum transfer in three-dimensional parabolic flows," *International Journal of Heat and Mass Transfer*, vol. 15, pp. 1787–1806, 1972.

A. Paul and T. DebRoy, "Free surface flow and heat transfer in conduction mode laser welding," *Metallurgical and Materials Transactions B*, vol. 19, pp. 851–858, 1988.

V. Pavlyk and U. Dilthey, "Simulation of weld solidification microstructure and its coupling to the macroscopic heat and fluid flow modelling," *Modelling and Simulation in Materials Science and Engineering*, vol. 12, no. 1, p. S33, 2004.

W. Pitscheneder, T. DebRoy, K. Mundra, and R. Ebner, "Role of sulfur and processing variables on the temporal evolution of weld pool geometry during multikilowatt laser beam welding of steels," *Supplement to the Welding Journal*, p. 71s, 1996.

M. Rao and W. Shyy, "Moving boundary computations of the float-zone process," *International Journal for Numerical Methods in Engineering*, vol. 40, no. 7, pp. 1231–1261, 1997.

B. Ribic, R. Rai, and T. DebRoy, "Numerical simulation of heat transfer and fluid flow in gta/laser hybrid welding," *Science and Technology of Welding and Joining*, vol. 13, no. 8, pp. 683–693, 2008.

H. Rusche, "Computational fluid dynamics of dispersed two-phase flows at high phase fractions," Ph.D. dissertation, Imperial College of Science, Technology, and Medicine, London, 2002.

Y. Saad, *Iterative Methods for Sparse Linear Systems*, 2nd ed. Society for Industrial and Applied Mathematics, 2003.

P. Sahoo, T. DebRoy, and M. McNallan, "Surface tension of binary metal - surface active solute systems under conditions relevant to welding metallurgy," *Metallurgical Transactions B*, vol. 19, pp. 483–491, 1988.

G. P. Sasmal and J. I. Hochstein, "Marangoni convection with a curved and deforming free surface in a cavity," *Journal of Fluid Engineering*, vol. 116, pp. 577–582, 1994.

A. K. Sen and S. H. Davis, "Steady thermocapillary flows in two-dimensional slots," *Journal of Fluid Mechanics*, vol. 121, pp. 163–186, 1982.

F. Stella and M. Giangi, "Melting of a pure metal on a vertical wall: numerical simulation," *Numerical Heat Transfer A*, vol. 138, pp. 193–208, 2000.

L. Tan, S. Leong, E. Leonardi, and T. Barber, "A numerical study of solid-liquid phase change with marangoni effects using a multiphase approach," *Progress in Computational Fluid Dynamics*, vol. 6, no. 6, pp. 304–313, 2006.

M. Thompson and J. Szekely, "The transient behavior of weld pools with a deformed free surface," *International Journal of Heat and Mass Transfer*, vol. 32, no. 6, pp. 1007 – 1019, 1989.

A. Traidia, F. Roger, and E. Guyot, "Optimal parameters for pulsed gas tungsten arc welding in partially and fully penetrated weld pools," *International Journal of Thermal Sciences*, vol. 49, no. 7, pp. 1197 – 1208, 2010.

G. Tryggvason, B. Bunner, A. Esmaeeli, D. Juric, N. Al-Rawahi, W. Tauber, J. Han, S. Nas, and Y. J. Jan, "A front-tracking method for the computations of multiphase flow," *Journal of Computational Physics*, vol. 169, no. 2, pp. 708–759, 2001.

M. C. Tsai and S. Kou, "Marangoni convection in weld pools with a free surface," *International Journal for Numerical Methods in Fluids*, vol. 9, no. 12, pp. 1503–1516, 1989.

O. Ubbink and R. I. Issa, "Method for capturing sharp fluid interfaces on arbitrary meshes," *Journal of Computational Physics*, vol. 153, pp. 26–50, 1999.

V. R. Voller and C. R. Swaminathan, "General source-based method for solidification phase change," *Numerical Heat Transfer Part B Fundamentals*, vol. 19, no. 2, pp. 175–189, 1991.

V. R. Voller, C. R. Swaminathan, and B. G. Thomas, "Fixed grid techniques for phase change problems: A review," *International Journal for Numerical Methods in Engineering*, vol. 30, no. 4, pp. 875–898, 1990.

T. Waclawczyk and T. Koronowicz, "Modeling of the wave breaking with CICSAM and HRIC high-resolution schemes," in *European Conference on Computational Fluid Dynamics*, P. Wesseling, E. Oñate, and J. Périaux, Eds. TU Delft, The Netherlands, 2006, pp. 1–19.

Y. Wang and K. Hutter, "Comparisons of numerical methods with respect to convectively dominated problems," *International Journal for Numerical Methods in Fluids*, vol. 37, pp. 721–745, 2001.

Y. Wang, Q. Shi, and H. Tsai, "Modeling of the effects of surface-active elements on flow patterns and weld penetration," *Metallurgical and Materials Transactions B*, vol. 32, pp. 145–161, 2001.

P. S. Wei, C. N. Ting, J. S. Yeh, T. Debroy, F. K. Chung, and G. H. Yan, "Origin of wavy weld boundary," *Journal of Applied Physics*, vol. 105, no. 5, 2009.

H. G. Weller, G. Tabor, H. Jasak, and C. Fureby, "A tensorial approach to computational continuum mechanics using object-oriented techniques," *Computer in Physics*, vol. 12, no. 6, pp. 620–631, 1998.

C. Winkler and G. Amberg, "Multicomponent surfactant mass transfer in gta-welding," *Progress in Computational Fluid Dynamics*, vol. 5, no. 3-5, pp. 190–206, 2005.

C. Winkler, G. Amberg, H. Inoue, T. Koseki, and M. Fuji, "Effect of surfactant redistribution on weld pool shape during gas tungsten arc welding," *Science and Technology of Welding and Joining*, vol. 5, no. 1, pp. 8–20, 2000.

T. Zacharia, S. A. David, J. M. Vitek, and T. Debroy, "Modeling of interfacial phenomena in welding," *Metallurgical Transactions B*, vol. 21, no. 3, pp. 600–603, 1990.

W. Zhang, G. G. Roy, J. Elmer, and T. DebRoy, "Modeling of heat transfer and fluid flow during gas tungsten arc spot welding of low carbon steel," *Journal of Applied Physics*, vol. 93, no. 5, pp. 3022–3033, 2003.

C. Zhao, "Measurements of fluid flow in weld pools," Ph.D. dissertation, Delft University of Technology, 2011.

C. X. Zhao, V. van Steijn, I. M. Richardson, C. R. Kleijn, S. Kenjereš, and Z. S. Saldi, "Unsteady interfacial phenomena during inward weld pool flow with an active surface oxide," *Science and Technology of Welding and Joining*, vol. 14, no. 2, pp. 132–140, 2009.

C. Zhao, C. Kwakernaak, Y. Pan, I. Richardson, Z. Saldi, S. Kenjeres, and C. Kleijn, "The effect of oxygen on transitional marangoni flow in laser spot welding," *Acta Materialia*, vol. 58, no. 19, pp. 6345–6357, 2010.

J. Zhou and H. L. Tsai, "Modeling of transport phenomena in hybrid laser-mig keyhole welding," *International Journal of Heat and Mass Transfer*, vol. 51, no. 17-18, pp. 4353–4366, 2008.

J. Zhou and H. L. Tsai, "Investigation of mixing and diffusion processes in hybrid spot laser-mig keyhole welding," *Journal of Physics D: Applied Physics*, vol. 42, no. 9, 2009.

A APPENDIX

Transport properties and process parameters in validation test cases

A.1 Melting of a pure metal

Properties & parameters	Values	Units
Density, ρ	6093	$\mathrm{kg/m^3}$
Thermal conductivity, k	32	$\mathrm{W/(m \cdot K)}$
Specific heat, C_p	381.5	$\mathrm{J/(kg \cdot K)}$
Latent enthalpy of fusion, L	80160	$\mathrm{J/kg}$
Thermal expansion coefficient, β	1.2×10^{-4}	$\mathrm{K^{-1}}$
Dynamic viscosity, μ	1.81×10^{-3}	$\mathrm{kg/(m \cdot s)}$
Gravity acceleration, g	9.81	$\mathrm{m/s^2}$
Melting temperature, T_m	302.78	K
Hot wall temperature, T_h	311	K
Cold wall temperature, T_c	301.3	K
Cavity height, H	0.0635	m
Cavity width, W	0.0889	m
Aspect ratio, $AR = H/W$	0.714	-

Table A.1. Physical properties of gallium and parameters (Brent et al. (1988)).

A.2 Marangoni convection in a cavity

Properties & parameters	**Values**	**Units**
Density, ρ	2385	$\mathrm{kg/m^3}$
Thermal conductivity, k	94.03	$\mathrm{W/(m \cdot K)}$
Specific heat, C_p	1080	$\mathrm{J/(kg \cdot K)}$
Thermal expansion coefficient, β	1.17×10^{-4}	$\mathrm{K^{-1}}$
Dynamic viscosity, μ	1.3×10^{-3}	$\mathrm{kg/(m \cdot s)}$
Cavity width, W	20	mm
Cavity height, H	20	mm
$\Delta T = T_h - T_c$	100	K

Table A.2. Material properties of liquid aluminum (evaluated at 660 ^0C) (Bergman and Keller (1988)).

A.3 Free surface Marangoni-driven flows with phase change

Properties / Parameters / Dimensionless numbers	Values	Units
Argon properties		
Density, ρ	1.6337	kg/m^3
Thermal conductivity, k	0.0177	$W/(m \cdot K)$
Specific heat, C_p	520	$J/(kg \cdot K)$
Dynamic viscosity, μ	2.26×10^{-5}	$kg/(m \cdot s)$
Bismuth properties		
Density, ρ	9780	kg/m^3
Thermal conductivity, k	10.35	$W/(m \cdot K)$
Specific heat, C_p	123	$J/(kg \cdot K)$
Latent enthalpy of fusion, L	44600	J/kg
Thermal expansion coefficient, β	1.34×10^{-5}	K^{-1}
Dynamic viscosity, μ	1.6×10^{-3}	$kg/(m \cdot s)$
Melting temperature, T_m	544.55	K
Parameters		
Hot wall temperature, T_h	552.55	K
Cold wall temperature, T_c	540.55	K
Gravity acceleration, g	4.415×10^{-4}	m/s^2
Container height, H	5	mm
Container width, W	15	mm
Melting front position, x_m	10	mm
Initial melt depth, H_m	4	mm
Initial argon gap, H_{Ar}	1	mm
Dimensionless numbers		
Prandtl, Pr	0.019	-
Marangoni, Mg	244	-
Rayleigh, Ra	0.031	-
Capillary, Ca	0.0022	-
Stefan, Ste	0.033	-
Bond, Bo	0.000188	-

Table A.3. Material properties and parameters for free surface Marangoni-driven flows with phase change test case (Tan et al. (2006)).

Summary

Marangoni driven free surface flows in liquid weld pools

Zaki S. Saldi

Extending the weldability of novel materials, and improving the weld quality by tailoring weld microstructures are key factors to obtain the welding techniques demanded in the modern manufacturing industries. This can be done, for example, by feeding chemical elements from a consumable wire into the weld pool during welding. Such elements include *e.g.* zirconium and scandium as grain refiners, or calcium as surface active elements. The resulting post-solidification weld microstructures are highly influenced by the flow of the liquid metal in the weld pool during welding, the so-called weld pool hydrodynamics. This influences the heat transfer from the heat sources to the heat affected zone around the weld, as well as the mixing of chemical components in the weld pool. Weld pool hydrodynamics is known to be primarily driven by Marangoni forces acting at the free liquid surface, *i.e.* by tangential gradients in surface tension along the liquid surface due to pronounced lateral gradients in temperature and surface active element concentration. The complex interaction between Marangoni driven weld pool hydrodynamics, heat transfer, and the mixing of surface active elements is still largely uncomprehended.

In literature, numerical simulations by means of Computational Fluid Dynamics (CFD), in conjunction with experiments, have been of great importance in studying the fluid flow, heat, and mass transfer in weld pools. Whereas experimental studies are hampered by the small dimensions, opacity, and high temperatures in the weld pool, CFD allows for a detailed, 3-dimensional and spatially resolved analysis of the time-dependent flow and heat and mass transfer, both at the free surface and inside the weld pool.

The main objectives of the research reported in this thesis are:

1. To develop a numerical model implemented in a Computational Fluid Dynamics (CFD) code that allows for the prediction of the flow field and heat transfer in steel weld pools subjected to a laser heat source during conduction mode laser spot welding.

2. To answer the question: which level of sophistication (*e.g.* 2-dimensional or 3-dimensional, with a flat or deformable liquid surface, with or without inclusion of the solidification phase) is needed to accurately model the physics of weld formation?

3. To use the developed code to study the physics of the weld pool flow. In particular, we seek to answer the following questions: (a) How does the Marangoni driven flow in the weld pool influence the shape of the final fusion zone?; (b) How does the Marangoni driven flow in the weld pool depend on the amount of heat supplied to the weld, and on the concentration of surface active elements in the weld pool?; and (c) What is the role of free surface deformation and flow instabilities on the heat transfer and on the shape of the final fusion zone?

A CFD model for weld pool hydrodynamics was developed in the open-source CFD toolbox OpenFOAM, accounting for important features of weld pool flows such as heat absorption at the surface, free surface deformation, Marangoni convection, melting and solidification phase change. Free surface deformation is modeled using the well-known Volume of Fluid (VOF) interface capturing method. Marangoni and surface tension effects are modeled using the Continuous Surface Force (CSF) method. The model was successfully validated on a number of generic test cases and on a test case of conduction-mode laser spot welding of stainless steel.

Moreover, the 3-D free surface model phase is used to study the effect of ambient oxygen on weld pool flows. Using an estimation for the absorbed oxygen level, we predicted quite well the outward flow and weld pool shape as observed experimentally. However, our estimation of the absorbed oxygen and the use of the 3-D free surface model are still limited for cases with a conduction mode laser spot source and a low ambient oxygen level, hence not too high Marangoni and Capillary numbers. Under these conditions, the free surface deformation is small and thus only small differences were observed between 2-D flat surface simulations, 2-D free surface simulations, and 3-D free surface simulations, although the latter were in slightly better agreement with experimental results, in terms of fusion zone shapes. Higher Marangoni and Capillary numbers, hence a more violent free surface deformations, would require very fine mesh and computational time steps so as to avoid parasitic currents in the vicinity of the free surface for accurate surface forces calculation.

It has been observed experimentally that weld pool flows can be highly unsteady, three-dimensional, turbulent-like, and involve free surface instabilities. In many simulation studies in literature, however, these aspects were neglected by the use of a 2-D axisymmetric coordinate system along with the assumption of a flat, non-deformable weld pool surface. With these simplifications, it was found to be necessary to artificially increase the thermal conductivity and viscosity of the liquid steel by about one order of magnitude. This is a very rudimentary way to represent the enhancement of heat and momentum due to the instabilities of the flow and free surface.

In this thesis, simulations have been done using 2-D axisymmetric flat surface, 2-D axisymmetric free surface, and 3-D free surface models, each by excluding and including the solidification phase after the switch-off of the laser source. It has been found that, in the absence of an artificial enhancement factor for the thermal conductivity and viscosity, flow instabilities and surface deformations can be predicted by the 2-D axisymmetric free surface model, leading to a deeper weld fusion zone that agrees better with experimental results, compared to the 2-D axisymmetric flat surface model. However, the discrepancy with experimental fusion zone depth is still significant. By also incorporating the solidification phase in the simulation, this discrepancy can be reduced, owing to the presence of inward flows that convectively transport heat downwards, when the laser is switched off.

Full 3-D free surface simulations were performed for cases with relatively small free surface deformation. Under these conditions, 3-D simulations led to 2-D symmetric flows and temperature distributions, and consequently the differences between 2-D free surface and 3-D free surface simulations were very small. This might, however, not be the case for welding conditions with a much more violent surface deformation, *i.e.* for high heat inputs and high concentrations of surface active elements.

With the use of a free surface model and including solidification in the cool down stage, a much lower enhancement factor than what is used in literature can be used to obtain a good agreement between simulated and experimental fusion zone shapes. Together, however, these two improvements in the model description do not lead to a sufficiently profound effect on the deepening of the weld pool to match experimental results. This might be due to the fact that the relation between element concentration and surface tension adopted in this thesis is still based on an equilibrium model, *i.e.* uniform element concentrations throughout the weld pool. A non-uniform distribution of surface active elements may lead to much more pronounced flow instabilities and deeper weld pools. It is therefore necessary that the transport of surface active elements is incorporated in future extensions of the model, so as to allow for the prediction of local element concentrations along the free surface.

When looking at the interaction between welding conditions, the induced Marangoni driven flow, and the final weld pool shapes, it is found that the welding conditions (heat input and concentration of surface active elements in the weld pool) have a strong influence on the magnitude and direction of the Marangoni flow. If the Marangoni driven velocity is sufficiently high, its direction has a large impact on the final post-solidification fusion zone shape. In general, an outward flow along the surface results in a shallow, but wide weld, whereas an inward flow results in a narrow, but deep weld pool.

The magnitude and direction of the Marangoni flow are determined by the magnitude of the lateral temperature gradients, and by magnitude and sign the temperature gradient of the surface tension. With increasing absorbed energy, the surface temperature gradient is increased, leading to an increased Marangoni number and higher weld pool velocities. Similarly, increasing the concentrations of surface active elements results in a higher magnitude of the temperature gradi-

ent of surface tension, which also lead to an increased Marangoni number and higher weld pool velocities. At a low heat inputs and low concentrations of surface active elements, the surface tension decreases with increasing temperature throughout the weld pool surface, and the surface tension is therefore lower in the weld pool center than at the edge. Consequently, the surface Marangoni flow occurs from the center to the edge (outward flow). Increasing the concentration of surface active elements or the heat input may result in a condition where the surface tension increases with temperature in the hot zones of the weld pool surface, and decreases with temperature in the colder zones. In this case, the surface tension has a maximum somewhere in the middle between the weld pool centre and the weld pool edge, and two counter-rotating Marangoni flows coexist, where in the center an outward flow is present, and at the edge an inward flow occurs. If the element concentration is so high that the surface tension increases with temperature throughout the weld pool surface, the surface tension has its maximum at the weld pool edge and a fully inward flow occurs. An interesting aspect is also observed in the solidification stage, where the absorbed energy is abruptly decreased, leading to a decrease in surface temperature and its gradients. In the case of low surface active element concentrations, this causes the Marangoni flow to flip direction. In the case of high surface active element concentrations, the Marangoni flow remains in the same direction after the heat source has been switched off, but its velocity magnitude is increased. As a result, the weld pool gets deeper (most notably for high concentration case) after the heat source has been switched off.

Free surface deformations and instabilities are found to play important roles in weld pool hydrodynamics. When these aspects are considered, the maximum weld pool velocities are lower than when a flat surface assumption is used, indicating an enhanced momentum transfer and decreased temperature gradients due to enhanced heat transfer. This, however, has different implications for different welding conditions. For a low concentration of surface active elements, the weld pool flow is outward. An enhanced convective heat transfer due to flow instabilities leads to a decrease in maximum temperature in the center, compared to the flat surface case, as more heat is transported to the edge. On the other hand, for a high concentration case, the weld pool flow is inward. Thus, an enhanced convective heat transfer due to flow instabilities leads to an increase in maximum temperature in the center, compared to the flat surface case, as more heat is transported to the center. The deviation from the flat surface simulations increases with increasing laser power and active element concentrations, as these increase surface deformation due to increased Marangoni driven velocities. Consequently, the final fusion zone shapes are also different from those predicted by the flat surface model.

Based on the findings in this thesis, it is concluded that free surface deformations and instabilities have a strong impact on the fluid flow and heat transfer in weld pools during conduction mode laser spot welding, and should therefore be accounted for in weld pool simulations. With increasing the surface active element concentration and laser power, the weld pool flow becomes highly unstable and can no longer be accurately modeled with a flat surface assumption. More accu-

rate predictions of weld pool physics can be made if the free surface, solidification stage, and three-dimensionality are taken into account. This reduces, but not eliminates, the need for the use of unphysical parameter fittings. A further necessary improvement of the models is to account for non-uniform distributions of surface active elements through the inclusion of the transport of such species. This is likely to further improve the prediction of Marangoni driven flows and flow instabilities.

Samenvatting

Door Marangonikrachten gedreven vrije oppervlaktestromingen in lasbaden

Zaki S. Saldi

Voor het ontwikkelen van de nieuwe lastechnieken die nodig zijn in de tegenwoordige vervaardigingsindustrie zijn verbetering van de lasbaarheid van nieuwe materialen, en verbetering van de laskwaliteit door verbeterde controle van de microstructuren in de las, essentieel. Dit kan bijvoorbeeld bereikt worden door het toevoegen van chemische elementen aan het lasbad tijdens het lassen. Dergelijke elementen zijn bijvoorbeeld zirkonium en scandium als korrelverfijners, of calcium als oppervlakte actieve stof. De resulterende las-microstructuren na stolling worden sterk benvloed door de stroming van het vloeibare metaal in het lasbad tijdens het lassen. Deze lasbad-hydrodynamica benvloedt de warmteoverdracht van de warmtebronnen naar de zogenaamde heat affected zone rond de las, alsmede het mengen van chemische componenten in het lasbad. De stroming in het lasbad is voornamelijk het gevolg van Marangoni krachten op het vrije vloeistofoppervlak ten gevolge van tangentile gradinten in oppervlaktespanning langs het vloeistofoppervlak. Deze worden veroorzaakt door grote tangentile gradiënten in de temperatuur en in de concentratie van oppervlakte actieve elementen. De complexe interactie tussen Marangoni-stromingen in een lasbad, warmteoverdracht, en het mengen van oppervlakte-actieve elementen is nog grotendeels onbegrepen.

In de literatuur zijn numerieke simulaties met behulp van Computational Fluid Dynamics (CFD), in samenhang met experimenten, van groot belang gebleken bij het bestuderen van de stroming, warmte- en stofoverdracht in lasbaden. Maar daar waar experimentele studies worden belemmerd door de kleine afmetingen, de opaciteit en de hoge temperaturen in het lasbad, kunnen CFD berekeningen een gedetailleerde, 3-dimensionaal en ruimtelijk opgelost beeld van de tijdsafhankelijke stroming, warmte-en stofoverdracht geven, zowel op het vrije oppervlak als binnen in het lasbad.

De belangrijkste doelstellingen van het onderzoek beschreven in dit proefschrift zijn:

1. Het ontwikkelen van een numeriek model, gemplementeerd in een Computational Fluid Dynamics (CFD) code, voor het voorspellen van de stroming en warmteoverdracht in staal lasbaden tijdens puntlassen in geleidingsmode met behulp van een laser.

2. Het beantwoorden van de vraag welke mate van detail nodig is in het model (bijv. 2-dimensionaal of 3-dimensionaal, met een plat of een vrij vervormbaar vloeistofoppervlak, met of zonder rekening te houden van de stollingsfase) om de fysica van lasvorming nauwkeurig te beschrijven.

3. Om de ontwikkelde code te gebruiken om de fysica van de stroming in het lasbad te bestuderen. In het bijzonder willen we de volgende vragen beantwoorden: (a) Hoe benvloedt de Marangoni-stroming in het lasbad de vorm van de uiteindelijke las?; (b) Hoe hangt de Marangoni-stroming in het lasbad af van de hoeveelheid toegevoerde warmte en van de concentratie oppervlakte-actieve elementen in het lasbad?; en (c) Wat is de rol van de vervorming van het vrije vloeistofoppervlak en de stromingsinstabiliteiten op de warmteoverdracht en de vorm van de uiteindelijke las?

Een CFD-model voor de hydrodynamica in een lasbad, waarin belangrijke fysische aspecten zoals warmteopname aan het oppervlak, vervorming van het vrije vloeistofoppervlak, Marangoni-stroming, smelten en stollen zijn gemodelleerd, is ontwikkeld in de open-source CFD toolbox OpenFOAM. De vervorming van het vrije oppervlak is gemodelleerd met behulp van de Volume of Fluid (VOF) methode. Marangoni- en oppervlaktespanningseffecten worden gemodelleerd met behulp van de Continuous Surface Force (CSF) methode. Het model werd met succes gevalideerd aan de hand van een aantal generieke testcases, evenals een testcasus waarin laser puntlassen van roestvrij staal in geleidingsmode van werd bestudeerd.

Bovendien wordt het 3-D vrije oppervlakte model gebruikt om het effect ongevingszuurstof op de stroming in het lasbad te bestuderen. De experimenteel waargenomen naar buiten gerichte oppervlaktestroming kon goed worden voorspeld op basis van een schatting voor het geabsorbeerde zuurstofgehalte. Echter, ons 3-D vrije oppervlakte model is thans nog slechts toepasbaar voor laser puntlassen in geleidingsmode bij lage zuurstofconcentraties, dus niet te hoge Marangoni- en Capillairgetallen. Onder deze omstandigheden is de vervorming van het vrije oppervlak gering en worden dientengevolge slechts kleine verschillen waargenomen tussen 2-D simulaties op basis van een onvervormbaar vloeistofoppervlak, en 3-D simulaties op basis van een vrij, vervormbaar vloeistofoppervlak. Toch was de voorspelde vorm van de las in deze laatste iets beter in overeenstemming met experimentele resultaten. Hogere Marangoni- en Capillairgetallen, leidend tot sterkere vervormingen van het vrije vloeistofoppervlak, zouden een zeer fijn rekenrooster en kleine tijdstappen noodzakelijk maken om de oppervlaktekrachten nauwkeurig te berekenen en parasitaire stromingen in de nabijheid van het vrije oppervlak te vermijden.

Experimentele waarnemingen laten zien dat de stroming in het lasbad zeer onstabiel, driedimensionaal, (quasi)turbulent kan zijn, met grote instabiliteiten in het vrije oppervlak. In veel simulatiestudies in de literatuur worden deze aspecten echter verwaarloosd en wordt gebruik gemaakt van een 2-D axisymmetrisch cordinatenstelsel en de veronderstelling dat het vrije oppervlak plat en niet-vervormbaar is. Met deze vereenvoudigingen bleek het noodzakelijk te zijn om de thermische geleidbaarheid en de viscositeit van het vloeibare staal kunstmatig

met ongeveer een orde van grootte te verhogen, teneinde resultaten te verkrijgen die overeenstemmen met de experimentele werkelijkheid voor wat betreft de vorm en afmetingen van de las. Deze verhoging van de viscositeit en de thermische geleidbaarheid is een rudimentaire manier om de verhoging warmte- en momentumtranssport ten gevolge van de stromings- en oppervlakte-instabiliteiten in rekening te brengen.

In dit proefschrift zijn simulaties uitgevoerd op basis van een 2-D axisymmetrische geometrie en een plat vloeistofoppervlak, een 2-D axisymmetrische geometrie met een vrij vervormbaar oppervlak, en een 3-D geometrie met een vrij vervormbaar oppervlak. Voor elk van deze simulatiemethodes is bovendien gekeken wat de invloed is van het meenemen of verwaarlozen van de stollingsfase na uitschakeling van de warmtebron. Hieruit bleek dat, in afwezigheid van een kunstmatige verhoging van de thermische geleidbaarheid en viscositeit, stromingsinstabiliteiten en oppervlaktevervormingen voorspeld worden door modellen gebaseerd op een 2-D axisymmetrische geometrie met een vrij oppervlak. In vergelijking met simulaties met een plat oppervlak leidt dit tot een dieper lasbad, dat beter in overeenstemming is met experimentele resultaten. Echter, het verschil met de experimenteel waargenomen diepte van het lasbad is nog steeds aanzienlijk. Door ook de stollingsfase mee te nemen in de simulatie, kan dit verschil worden verkleind. Dit is het gevolg van het feit dat tijdens de stollingsfase, na uitschakeling van de laser, een naar het centrum gerichte oppervlaktestroming optreedt, waardoor warmte door het centrum naar beneden getransporteerd wordt. Volledige 3-D vrij oppervlak simulaties werden uitgevoerd voor gevallen met relatief kleine vervormingen van het vrije oppervlak. Onder deze omstandigheden leiden de 3-D simulaties tot vrijwel perfecte 2-D symmetrische stromingspatronen en temperatuurverdelingen en dus zijn de verschillen tussen 2-D vrij oppervlak en 3-D vrij oppervlak simulaties klein. Voor lascondities met een veel sterkere oppervlaktevervorming, dat wil zeggen voor hoge warmtetoevoer en hoge concentraties van oppervlakte-actieve elementen, zullen de verschillen tussen 2-D en 3-D simulaties wellicht echter groter zijn.

Ook wanneer zowel het vrije oppervlak als de stollingsfase in de simulaties woerden meegenomen, is het voor het verkrijgen van een goede overeenstemming met experimenteel waargenomen nog steeds nodig om de thermische geleidbaarheid en de viscositeit van het vloeibaar staal kunstmatig te verhogen. De benodigde verhogingsfactor is nu echter veel lager dan de waarden die in de literatuur gebruikt worden. Dat met deze wee verbeteringen in de modelbeschrijving nog steeds onvoldoende rekening wordt gehouden met het verhoogde transport van impuls en warmte door stromingsinstabiliteiten kan te wijten zijn aan het feit dat de relatie in dit proefschrift steeds is uitgegaan van een uniforme concentratie van de oppervlakte-actieve elementen in het lasbad. Een niet-uniforme verdeling van oppervlakte-actieve elementen kan leiden tot veel meer uitgesproken stromingsinstabiliteiten en dientengevolge een dieper lasbad. Het is daarom nodig dat het transport van oppervlakte-actieve elementen in toekomstige uitbreidingen van het model wordt meegenomen, zodat de verdeling van de concentratie over het oppervlak kan worden voorspeld.

Wanneer we kijken naar de interactie tussen de lascondities, de opgewekte Ma-

rangonistroming en de uiteindelijke vorm van het lasbad, kunnen we concluderen dat de lascondities (sterkte van de warmtebron en concentratie van oppervlakteactieve elementen in het lasbad) een sterke invloed hebben op de grootte en richting van de Marangonistroming. Indien de snelheid van de Marangonistroming voldoende hoog is, heeft de richting van deze stroming een grote invloed op de uiteindelijke vorm van de las na stolling. In het algemeen leidt een naar buiten gerichte oppervlaktestroming in een ondiepe, maar brede las, terwijl een naar binnen gerichte stroming resulteert in een smalle, maar diepe las.

De grootte en richting van de Marangonistroming worden bepaald door de grootte van de laterale temperatuurgradiënten, en door de omvang en het teken van de temperatuurgradiënt van de oppervlaktespanning. Met toenemende geabsorbeerde energie neemt de laterale temperatuurgradiënt over het oppervlak toe, wat leidt tot een verhoogd Marangonigetal en hogere stromingssnelheden in het lasbad. Op soortgelijke wijze leidt het verhogen van de concentraties van oppervlakteactieve elementen resulteert in een hogere absolute waarde van de temperatuur gradiënt van de oppervlaktespanning, wat eveneens leidt tot een verhoogd Marangonigetal en hogere snelheden in het lasbad. Bij een geringe warmtetoevoer en lage concentraties van de oppervlakteactieve elementen neemt de oppervlaktespanning af met toenemende temperatuur van het lasbladoppervlak en is de oppervlaktespanning lager in het centrum van het lasbad dan aan de rand. Hierdoor is de Marangonistroming gericht vanuit het midden naar de rand. Verhoging van de concentratie oppervlakteactieve elementen, of verhoging van de lasbadtemperatuur door gebruik van een sterkere warmtebron, kan leiden tot een toestand waarin de oppervlaktespanning stijgt met de oppervlaktetemperatuur in hete delen van het lasbad, en afneemt met de temperatuur in de koudere zones. In dat geval het heeft de oppervlaktespanning een maximum ergens tussen het centrum en de rand van het lasbad, en zijn er twee in tegengestelde richting draaiende Marangonistromingen: in het midden een naar buiten gerichte stroming en aan de rand een naar binnen gerichte stroming. Als de concentratie van de oppervlakteactieve elementen zo hoog is dat de oppervlaktespanning overal in het lasbad toeneemt met toenemende temperatuur, dan heeft de oppervlaktespanning een minimum aan de rand van het lasbad rand en treedt er een volledig naar binnen gerichte stroming op. Tijdens de stollingsfase, na uitschakeling van de warmtebron, neemt de geabsorbeerde energie abrupt af, waardoor zowel de oppervlaktetemperatuur als de laterale temperatuurgradiënten aan het oppervlak afnemen. Bij lage concentraties oppervlakteactieve element veroorzaakt dit een omkering van de richting van de Marangonistroming. Bij hoge concentraties oppervlakteactieve elementen blijft de Marangonistroming in dezelfde richting na uitschakeling van de warmtebron, maar de snelheden nemen toe. Dientengevolge wordt, met name voor hoge concentraties oppervlakteactieve stoffen, het lasbad dieper na uitschakeling van de warmtebron.

Vervormingen en instabiliteiten van het vrije oppervlak blijken een belangrijke rol te spelen in de hydrodynamica van lasbaden. Wanneer deze in de modellering worden meegenomen, zijn de maximale stromingssnelheden in het lasbad lager dan wanneer een plat oppervlak wordt aangenomen. Dit wijst op een toegenomen viskeus impulstransport en lagere temperatuurgradiënten ten gevolge van een

toegenomen warmtetransport. Dit heeft echter verschillende gevolgen voor verschillende lascondities. Voor een lage concentratie oppervlakteactieve elementen is de oppervlaktestroming naar buiten gericht. Een verbeterde convectieve warmteoverdracht door stromingsinstabiliteiten leidt dan tot een afname van de maximale temperatuur in het centrum omdat meer warmte wordt getransporteerd van het centrum naar de rand. Bij een hoge concentratie oppervlakteactieve elementen is de oppervlaktestroming naar het centrum gericht en leidt een door instabiliteiten verhoogde convectieve warmteoverdracht tot een toename van de maximumtemperatuur in het centrum. Het verschil russen simulaties met en zonder een vrij oppervlak neemt toe met toenemend laservermogen en met toenemende concentraties oppervlakteactieve elementen, omdat beide leiden tot verhoogde Marangonisnelheden en daardoor sterkere oppervlaktevervormingen. Hierdoor neemt ook het verschil in de voorspelde vorm van het lasbad toe.

Op basis van de bevindingen in dit proefschrift wordt geconcludeerd dat vervormingen en instabiliteiten van het vrije oppervlak een sterke invloed hebben op de stroming en warmteoverdracht in lasbaden tijdens laser puntlassen in geleidingsmode, en dat hier daarom rekening mee moet worden gehouden in lasbadsimulaties. Met verhoging van de concentratie oppervlakteactieve elementen en van het laservermogen wordt de stroming in het lasbad zeer instabiel. Deze kan dan niet meer nauwkeurig worden gesimuleerd met een model dat uitgaat van een onvervormbaar vrij oppervlak. Nauwkeuriger voorspellingen van de fysica van lasbaden kunnen worden gedaan indien rekening wordt gehouden met het vrije oppervlak, de stollingsfase en de driedimensionaliteit van de stroming. Dit vermindert de noodzaak van het gebruik van onfysische fitparameters, maar maakt deze nog niet geheel overbodig. Een verdere noodzakelijke verbetering van de modellen is het rekening houden met de niet-uniforme verdeling van de oppervlakteactieve elementen door het toevoegen van een convectie-diffusie-reactievergelijking van deze stoffen. Dit zal waarschijnlijk leiden tot een verdere verbetering van de voorspelling van de Marangonistromingen en hun instabiliteiten.

Acknowledgments

Had I worked single-handedly on the research reported in this thesis, it would have never been completed. In this part, I would like to acknowledge the help and support of the following people during the last six years.

Firstly, I thank my promotor Chris Kleijn and my daily supervisor Sasa Kenjereš. Since day one of my term as a PhD researcher in Delft, I have been enjoying working with them. We have had numerous discussions in which I learned a lot about not only all specific ingredients of my research, but also how to do research works in general. I also acknowledge their encouragement, critical reviews, and suggestions that led to a series of refinement of my work. Moreover, their passionate approach to doing science truly inspires me and is worth emulating.

Ian Richardson led the experimental group in this project. I am thankful for his comments and suggestions in our meetings, which always helped bridge the numerical and experimental extremes.

I appreciate the help of Chuangxin Zhao, who worked on the experimental part of the project. I am glad to have collaborated closely with him. He helped me a lot in terms of seeing weld pools from the 'real thing' perspective. I enjoyed very much our discussions on research and also talks about life outside research.

Anton Kidess and Hoang Anh Duong helped me with the numerical aspects of the project as we used the same CFD code. I thank them a lot for their critical eyes and the discussions we had.

Tata Steel was the industrial partner in this project. I appreciate the comments and suggestions from René Duursma, Tim Peeters, Eelco van Vliet, Nick den Uijl and Tony van der Veldt. I also thank Bart van Haastrecht as program manager at M2i for his helpful comments.

The technical supports from Erwin de Beus and Peter Bloom are deeply appreciated. As computing cluster system administrators, they provided endless help whenever I encountered problems. The secretaries at MSP Department, Amanda van der Vlist and Angela de Ceuninck van Capelle, and at Transport Phenomena Group - Chemical Engineering Department, Anita van Haren; and officers at M2i: Monica Reulink, Oscar Ruijgrok, and Gitty Bouman, made sure that all my administrative matters went smoothly and should be fully credited.

My office colleagues contributed very much to making the working atmosphere fun and enjoyable. I am fully indebted to Annekatrien Daalmans, Ozgur Gunyol,

Adrian Toader, Federico la Torre, Anton Gryzlov, Volkert van Steijn, Mengmeng Xie, Laurens van Campen, Davide Ambesi, Mohammad Kamali, Reza Malekzadeh, Farzad Mousazadeh, Galileu Olivera, Michiel Musterd, Milos Birvalski, Bernhard Righolt, Xiaogang Yang, Rajat Bhardwaj.

I am proud to be part of the Indonesian community in the Netherlands and former Indo-Delftenaars in Jakarta. I enjoyed the life-enriching friendships through offline-online interactions with them. I express my sincere gratitude to Witono Susanto, Rizli Anshari, Ismail Habib Muhammad - Linda Agustina, Irfan Pawennei, Louis Basri, Saputra - Indra Puspitasari, Elisa Anggraeni, Anggara Rhabenta, Raymon Frediansyah - Intan Ambari and family, Bib Silalahi - Rini Firdaus and family, Kamarza Mulia - Elsa Krisanti and family, Alex Sulaksana - Ria Rizqi and family, Eko Nugroho - Diany Ismirilda and family, Aditia Djaya - Dewi Kusumaningrum and family, Bambang Yudodibroto - Endang and family, Archi Delphinanto - Siska Fitrianie, Mimi Herwani, Menas Wibowo, M. Albaqir Alhadar, Agung Purniawan, Yusuf Maury, Robianesar Bakaruddin, Melisa Asrianti, Anissa Suharsono, Risvelina, Andy Sibuea, Puspa Sandhyaduhita, Reza Pramana - Rosalyn Siburian.

I thank Axel Hagen, Liesl Bosman, and their little Sophie for our friendship and especially for being such a great 2nd family to me and my wife.

I am faithfully thankful for the love and continuous encouragement from my beloved parents, parents-in-law, brothers, and sisters. Last but not least, I thank my wife Selly for patiently and understandingly bearing with me in coping with the challenging moments in my research, and our son Rafardhan for making the writing part of this thesis pleasantly refreshing.

Zaki S. Saldi

About the author

Zaki Saptari Saldi was born on September 6, 1980 in Jakarta, Indonesia. After finishing his secondary education at SMAN 81 Jakarta, he entered Bandung Institute of Technology (ITB), majoring in Aerospace Engineering. He completed his work on modeling and experiments on laboratory wing section aeroelasticity in 2002, leading to his Bachelor degree. In 2003, he was awarded the scholarship from the Japanese Ministry of Education to embark on a Master study at Department of Mechanical Engineering, Toyohashi University of Technology, Japan. He obtained Master of Engineering degree in 2005, following completion of his thesis on reactive turbulent flow simulations of non-premixed flames. In 2006, he was employed by the Netherlands Institute for Metal Research (NIMR), which later became Materials Innovation Institute (M2i), as a PhD researcher, working on CFD simulations of weld pool hydrodynamics at Department of Multi Scale Physics, Delft University of Technology, The Netherlands.